EFFECTS OF MICROSTRUCTURE AND STRAIN RATE ON DEFORMATION BEHAVIOR IN ADVANCED HIGH STRENGTH STEELS

A thesis

Presented to

The Academic Faculty

By

Kishlay Mishra

In Partial Fulfillment
of the Requirements for the Degree
Master of Science in Materials Science and Engineering

Georgia Institute of technology

December 2017

EFFECTS OF MICROSTRUCTURE AND STRAIN RATE ON DEFORMATION BEHAVIOR IN ADVANCED HIGH STRENGTH STEELS

Approved by:

Dr. Arun Gokhale, Advisor
School of Materials Science and Engineering
Georgia Institute of Technology

Dr. Shrikant P. Bhat
Principal Research Engineer
Automotive Product Applications
ArcelorMittal Global R&D, East Chicago

Dr. Naresh M. Thadhani
Chair
School of Materials Science and Engineering
Georgia Institute of Technology

Date Approved: 07/21/2017

To my parents Mrs. Karuna Mishra and Mr. Sunil Kumar Mishra…

ACKNOWLEDGEMENTS

I would like to express my sincere gratitude to my thesis advisor, Dr. Arun Gokhale, for accepting me into his lab, and guiding me through this project. His insights, discussions and encouragement, helped me complete this work. Without his consistent guidance, this work would not have been possible.

I would like to thank my thesis committee members, Dr. Shrikant Bhat and Dr. Naresh Thadhani, for their valuable time and being a part of this committee. I would like to specially thank Dr. Bhat for the numerous discussions we had during the course of this research. I would like to thank my colleagues at Georgia Tech, Sukanya M Sharma and Meha Kumar for their help in conducting mechanical tests and quantitative analysis. I would like to thank Mr. Gautum Patel for his help with the SEM. I would like to thank my friends, Vinuta Mayakonda, Divya Sawhney, Bhavishya Mittal, Ashish Kumar, Anmol Gupta and Kaushik Santhanam for their encouragement and support. I truly enjoyed my time as a graduate student with them.

I would like to thank ArcelorMittal Global R&D, East Chicago, for providing the steel sheets for this research and financial support. I would like to thank Association for Iron and Steel Technologies for the financial support during the latter half of this research.

I would especially like to thank my sister Ms. Preety Mishra, and brother-in-law Mr. Manish Jha, for their unconditional love and support. Finally, words are not enough to express my gratitude towards my parents, for all I have achieved in my life to this day, would not have been possible without their love and support.

TABLE OF CONTENTS

LIST OF TABLES

LIST OF FIGURES

SUMMARY

With an increasing demand for better fuel efficiency and better crashworthiness, automotive and steel industries in the recent past have seen enormous interest in developing thinner and stronger Advanced High Strength Sheet (AHSS) steels. During forming processes, AHSS steels can undergo deformation at 10-100/sec strain rate, while in a crash they can experience deformation at around 1000/sec. Therefore, it is important to understand their deformation at slow as well as high strain rates while designing automotive body parts. Most studies in this area have been in understanding the mechanical response of AHSS under different loading conditions. Some studies have also been done to qualitatively study the fracture surfaces, to understand the mechanisms of failure in these steels. However, very few quantitative studies have been done to understand these mechanisms of failure. Therefore, the objective of this study was to quantitatively understand the effects of microstructure and strain rate on the deformation behavior of three different grades of AHSS steels; HSLA 590, Ductibor® 500 and Usibor® 1500. Differences in microstructures were achieved using different grades of steel, as well as by changing the austenitization conditions of hot-stamping process. Microstructures were quantified for surface area per unit volume of different interfaces, volume fraction of different microstructural constituents, and length per unit volume of grain edges (for HSLA 590). HSLA 590 specimens were tested at various strain rates ranging from 10^{-4}/sec to 3200/sec and their mechanical response were studied. Similarly, mechanical response of Ductibor 500 and Usibor 1500 were studied for strain rates ranging from 10^{-4}/sec to 1000/sec. Various micro-mechanisms of failure were quantified using quantitative fractography and digital image analysis. Mechanical testing data shows that tensile

properties of HSLA 590 are most strain rate sensitive. Tensile properties of Usibor 1500 are least sensitive to changing strain rates. Tensile properties of Ductibor 500 are more sensitive to hot-forming process parameters compared to Usibor 1500. Also, some fracture micro-mechanisms have been seen to vary significantly with processing conditions, even though their effects on mechanical behavior is minimal.

CHAPTER 1

PROBLEM FORMULATION AND OBJECTIVES

1.1 Problem Formulation

Advanced high strength sheet (AHSS) steels have been extensively used in manufacturing of structural automotive body parts. They were developed to address two main issues, better crashworthiness and lower body weight to improve fuel efficiency. In these contexts, efforts have been made to develop thinner gage sheet steels that have high strength and high ductility.

HSLA steels were amongst the first types of Advanced High Strength Sheet (AHSS) Steels with relatively high ductility. Hot-stamped steels are amongst the newer generations of AHSS, increasingly finding new applications in manufacturing of structural automotive parts, due to their exceptionally high strength (~ 1500MPa) and reasonably good ductility (~ 5%). During conventional forming processes, these auto body sheet steels undergo deformation at a strain rate of 10-100/sec, while in a crash condition, they can experience strain rates on the order of 10^2 - 10^3/sec. Therefore, it is of interest to understand the deformation behavior of these steels over a range of strain rates. Various studies have been conducted on HSLA 590 to understand its mechanical response and deformation behavior at high strain rates. Some studies have also been conducted on hot-stamped steels to understand the effects of hot forming process parameters such as heating and cooling rates, and temperatures and times of austenitization during hot-stamping, on the effects of microstructure on strain rate dependence of mechanical behavior. Albeit, these studies have

mainly been focused on qualitatively understanding the deformation behavior. Also, in majority of these studies, specimen geometry is often not kept constant for quasi-static and high strain rate tests. It is well known that mechanical properties like ductility depend on test geometry. Consequently, it is of interest to quantitatively study the effects of microstructure on deformation and fracture behavior in AHSS steels, while keeping the geometry consistent for all strain rates. To the best of the author's knowledge, no previous studies have been conducted to quantitatively address the fracture micro-mechanisms in HSLA 590, Ductibor 500 and Usibor 1500.

1.2 Objectives of research

The main objective of this research is to quantitatively understand the micro-mechanisms of failure in AHSS steels and how process parameters affect the microstructure and strain rate dependence of mechanical response, particularly in HSLA 590, Ductibor 500 and Usibor 1500. Following set of tasks are formulated, in order to accomplish the overall objective of this research,

- Quantitative characterization of three-dimensional (3D) microstructures using stereology and image analysis.
- Uniaxial tensile tests at strain rates ranging from 10^{-4}/sec to 3200/sec.
- Characterization of the hot-stamping process parameters on the microstructure and strain rate dependence of mechanical behavior of hot-stamped Usibor 1500 and Ductibor 500 steels.

- Quantitative characterization of micro-mechanisms of failure using fractography, fracture profilometry and digital image analysis.

Next chapter discusses the essential background and literature review needed to design experiments and subsequent data analyses. Chapter 3 reports the experimental work undertaken. Chapter 4 discusses the results obtained from the mechanical testing, microstructural analyses and fractography. Chapter 5 presents the summary and conclusions.

CHAPTER 2

BACKGROUND AND LITERATURE REVIEW

2.1 Introduction

The main objective of this research is to understand the effects of strain rate and microstructure on the mechanical behavior and failure micro-mechanisms in Hot Rolled High Strength Low Alloy Steel (HSLA 590) and two Hot-Stamped Advanced High Strength Steels, Usibor 1500 and Ductibor 500. To achieve this objective, it is important to develop an understanding of the chemistry and thermomechanical processing of these sheet steels, and the experimental techniques for quantitative microstructural characterization and quantitative fractography. This background information is required for the design of experiments and data analyses, which is presented in the subsequent chapters. Following sections discuss the chemistry, microstructure and mechanical properties of High Strength Low Alloy Steels (HSLA) and Hot-Stamped Steels. Subsequent sections provide a background on the stereological and quantitative fractographic techniques used in the experimental work, which is presented in the next chapter.

2.2 Hot rolled High Strength Low Alloy (HSLA) Steels

High Strength Low alloy (HSLA) steels are used for structural automotive parts due to their better mechanical properties and corrosion resistance compared to conventional carbon steels. HSLA steels are designed to achieve desired mechanical properties via appropriate thermo-mechanical processing [1], rather than to achieve a particular chemistry. HSLA steels are low carbon hot-rolled steels, micro-alloyed with addition of alloying elements like chromium, nickel, molybdenum, copper, nitrogen, vanadium, niobium, titanium, and zirconium in various combinations. These steels are not considered alloy steels even though small amounts of alloying elements are added to achieve desired mechanical properties. Rather, they are considered a separate category of steels [2]. Various categories of micro-alloyed HSLA steels have emerged because of development of new chemistries and thermo-mechanical processes. HSLA steels can be classified into five categories: [1, 3]

1) Micro-alloyed Ferrite-Pearlite Steels: Precipitation strengthened via addition of very small quantities of Niobium, Vanadium, and Titanium. These alloying elements also act as strong carbide and carbo-nitride formers and facilitate grain refinement.

2) As-rolled Pearlitic Steels: Includes carbon-manganese steels with enhanced strength, weldability and formability due to addition of alloying elements.

3) Low carbon acicular ferrite steels, typically having less than 0.05% carbon and excellent combination of high yield strength, formability and toughness.

4) Dual-Phase Steels: Containing martensite and ferrite, having varying martensitic content depending on the steel grade.

5) Inclusion-shape-controlled steels containing calcium, zirconium, titanium, and/or rare-earth elements.

2.2.1 Chemistry of HSLA steels

HSLA steels do not have a fixed chemistry, in the sense that, the focus of their development is on achieving desired mechanical properties rather than achieving a specific chemical composition. Various micro-alloying elements; Nb, V, Ti and Zr, are added to low carbon steels to achieve desired mechanical properties. These alloying elements improve the tensile strength of HSLA steels by forming carbides, nitrides and carbo-nitrides.

The two most widely used alloying elements are vanadium and niobium. Vanadium contributes to strengthening by forming fine precipitates (5 to 100 nm in diameter) of V(CN) in ferrite during cooling after hot rolling [2]. The vanadium rich precipitates are not as stable as niobium rich precipitates, and are in solid solution at all normal rolling temperatures and thus are very dependent on the cooling rate for their formation. Niobium precipitates, however, are stable at higher temperatures, which is beneficial for ferrite grain refinement.

Like vanadium, niobium increases yield strength by precipitation hardening; the magnitude of the increase depends on the size and amount of precipitated niobium carbides [2]. Niobium is a more effective grain reformer compared to vanadium. Finer ferrite grains and precipitation hardening makes niobium a better strengthening agent compared to vanadium.

Jun et.al [4] studied the addition of boron in HSLA steels. Addition of boron facilitates the formation of bainitc ferrite and martensite by increasing the hardenability and thereby reducing the formation of pearlite and quasi-polygon ferrite. Combined effect of niobium and boron in HSLA on the formation of precipitates and mechanical properties was studied by Tamahiro et.al [5]. It was found that, adding only boron had little effect on the properties, whereas the combined addition of niobium and boron improved the strength and toughness balance.

2.2.2 Processing of HSLA steels

To obtain high yield strength and good weldability, ferrite grain refinement and precipitation of carbo-nitrides are important in HSLA steels. Majority of HSLA steels are thermo-mechanically processed by rolling. Different types of thermo-mechanical processes are well summarized by Skobir et.al [6].

Following thermo-mechanical processing, numerous microstructural constituents are present in the steel depending on the process parameters and compositions. These microstructural constituents determine the mechanical behavior. Following section describes different microstructures observed in HSLA steels.

2.2.3 Microstructure of HSLA steels

Microstructure of HSLA steels is governed by the processing conditions. Processing in hot-strip mill can be divided into 3 stages; heating sheet steels above Ac_3 temperature for complete austenitization, rolling, and then subsequent cooling. Table 2.1 highlights the metallurgical phenomena occurring in each stage.

Table 2.1: Process steps and corresponding metallurgical phenomena during a conventional HSLA grade steel processing

Process Step	Metallurgical Process
Reheating	Ferrite to austenite transformation, grain growth, dissolution of precipitates
Rolling	Recrystallization, austenite grain growth, precipitation
Cooling	Austenite to ferrite transformation, precipitation

A variety of microstructural phases are possible in HSLA following thermo-mechanical processing including pearlite, quasi-polygonal ferrite, granular bainite, acicular ferrite, bainitic ferrite, lower bainite, and martensite. Numerous studies have been conducted to understand the effects of alloying elements on the microstructural evolution of HSLA steels. Militzer et.al [7] comprehensively studied recrystallization, precipitation and grain growth, and developed a microstructural model for hot-strip rolling of micro-alloyed low carbon steels.

Jun et.al [4], studied the formation of different phases during continuous cooling of two different grades of HSLA steels. Effects of continuous cooling on deformation behavior were also studied in this research. It was concluded that bainite-like microstructures are formed at fast and intermediate cooling rates in low carbon HSLA steels. Microstructures transformed at slow cooling rates were identified as pearlite and quasi-polygonal ferrite. Formation of pearlite occurs at a very slow cooling rate showing a lamellar structure of

cementite and ferrite. It was found that, the quasi-polygonal ferrite was similar to polygonal ferrite. However, the grain shape of quasi-polygonal ferrite formed at medium cooling rate was relatively more irregular than that of polygonal formed at low cooling rate in carbon steels. With an increase in the cooling rates, formation of bainite was reported. When HSLA steels were rapidly cooled in water, lath microstructures of bainitic-ferrite and martensite were obtained. Figure 2.1 summarizes different microstructures obtained during this study.

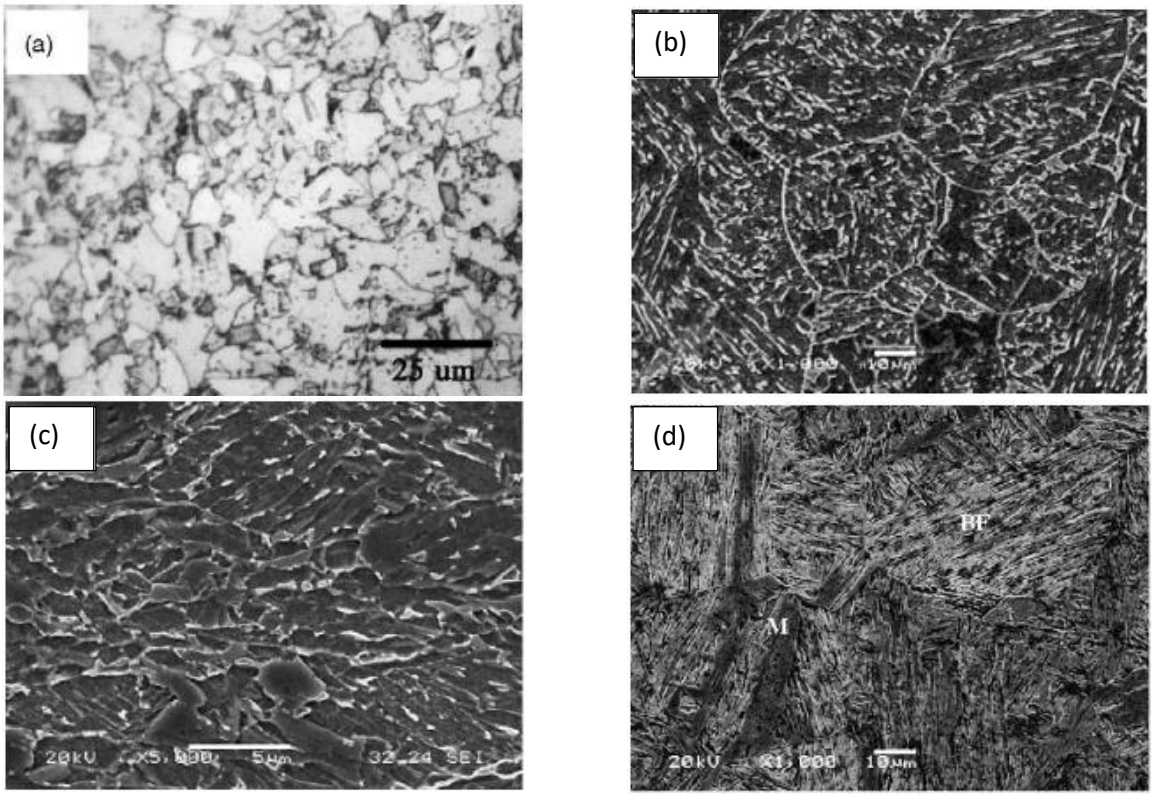

Figure 2.1: (a) Ferrite-pearlite microstructure for 0.3°C/s cooling rate in deformed CCT for steel A (b) granular bainite for 0.5°C/s cooling rate in non-deformed CCT for steel A (c) acicular ferrite for 10°C/s rate in deformed CCT for steel B (d) bainitic ferrite and martensite for 100°C/s cooling rate in non-deformed CCT for steel B.[4]

2.2.4 Failure mechanisms in HSLA steels

Various studies have been conducted to understand the tensile properties and deformation behavior in HSLA sheet steels. Bruce et.al [8] studied the effects of strain rate on tensile properties in two different grades of HSLA sheet steels. HSLA steels showed an increase in yield strength with increasing strain rate.

Zubko et.al [9] studied the deformation near the fracture surface by calculating the aspect ratio of deformed ferrite grains near the fracture edge over a spectrum of strain rates ranging from 10^{-3}/sec to 3000/sec. Ferrite grains showed a gradual decrease in aspect ratio while transition away from the fracture edge. The correlation was non-linear with distance from the fractured edge. At high strain rates, it was also observed that the ferrite grains were deformed more compared to slower strain rates. However, this difference in aspect ratio disappeared, away from the fractured edge. Deformation, therefore, was localized. Qualitative study of fractured surface revealed ductile fracture in HSLA steels in both static tests and high strain rate tests.

2.3 Press Hardened Steels

With increasing demand for improved crash-worthiness and light weight, automotive industries have begun using AHSS Steels on a large scale [10]. However, forming of ultra-high strength steel sheet has some disadvantages like unacceptably high stresses and significant spring-back phenomena, thus making traditional sheet metal forming technologies unsuitable [11]. Hot stamping combines heat treatment and press forming to produce automotive parts. In this process, steel sheets are heated in the austenite temperature range and they are then press formed and simultaneously quench hardened with dies to produce the intended shape. Since steel sheets have low strength and high ductility during heating in the austenite temperature range, they can be accurately press formed to produce complex structural parts. Moreover, steel sheets are strengthened by the martensite transformation that occurs during quenching from the austenite region. Hot stamped steels are frequently used in the production of sheet metal components such as side impact beams, bumpers, B-pillars, roof rails, and tunnels. The use of hot stamped steel parts in automotive body structure can significantly increase the passenger safety, and contribute to vehicle mass reduction and reduce fuel consumption. Following sections discuss the chemistry, processing and mechanical behavior of Press Hardened Steels.

2.3.1 Chemistry of Press Hardened Steels

Naderi et.al [12] studied different steel chemistries and found out that only boron alloys of 22MnB5, 27MnCrB5, and 37MnB4 steel grades produce fully martensitic microstructures upon hot-stamping.

22MnB5 steel and its variants are the most commonly used grades for hot-stamping. Mechanical properties of these steels are determined by the amount of carbon present and microstructure. Boron is added to improve the hardenability of the steel, thereby reducing the cooling rate required to achieve complete martensitic microstructure following hot-stamping process. Mn and Cr are also added to improve the hardenability of the steel, but their effects on mechanical properties are not as profound as due to the addition of carbon.

2.3.2 Hot-Stamping of Press Hardened Steels

Hot-Stamping is a non-isothermal sheet metal forming process in which quenching and forming takes place simultaneously in the die. Two types of hot-stamping process exists for industrial use; direct hot-stamping and indirect hot-stamping. Figure 2.2 illustrates the two processes. Generally, for automotive hot-stamping, direct hot-stamping process is employed as it provides better forming. The first step of this process is heating of the steel blank (for indirect hot-stamping, this step is after cold pre-forming). Steel is heated above Ac_3 temperature until complete austenitization. Temperature and time of heating can be varied to obtain desired mechanical properties in the hot-stamped steel. Lechler and Merkelein conducted a series of experiments to determine a processing window for complete austenitization of steel [13]. It was revealed that the temperature of austenitization and thickness of the sheet have strong dependence on time required for complete austenitization. The upper time limit of Al–Si pre-coated steel is determined by means of the thickness of the alloying ternary Al–Si–Fe layer [14] during heat treatment for good weldability [15] of the hot stamped parts during post processing. Stopp et.al [15], showed that a layer thickness of approximately 40μm should not be exceeded during austenitization in the furnace. Following austenitization, steel is quickly transferred to a

die-punch setup. A long transfer time is avoided, which may result in air-cooling of the steel, thereby, resulting in the formation of bainite or ferrite-pearlite. Sheet steel is then die-punched and quenched. Forming must complete before the beginning of martensitic transformation. Cooling rate determines the phases formed in the steel after hot-stamping [16]. To obtain a fully martensitic microstructure, generally, cooling rate must be above 27°C/sec. A number of different parameters determine the cooling rate of the steel sheet; material of die, type of coolant, coolant flow rate, temperature of coolant and number of coolant channels. Faster cooling rates can be achieved by using a coolant with a low temperature in order to increase the temperature difference between the coolant and the tool, and therefore increasing the resulting heat flux [17]. Steel sheet is quenched below M_s temperature. Typically, M_s temperature for boron sheet steel is 425°C [18]. Produced fully-martensitic sheet steels have UTS of around 1500 MPa. Hidaka et.al [19], studied the influence of heating rate, heating temperature and cooling conditions on the microstructure and mechanical properties in 2.5 wt% Mn sheet steel. Higher amount of Manganese helps in obtaining martensitic microstructure even during air cooling due to an increase in its hardenability.

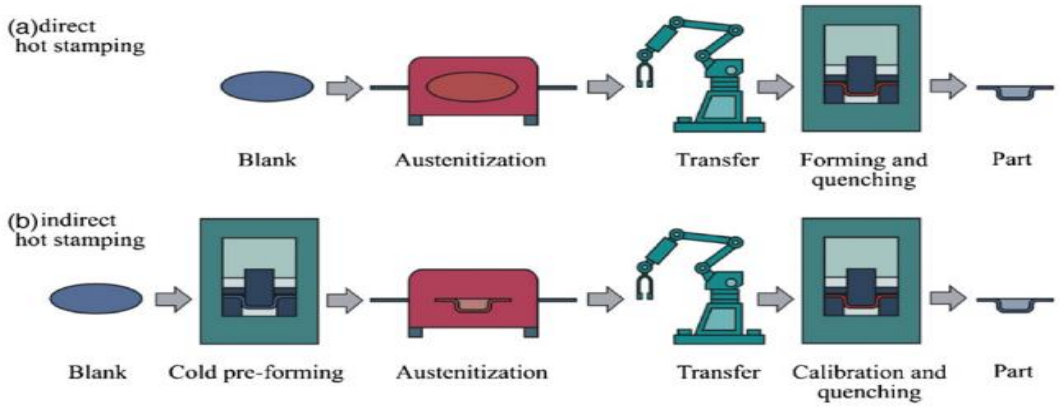

Figure 2.2: Sketch illustrates the process steps in (a) direct (b) indirect hot-stamping process [20]

Figure 2.3 shows typical microstructures obtained after different cooling rates. From this study, it was concluded that high heating temperatures lead to coarse microstructures and low strength. Also, sample heated at a faster rate displayed finer grains resulting in better mechanical properties. Following section discusses various microstructures obtained subsequent to hot-stamping process.

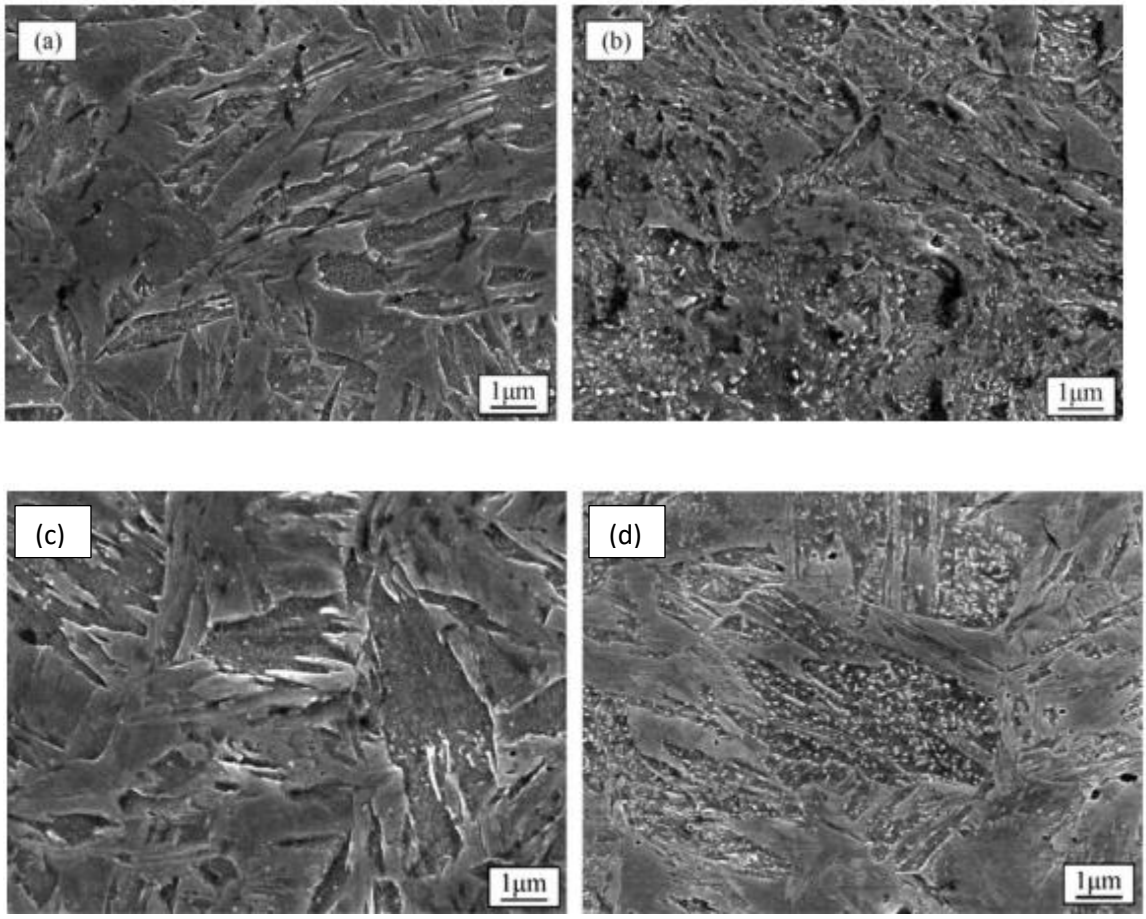

Figure 2.3: Shows different microstructures after samples were heated to 930°C at 200°C/s and (a) quenched using water spray, (b) air-cooled. Samples heated to 900°C at 200°C/s and cooled in air and subsequently quenched in water from (c) 450°C, and (d) 250°C [19]

2.3.3 Microstructure of Press Hardened Steels

Prior to the hot-stamping process, microstructure of the steel consists of ferrite and pearlite phases. Figure 2.4 shows a typical microstructure before the hot-stamping process.

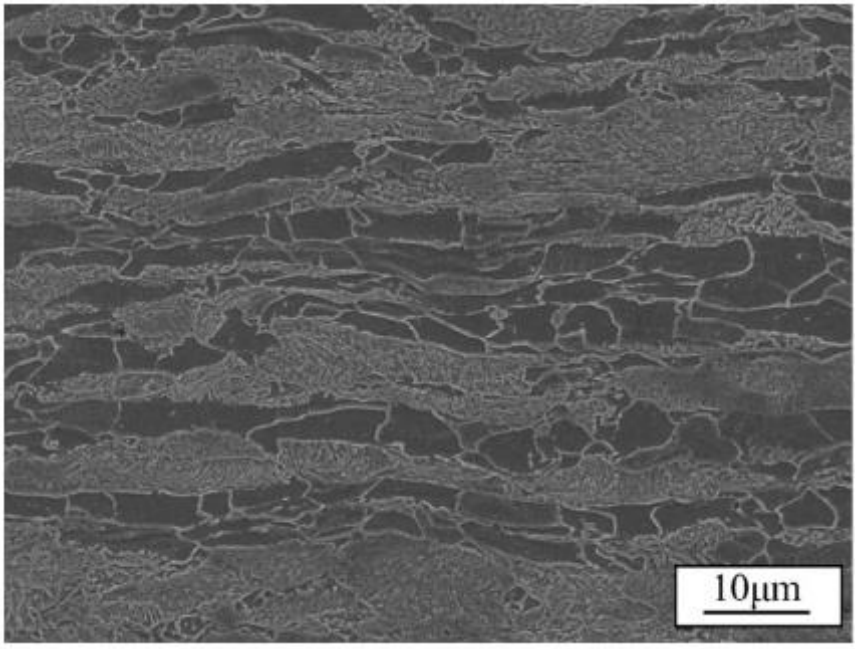

Figure 2.4: Microstructure of boron sheet steel prior to hot-forming process showing ferrite (darker phase) and pearlite (brighter constituent).[19]

After hot-stamping, a combination of pearlite, bainite, retained ferrite and martensite can form depending on the steel chemistry and processing conditions. Hot-Stamped microstructure is a strong function of the heating rate, austenitization temperature and cooling rate. Uthaisangsuk et.al [21] studied the formation of different phases at different cooling rate after hot-stamping. Samples were heated to 950°C for 5 minutes for complete austenitization, following which, samples were cooled in open furnace, air and oil. CCT diagram used in the study [22] helped in predicting the phases formed in the samples. It is depicted in figure 2.5.

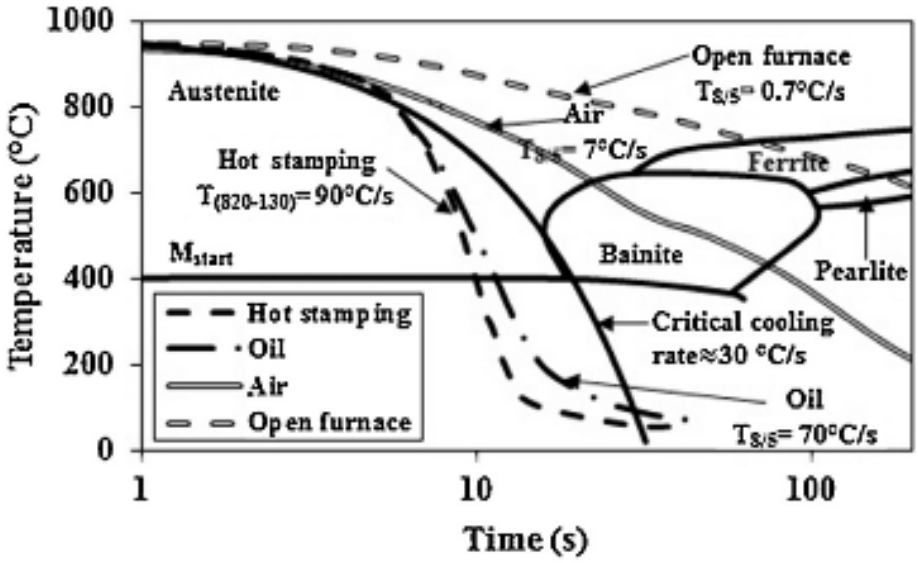

Figure 2.5: CCT diagram used in the study conducted by Uthaisangsuk et.al [22].

As expected, ferrite - pearlite microstructure is observed in samples cooled in furnace. Air cooled samples showed fully bainitic microstructure. A very high cooling rate of approximately 70°C/sec, samples generally exhibited typical lath martensite microstructure. Figure 2.6 shows the obtained microstructures after hot-stamping and subsequent cooling of the samples.

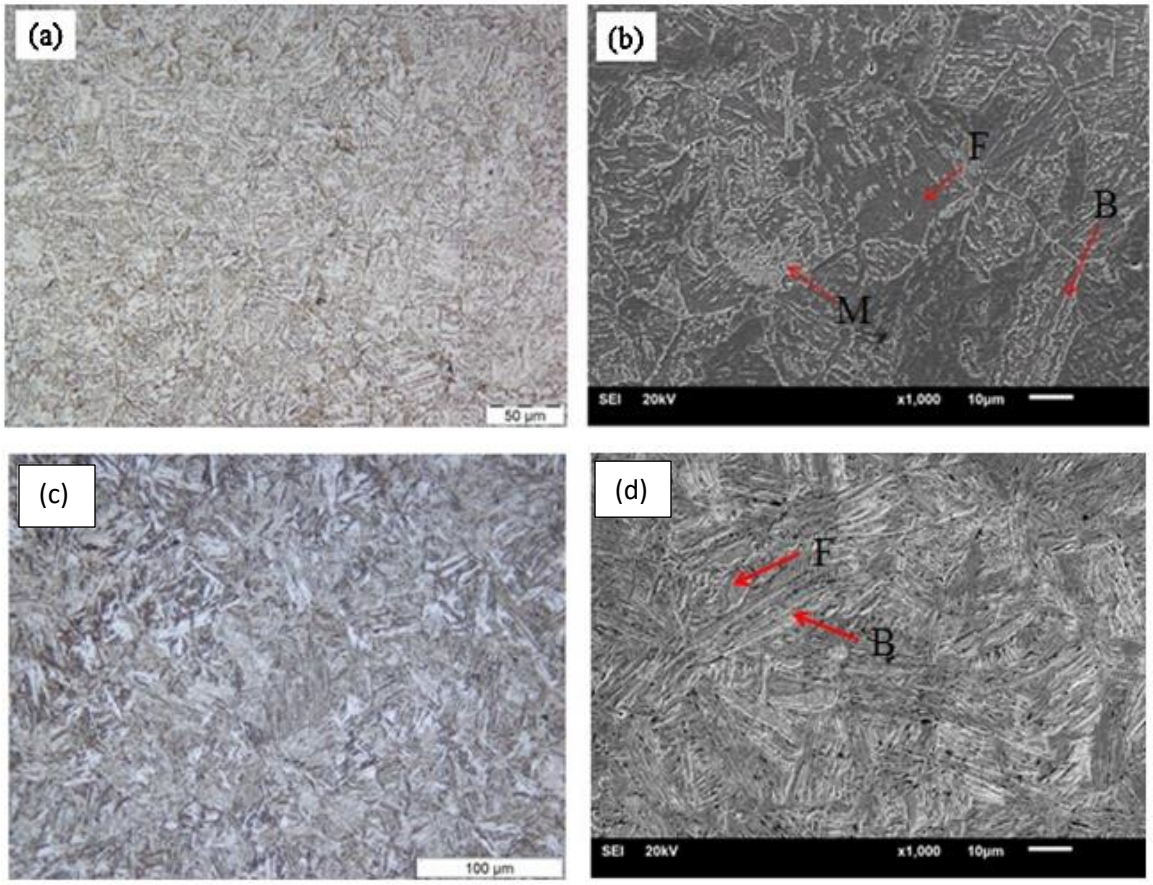

Figure 2.6: Microstructures obtained after heating and cooling in air (a) LOM (b) SEM. Microstructures obtained after heating and cooling in oil (c) LOM, and (d) SEM. [22]

In a comprehensive study, Hidaka et.al [19] observed different microstructures obtained with different austenitization and cooling conditions. Samples of 0.22%C-2.5%Mn grade steel were heated at 10°C/sec and 200°C/sec to a number of different final temperatures ranging from 650°C to 900°C in 25°C increments. The samples were then cooled either in air or water. It was observed that heating the samples to high austenitization temperature results in coarser martensite grains, and consequently, low strength. Also, samples heated at 200°C/sec show a smaller grain size for the same heating temperatures than the samples heated at 10°C/sec. The main reason being not enough time available for grain growth in samples heated at 200°C/sec than those heated at 10°C/sec. Furthermore,

subsequent to cooling, samples heated to 811°C mostly consisted of martensite whereas samples heated to 761°C consisted of martensite, transformed ferrite and recovered ferrite. Sample heated to 930°C (well above Ac_3 temperature) showed complete martensitic microstructure upon water cooling whereas it showed presence of cementite while cooled in air. This strongly suggested tempering of martensite during slow cooling in air. A further set of experiments confirmed the precipitation of cementite only in the martensitic matrix.

2.3.4 Surface Coating on Press Hardened Steels

To improve the corrosion resistance and paint adhesion after forming, as well as to prevent scale formation and decarburization during hot-forming, aluminized coating is widely used on hot-stamped steels. Aluminized coating can be formed by two different processes. In Calorizing process, Fe-Al alloy powder, sintered alumina and NH_4Cl are made to react at 850-1000°C for several hours. A Fe-Al intermetallic solution is formed at the surface [23]. Hot-dip aluminizing is the other process in which the sheet steel is dipped in liquid Al bath. During heating at 700-1100°C, the substrate steel diffuses into the coating and iron aluminized coatings are formed [23, 24]. Addition of 10 wt.% Si provides the aluminized layer with better mechanical properties, by effectively decreasing the thickness of the intermetallic layer and flatten the intermetallic substrate/interface [25, 26]. High formability of coating is essential for preventing it to fail during the hot-stamping process.

Figure 2.7 shows a typical aluminized coating on hot-stamped boron sheet steel before heat-treatment. The coating layer consists of an Al-Si matrix, with an intermetallic layer sandwiched between the matrix and the steel substrate. This intermetallic layer is important in stopping crack propagation to the substrate steel.

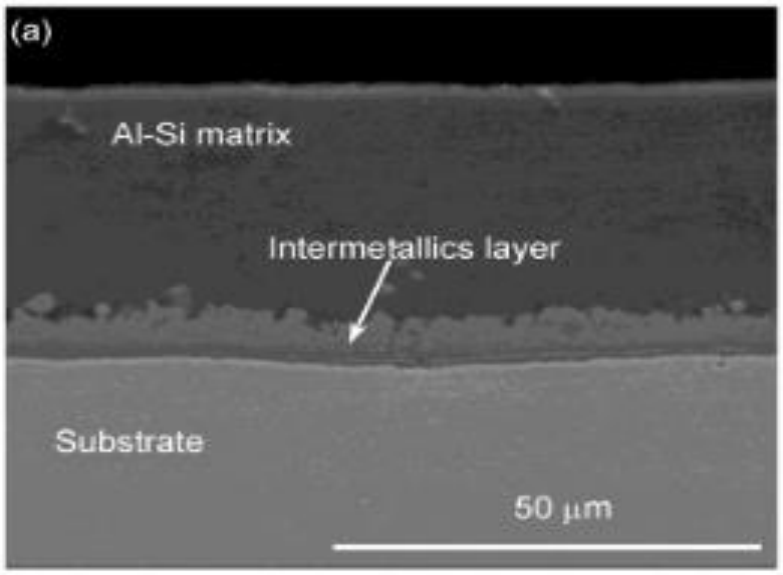

Figure 2.7: Shows a typical aluminized coating on boron sheet steel before heat treatment.[27]

Fan and Cooman [28] showed that the formed B2 Fe-Al phase was brittle in nature and the disordered α-Fe phase with Al in solid solution was ductile during high temperature deformation. It was further noted that the two main criteria for obtaining a formable coating on a hot-stamped steel are; Fe content in the coating should be above 70 at.%, and that the disordered α-Fe phase with Al in solid solution should form.

Wang et.al [29] studied different layers formed in the coating at two different austenitization temperatures and various dwell times. An increase in austenitization temperature and time allows more Fe to diffuse into the coating layer forming ductile Fe_2Al and Fe_3Al phases, which is consistent with measured number density of cracks for each time and temperature combination.

Wang et.al [30] studied in detail, the formation of crack in the coating at different temperatures of deformation with increasing strains. Three different parameters; crack

density (crack number per millimeter), average crack width and average tip distance from interface have been defined. It was found out that cracks propagate perpendicular to the substrate/coating interface. Furthermore, it was noticed that deformation temperature has little effect on crack width for small strains (<10%). Also, distance of the crack tip from the coating/surface interface was found to be larger at higher deformation temperature.

2.3.5 Failure mechanisms in Press Hardened Steels

Studies have been conducted in the past to understand deformation behavior in hot-stamped boron steels [12, 31-33]. Naderi et.al [12] have reported the effects of different phases on the observed mechanical properties of Hot-Stamped steels. Formation of cementite, bainite and retained ferrite reduces the tensile and yield strength. Press-Hardened steel used for automotive applications being predominantly martensitic, the mechanical properties are governed by the carbon content of the martensite. It is known that boron enhances hardenability [31] and might also act as grain refiner which the results in high strength and may enhance the ductility.

Bardelcik et.al [32] studied the strain rate dependence of tensile properties of boron sheet steel with five different cooling rates after hot-stamping, resulting microstructures ranging from bainitic to martensitic. A linear co-relation between Vickers hardness and fraction of martensite in the microstructure was reported. Strain rate sensitivity was found to increase with increasing strain rates. Specimen with highest cooling rate showed highest tensile strength due to completely martensitic microstructure. Area reduction measurements revealed highest ductility for lowest cooling rate (bainitic microstructure). To understand the failure mechanisms, fractured surfaces of tensile specimens have been

qualitatively studied. Figure 2.8 shows the fractured surface representing ductile and shear failure. The mode of fracture is pre-dominantly ductile when the microstructure is mainly bainatic. Ductile fracture is evident from the fibrous fracture surface due to dimpling and void growth. As the martensitic content in the microstructure increases, the failure mechanism shits from ductile to ductile-shear to predominantly shear.

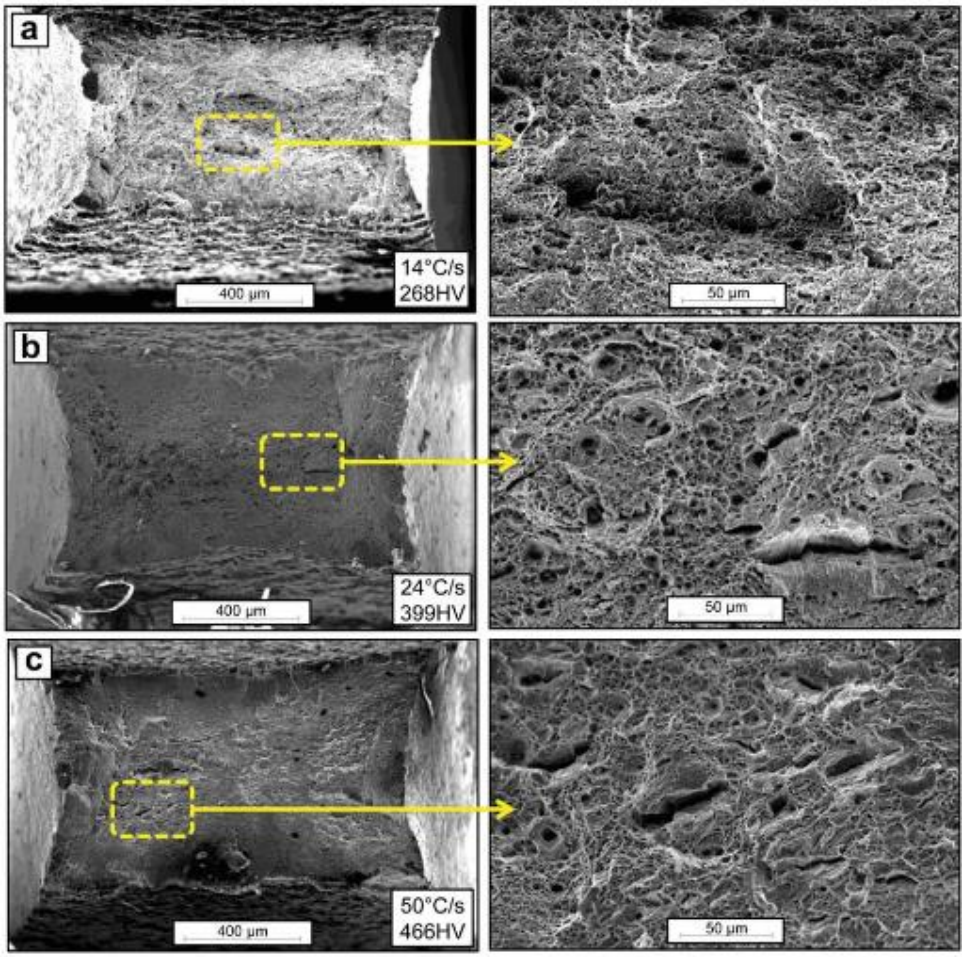

Figure 2.8: SEM fractographs showing different modes of failure for samples quenched at (a) 14°C/s (b) 24°C/s and (c) 50°C/s at quasi-static strain rate of 0.003/sec. [32]

Following section discusses the stereological techniques used in this research to quantitatively study the effects of strain rate on microstructure-property relationship and fracture mechanism in Advanced High Strength Steels.

2.4 Stereological Techniques

Quantifying microstructures forms an essential part in understanding the distribution of various attributes (grains, inclusions, defects) of microstructures in three-dimensional space. Quantifying features helps in understanding the relationship between processing, microstructure and mechanical properties. Metallographically observed microstructures are two-dimensional representation of three-dimensional structures. Three dimensional microstructures can be quantified using probes of lower dimensions; planar sections as a 2-D probe, line as a 1-D probe and point as a zero dimensional probe. Stereological measurements can be made manually or with the help of digital image processing. Using Digital Image Processing, features in the microstructure can be binarized, thereby automating the quantification processes by employing computer algorithms. Not all metallographic images can be binarized as the features are not contrasting enough. In such cases, manually quantifying the microstructure is more reliable and accurate. Stereology provides a set of relationships [34] that can statistically correlate measurements made on two-dimensional micrographs (projections of 3D microstructures) to quantify 3D attributes. Following sections discuss the stereological techniques and Digital Image Processing used in this research.

2.4.1 Estimation of Volume Fraction

Relative amounts (Volume Fraction, V_V) of different microstructural attributes in 3D can be calculated from 2D micrographs obtained by standard optical microscopy or scanning electron microscopy. Volume fraction can be estimated using areal analysis, lineal analysis or point counting.

Areal analysis in estimating volume fraction requires the measurement of area fraction of different microstructural attributes [34, 35]. It is denoted by A_A. By incorporating digital image processing, absolute areas of different attributes can be calculated. Area fraction in 2D micrograph is equal to the volume fraction in 3D microstructure.

$$<A_A> = V_V \quad (1)$$

Lineal analysis incorporates superposing straight test lines in any orientation on the 2D microstructure. By superposing set of test lines on the micrographs, absolute length of test lines in different phases can be measured. Length of test lines in desired features averaged over the total length of test lines (L_L) provides the statistically unbiased estimate of volume fraction.

$$<L_L> = V_V \quad (2)$$

An easy method for unbiased estimation of volume fraction is by point counting. Volume fraction can be estimated by randomly placing a grid of points, generally between nine and thirty-six, on 2D micrographs and calculating the fraction of points (P_P) lying in the region of phase of interest. Point fraction provides a much faster way of estimating volume fraction compared to the previous two methods.

To summarize different stereological techniques to estimate volume fraction,

$$V_V = <A_A> = <L_L> = <P_P> \quad (3)$$

2.4.2 Estimation of Surface Area per Unit Volume

2D surfaces like grain boundaries and interfaces in 3D space, when observed in 2D micrographs, appear as lines. These features play a key role in determining the mechanical

and physical properties of the material. Surface per Unit Volume is the total surface area of desired boundaries or interfaces in a unit volume of investigation. It is denoted by S_V. S_V can be estimated by placing a grid of straight test lines on the 2D micrographs. Counting the number of intersections of test lines with the boundaries or interfaces, averaged over the total length of the test lines provides the estimate of S_V. The relationship between number of intersections and S_V is given by [34, 36]

$$S_V = 2\langle P_L \rangle \tag{4}$$

Statistically unbiased estimate of S_V can be made by averaging P_L over all orientation of test lines and in all orientations of metallographic planes. For homogeneous microstructures, where the attributes are randomly oriented, only one cross-section provides a good estimate of Surface Area per Unit Volume. For non-homogeneous microstructures, a number of different orientations of test lines in various metallographic cross-sections of random orientation can provide a good estimate of S_V. For microstructures with an axis of symmetry, for example an extruded wire, a vertical axis containing all metallographic cross-sections encompasses all the orientation of test lines in 3D space [37]. For statistically unbiased estimation of S_V, intersection count by test lines have to be a sine average of the angle of orientation of test lines and the vertical axis. By using cycloids, placement of straight test lines in random orientations can be can be avoided [37, 38]. To make unbiased estimation, the minor axis of the cycloids should be perpendicular to the vertical axis. Surface Area per Unit Volume can then be defined as

$$S_V = 2\langle P_L^{cyc} \rangle \tag{5}$$

Axis of symmetry is absent in rolled products like sheet steels. In such cases, three vertical planes oriented at an angle of 120° with each other (tri-sector) are used [37]. S_V is then estimated by averaging the point count of cycloids over all three planes. Vertical axis in these cases are chosen such that most of the surface features are not parallel to the chosen direction. Minor axis of the cycloids are kept parallel to the vertical axis and S_V is estimated by

$$S_V = \langle P_L^{cyc} \rangle \tag{6}$$

2.4.3 Estimation of Number per Unit Area

Number per unit area of microstructural features can be estimated using an unbiased frame [39]. It is denoted by N_A. Two edges of the frame are "forbidden" and any feature touching these are not counted. Features inside the frame and only touching the remaining two edges are counted. Figure 2.9 Illustrates the unbiased counting frame used to estimate N_A.

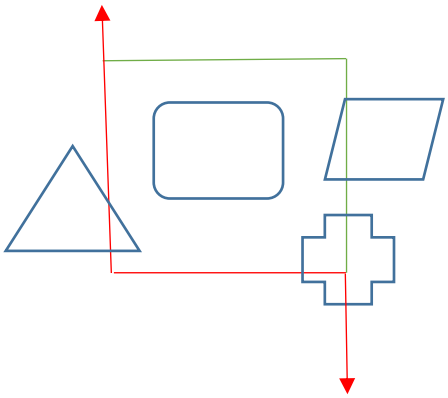

Figure 2.9: Illustrates forbidden edges in red. Features touching the red edges are not counted.

Number of features in the above unbiased counting frame is 2. Number per unit area for this example would be 2 divide by the area of the frame. Unlike volume fraction, S_V and

N_A are not dimensionless quantities. It is important to take into account the magnification of the metallographic images while estimating S_V and N_A.

2.4.4 Quantitative Fractography

Quantitative fractography plays an important role in understanding the micro-mechanisms of failure in tensile specimens. Failed tensile specimens can be observed under Scanning Electron Microscope and a series of measurements to quantify features of fractured surfaces can be made using the stereological techniques. Figure 2.10 shows fracture surface of a typical failed dog-bone specimen for sheet steel.

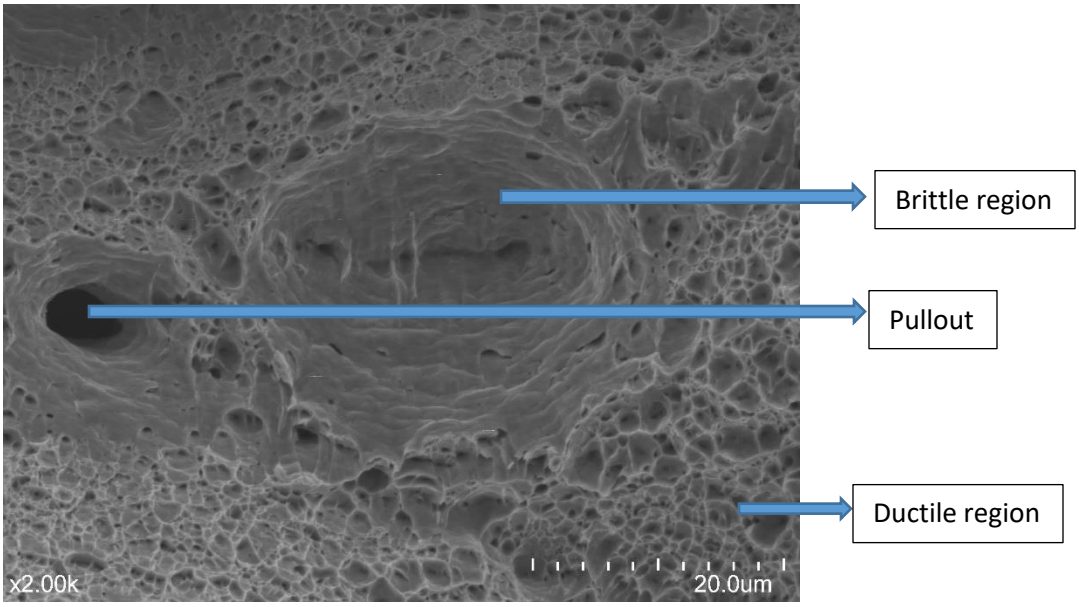

Figure 2.10: Illustrates different features in a fracture surface of HSLA 590.

A typical fracture surface contains features corresponding to ductile failure, brittle failure, pullouts, cracks and inclusions. One of the most common measurements is to

estimate the area fraction of different features in a fractured surface. Area Fraction can be estimated by point counting technique described earlier.

$$A_A \text{ (feature of interest)} = P_P \text{ (feature of interest)} \quad (7)$$

A_A estimated through this technique is the area fraction of the feature in the SEM image. Error is incorporated into the measurements as the fractured surfaces are two-dimensional projection of non-planar surfaces. True area fraction in 3D space (F) can be estimated by incorporating a factor called surface roughness parameter (R_S) [40, 41].

$$F = [R_S / (R_S)_\beta] \langle P_P \rangle = [R_S / (R_S)_\beta] A_A \quad (8)$$

Surface roughness parameter is defined as follows,

R_S = Actual Area of fracture surface (S)/Area of projection of the fracture surface (A) (9)

Figure 2.11 illustrates the fracture roughness parameter. Vertical section planes can be used to estimate the value of R_S. Figure 2.12 shows the vertical section profiles. Fracture profile generated by the vertical sections is characterized by surface profile roughness parameter R_L.

$$R_L = \text{True profile length } (L_T) / \text{Projected length } (L) \quad (10)$$

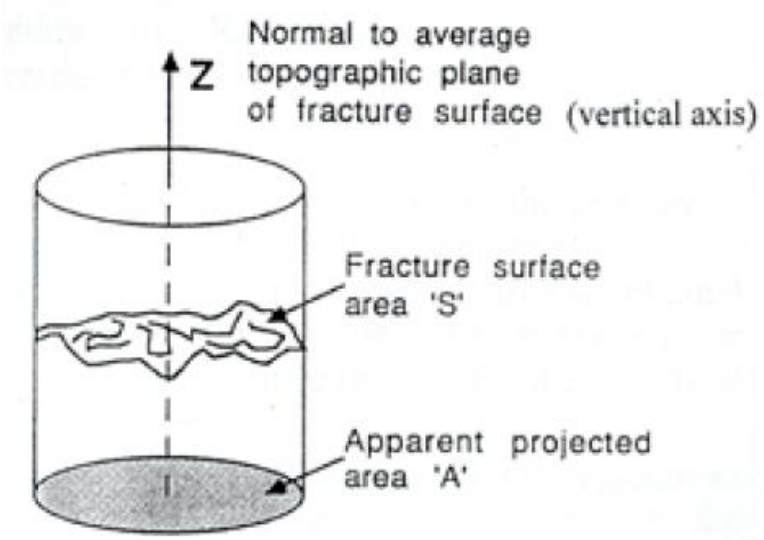

Figure 2.11. Schematic illustrating the fracture roughness parameter.[40]

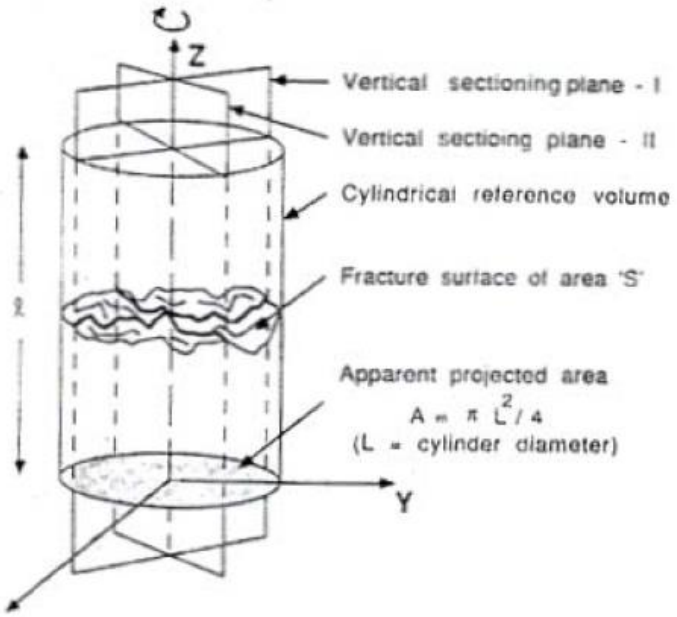

Figure 2.12. Schematic illustrating the vertical section fracture profile.[40]

Following relations correlates surface roughness parameter R_S with fracture profile roughness parameter R_L [41].

$$R_S = \langle \Psi . R_L \rangle \quad (11)$$

where, $$\Psi = \int_0^{\pi} [\sin\alpha + \{(\pi/2 - \alpha)\cos\alpha\}] f(\alpha).\, d\alpha \quad (12)$$

Ψ is called the profile structure factor and $f(\alpha)$ is defined such that $f(\alpha)d\alpha$ is the fraction of profile length in the orientation range of α to $(\alpha+d\alpha)$, where $0 < \alpha < \pi$. $f(\alpha)$ is called the orientation function of the fracture profile. Estimation of surface roughness via calculating profile roughness parameter is complicated and can be achieved by computer algorithms.

Number per unit area of features in fracture surfaces can also be estimated using the technique described in Section 2.4.3. Considering the non-planarity of the fractured surface, number per unit area estimations made on SEM fractographs is defined as

$$N_S = \langle N \rangle / (A/M^2) \quad (13)$$

where A is the area of SEM image and M is the magnification. True number per unit area (N_f) is estimated by dividing N_S by surface roughness R_S.

$$N_f = N_S / R_S \quad (14)$$

Another important parameter to quantitatively characterize the fracture surface is the average dimple size. The average dimple size is given by [42, 43].

$$\Omega = F / N_f \quad (15)$$

2.4.5 Digital Image Processing

Digital Image processing provides strong and efficient tools to make stereological measurements using computer algorithms. Many features in the microstructure may extend over a longer range than that can be captured in multiple fields of view. In such cases, it is

desirable to have one single image of the complete microstructural feature without the loss of any resolution. A method developed at Georgia Institute of Technology, allows images of large area to be taken at high resolution [44]. The first step involves grabbing a random field of view (FOV) in the area of interest in the metallographic plane. The image is stored in the memory as an image file. The right border of about 60 pixel width of this image is then displayed along with the live image. This results in superimposed image on the left border with the rest of the screen having live image. Using software packages, the images can be stitched together to form one single image. Stitching several such images creates a "montage" in the computer memory without losing resolution of a single field of view. This can be utilized in profilometric studies of the fractured specimens at high magnifications.

Software's like Image J, provides an interactive interface to make stereological measurements by superposing measuring probes on the obtained micrographs and fractographs. Table 2.2 illustrates the plugins used in Image J to make corresponding measurements described in the previous section.

Table 2.2: Shows the plugins used for various stereological measurements in Image J.

Measurement	**Stereological Technique**	**Image J Plugin**
Volume Fraction	Point Counting	Point Counting Grid plugin
Surface Area per Unit volume	Intersection counts	Cycloid Grid plugin
Number per Unit Area	Unbiased Frame	Unbiased Frame plugin

Stereological techniques described in the current chapter are utilized in this research, as discussed in the next chapter.

CHAPTER 3
EXPERIMENTAL WORK

3.1 Introduction

The main objective of this research is to understand the effects of strain rate on deformation, fracture and quantitative-microstructure properties relationship in hot-rolled HSLA and press-hardened steels. For this purpose, quantitative microstructural characterization, tensile testing, and quantitative fractography of commercially produced hot-rolled HSLA 590 and Press-Hardened Usibor 1500 and Ductibor 500 has been carried out. Processed steels were provided by ArcelorMittal Global R&D, East Chicago after thermo-mechanical processing, heat treatment and hot-stamping. Experimental work encompasses two parts; tensile testing of the sheet steels at different strain rates and quantitative study of microstructure and fracture surfaces. Tensile tests were conducted over a spectrum of strain rates ranging from 10^{-4} to 3200/sec for HSLA 590 and 10^{-4} to 1000/sec for hot-stamped Ductibor 500 and Usibor 1500. Quasi-static strain rate tests involved the servo-hydraulic setup whereas higher strain rate tests were performed on Hopkinson Bar equipment. Microstructure and fracture surfaces of the tested specimens were characterized using stereology, image analysis and SEM fractography. Following sections describe the experimental procedures used for mechanical tests, metallography, quantitative microstructural characterization, fractography and fracture profilometry in the present research. Obtained experimental data have been analyzed in the next Chapter to understand the effects of strain rate on micro-mechanisms of failure.

3.2 Materials and Processing

3.2.1 Materials Chemistry

Commercially produced hot-rolled sheet HSLA 590 (2.5mm thick), Usibor 1500 (1.5mm thick) and Ductibor 500 (1.5mm thick) were obtained from ArcelorMittal Global R&D East Chicago. Table 3.1 shows the nominal bulk chemical composition of these sheet steels.

Table 3.1: Chemical composition of the steel grades being used in this research.

Steel Grade	C	Mn	Si	Cr	Ti	Nb	Al	N	P	S	B
HSLA 590	0.05	1.54	0.13	-	0.03	0.05	0.03	0.006	0.01	0.005	-
Usibor 1500	0.23	1.245	0.27	0.02	0.04	-	0.04	0.004	0.01	0.002	30 ppm
Ductibor 500	0.064	1.604	0.03	0.02	0.07	0.055	0.03	0.006	0.02	0.002	-

Table 3.2 shows the average tensile properties of "As Received" Ductibor 500 and Usibor 1500.

Table 3.2: Quasi-static mechanical properties of "as received" DUCTIBOR 500 and USIBOR 1500.

Tensile Properties "as received", 1.5mm thick sheet				
Grade	UTS (MPa)	Yield Strength (MPa)	Uniform Elongation (%)	Total Elongation (%)
Ductibor 500	584	493	15.1	23.2
Usibor 1500	589	452	12.0	18.8

Above values are for specimens with standard ASTM E8 geometry, machined with the gage section along the transverse direction of rolled sheet.

3.2.2 Materials Processing

For hot-stamping, three different time-temperature combinations of austenitization were selected. Commercially produced Usibor 1500 and Ductibor 500 were subjected to these austenitizing conditions. Table 3.3 shows the time and temperatures used for this study.

Table 3.3: Austenitization conditions used for hot-stamping experiments.

Temperature of austenitization (°C)	Time of holding the blank inside the furnace(min)
920	7
950	15
980	30

The time-temperature combinations were selected for this study, recognizing the existing industrial practice, temperature of 920°C for 7 minutes being the optimum condition, 950°C for 15 minutes being the extreme condition and 980°C for 30 minutes being the abuse condition. The most widely used combination in the industry is austenitization at 920°C for 7 minutes.

Subsequent to the austenitizing process, these blanks were die-quenched until the temperature of the blanks reached below M_f temperature of the steel. These blanks were then air cooled to room temperature. Figure 3.1 shows the schematic of obtained blanks after hot-stamping. Different regions of the blank are marked on the figure. Top-hat, side walls and flanges were separated, and tensile specimens were machined from the top-hat using water jet machining. Figure 3.2 shows the area on the top hat from which tensile

specimens were machined. Specimen geometry and tensile testing techniques are discussed in the next section.

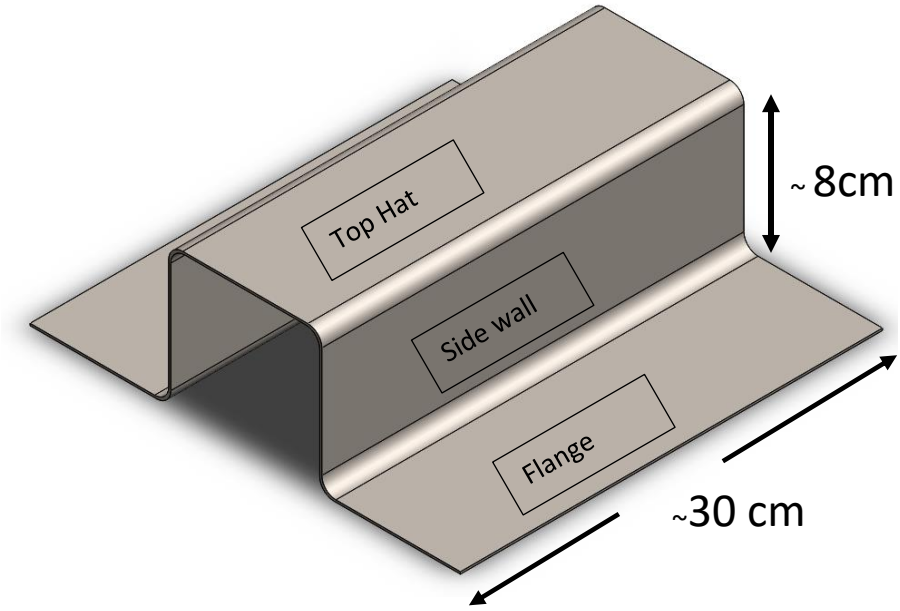

Figure 3.1: Schematic of the hot-stamped blank

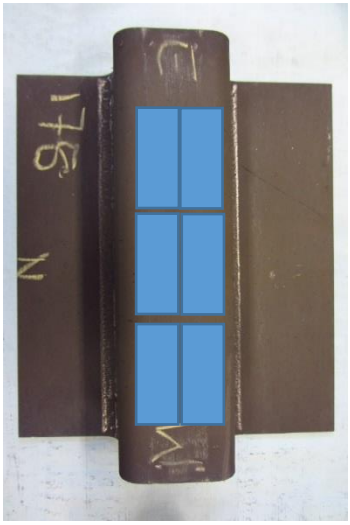

Figure 3.2: Figure showing the location of machined tensile specimens from the top hat section

3.2.3 Tensile Testing

Tensile test specimens were machined from blanks using water-jet with gage section in the transverse direction. For industrial practices, ASTM E8 or JIS specimen geometry is used for testing samples at quasi-static stain rate. However, miniature geometries are used for split-hopkinson bar experiments. Therefore, the geometry was chosen according to the split-hopkinson bar setup used. Mechanical properties like ductility is dependent on the geometry of the tensile specimen. Hence, the specimen geometry was kept consistent at all strain rates, and for a particular steel grade. Figure 3.3 (a) illustrates the specimen geometry used for HSLA 590, for which the tensile tests were carried out at strain rates ranging from 10^{-4}/sec to 3200/sec. Figure 3.3 (b) shows the specimen geometry for Press-Hardened steels, for which tensile tests were carried out from 10^{-4}/sec to 1000/sec. Tensile tests for quasi-static strain rates up from 10^{-4}/sec to 80/sec were conducted using screw driven MTS servo-hydraulic tensile machine at room temperature at MPRL, Gatech. These tests were carried out under displacement control. High strain rate tests were conducted using split-hopkinson bar setup.

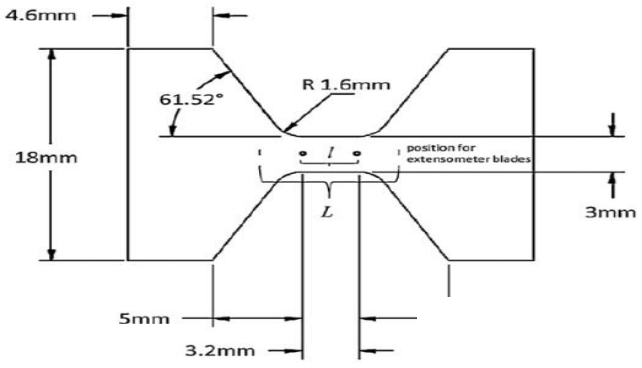

(a)

Figure 3.3: Schematic of the tensile geometry used for (a) HSLA 590 and, (b) Ductibor 500 and Usibor 1500

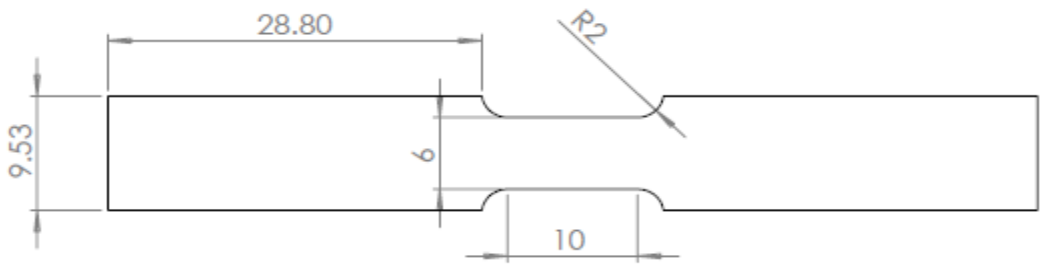

Figure 3.3: (b) continued

A strain gage was mounted on each specimen in the gage section along with DIC setup to obtain engineering stress versus engineering strain plots. Figure 3.4 illustrates the mounting of strain gauges on the specimens. A quarter wheatstone bridge circuit configuration was employed to obtain the strain values from the strain gauges.

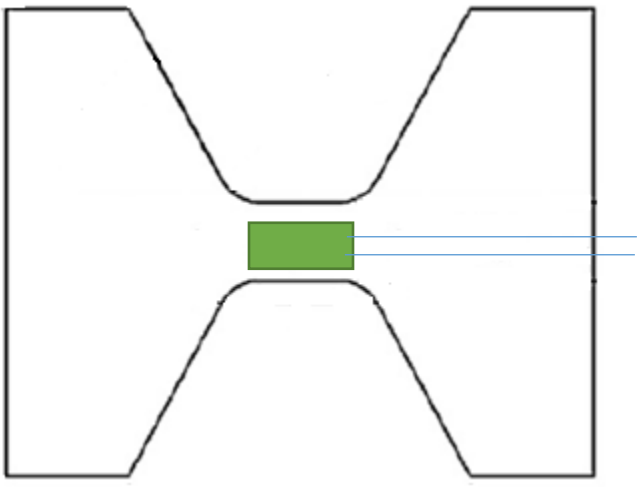

Figure 3.4: Schematic showing mounting of the strain gage on the tensile specimens for the servo-hydraulic quasi-static strain rate testing.

Specimens were marked with markers in the gauge length on the other side of strain gauge and a high speed camera was used to capture the entire tensile test process. Images

were fragmented from this video. Strain values in the specimen corresponding to each image was calculated. Obtained strain values from DIC were stitched with values obtained from strain gauge to get the complete engineering stress vs engineering strain curve.

3.3 Metallography

To quantitatively study the microstructures, metallographic specimens from three orthogonal sections were prepared for each steel grade. HLSA samples were machined from the blanks using rotatory blade cutter and hot-mounted using Bakelite. Usibor 1500 and Ductibor 500 were cold mounted in Struers DuroCit, which provided good edge retention necessary to prevent coating layer from getting damaged during polishing. Specimens were then carefully polished starting with 320 grit SiC followed by 400, 600, 800 and finally 1200 grit SiC papers. Subsequent polishing of the specimens was carried out on lapping cloth using diamond suspensions of 3 µm, 1 µm and 0.05 µm and finished with 0.02µm colloidal silica solution. Freshly prepared 2% Nital solution was used to etch the specimens for 15 secs to reveal ferrite and martensite boundaries. Etched specimens were preserved after cleaning with ethanol, under a dry environment. Micrographs of the representative microstructures are presented and discussed in the next chapter.

3.4 Digital Image Processing

For HSLA 590, microstructure of etched samples were observed under Zeiss Optical microscope at a magnification of 500X, carefully marking the three directions; rolling direction (RD), Transverse direction(TD) and thickness direction(THD) as shown in Figure 3.5.

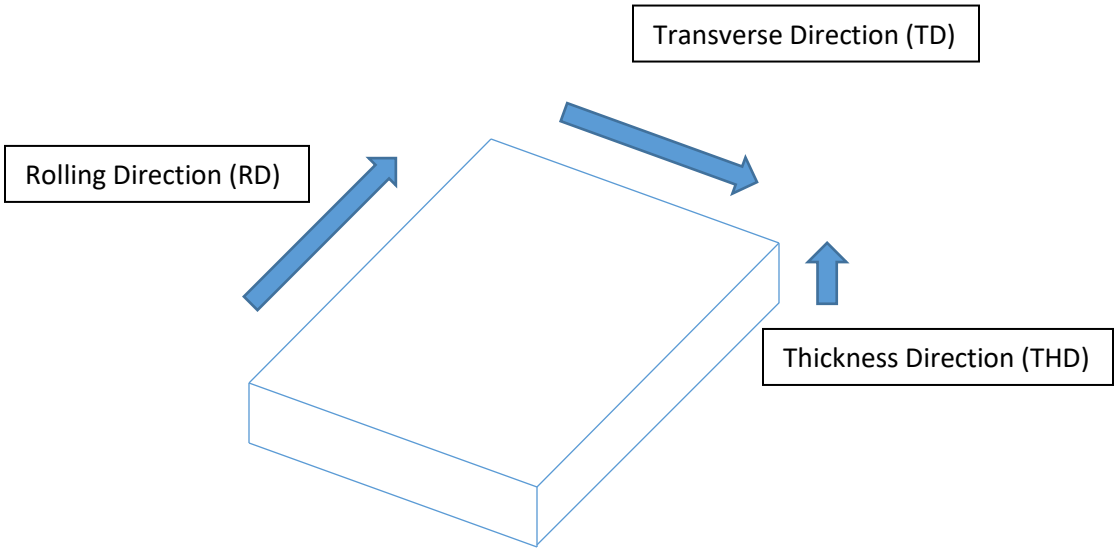

Figure 3.5: Schematic showing the three orthogonal planes of the sheet steel used for metallography

Ten systematic digital random fields of view were captured from each orthogonal section with the help of CCD camera attached to the microscope in order to make unbiased stereological measurements. In case of Ductibor 500 and Usibor 1500, due to very small grain size, resolution provided by optical micrograph was not enough to make unbiased stereological measurements. To overcome this, Hitachi SU 8010 scanning electron

microscope was used to capture 10 systematic random fields of view from TD-THD face. These images were captured at a magnification of 1000X. Numerous 3D microstructural parameters such as total surface area of grain boundaries, total length of grain edges, volume fraction of different constituents and grain size distribution were estimated on these captured images using stereological techniques. These data and their analyses are presented in the next chapter. To study the coating in hot-stamped steels, images of coating at a magnification of 1000X were captured using Hitachi SU 8010 SEM. Energy Dispersive Spectroscopy was conducted on different layers in coating to study variation in their chemical compositions.

3.5 Stereological Procedures

With the help captured micrographs, total surface area per unit volume of ferrite-ferrite interfaces (S_v) and total grain edge length per unit volume (L_V) for HSLA were calculated. Images from two orthogonal planes containing the thickness direction were used for this purpose. For Ductibor 500, volume fraction of ferrite and secondary constituents (pearlite, bainite and/or martensite) in the microstructures were estimated. Total surface area per unit volume of ferrite-secondary constituent interfaces were also estimated. In case of Usibor 1500, total surface area per unit volume of martensite-martensite interfaces were estimated.

In case of hot-stamped steels, thicknesses of various coating layers was measured at random locations using ImageJ software package. Average thickness of each layer was calculated using these values.

3.6 SEM Quantitative Fractography

Fracture surfaces were first qualitatively, and subsequently, quantitatively studied under Hitachi SU 8010 SEM. Only the central one-third region of each fracture surface were taken into account for measurements, to avoid areas of fast fracture near the edges. Fifteen systematic random fields of view (from the central one-third region) were captured to keep the calculations statistically unbiased. Obtained fractographs were analyzed for different morphologies corresponding to different micro-mechanisms of failure using ImageJ software. ImageJ provides an interactive interface to make stereological measurements on obtained optical and SEM images. Area fraction of ductile and brittle fracture regions were estimated using point counting, by placing a grid of nine points on each field of view at six different locations. Number per unit area, N_A, of dimples were calculated by placing an unbiased counting frame on the SEM images as described in Chapter 2. Number per unit area of pullouts were also determined using the same technique. After fractography of failed specimens, profilometric studies were employed as discussed in the next section.

3.7 Fracture Profilometry

Quantitative profilometric study is used in correcting the surface projection effects in quantitative data obtained from fracture surfaces as described in Chapter 2. Fractured specimens of HSLA 590 were cold mounted in Struers DuroCit to retain the fracture edge, and preventing it from getting damaged during subsequent metallographic preparation. Hot

mounting in Bakelite and cold mounting in Epoxy does not provide a good edge retention important for length measurements to understand fracture profile. DuroCit also provides a good contrast between the specimen and the mount. Specimens were polished to half the thickness to truly capture the fracture behavior, and negate the effects of fast fracture near the edges. The surfaces were metallographically prepared and finished with 0.02 micron colloidal silica suspension. Only central one-third region of the fracture profile was captured using an optical microscope, and the length of fracture profiles were measured using free-hand measuring tool in Carl Zeiss Axiovision Image Processing software. Coordinates of the fracture profile were also measured using the same tool.

Calculated microstructural parameters, results from the mechanical tests, quantitative fractography and profilometry are presented and discussed in the next chapter.

CHAPTER 4

RESULTS AND DISCUSSION

Experimental techniques and methodologies employed to understand the effects of strain rate on the deformation behavior have been discussed in the previous chapter. This chapter reports the experimental data on HSLA 590, Ductibor 500 and Usibor 1500 steels, and their analyses. Results for HSLA 590 are presented in the next section, followed by results for Ductibor 500 and Usibor 1500. Quantitative microstructural characterization, uniaxial tensile test results, and quantitative fractography data are presented together for each steel grade. Obtained data highlight the effects of microstructure and strain rate on mechanical response and fracture micro-mechanisms in these steel grades. Analyses of obtained data is carried out in the final section. Conclusions derived from data analyses are presented in the next chapter.

4.1 HSLA 590

4.1.1 Bulk Microstructure of HSLA 590

Three orthogonal planes have been characterized to quantitatively understand the microstructure. Representative microstructures in the planes containing Rolling-Transverse directions, Transverse- Thickness directions and Rolling-Thickness directions as their X-Y axes respectively, as defined in figure 3.5 are given in Figure 4.1.

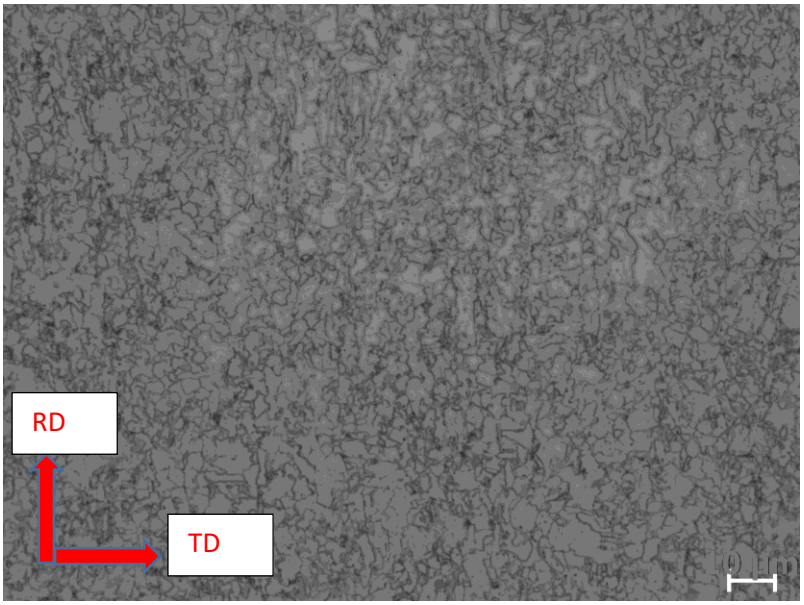

(a)

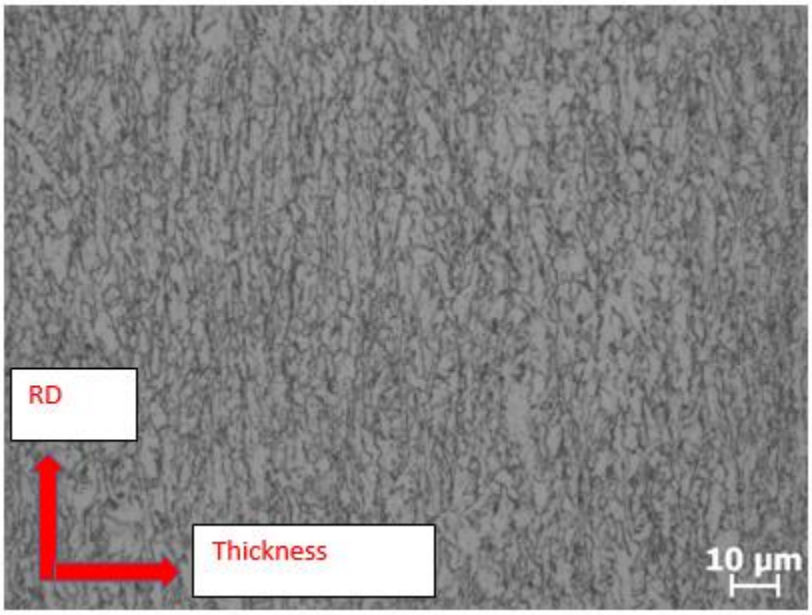

(b)

Figure 4.1: Representative optical micrographs of HSLA 590 containing (a) Rolling and Transverse directions (b) Rolling and Thickness directions and (c) Thickness and Transverse directions

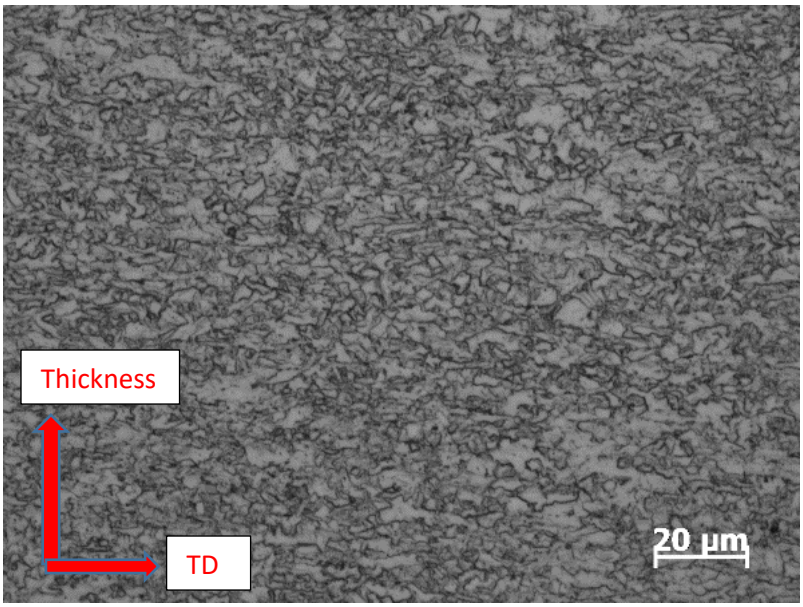

Figure 4.1: (c) continued

HSLA 590 has a ferritic microstructure, with fine carbides distributed along the grain boundaries as well as inside the grains. Qualitative analysis shows that the ferrite grains are preferentially elongated in the rolling direction. The total surface area per unit volume (S_V) of ferrite-ferrite interface was estimated to be 609 $\pm$ 72 mm^2/mm^3. Total length per unit volume of ferrite-ferrite-ferrite grain edges was estimated to be (98 $\pm$ 9) x 10^3 mm/mm^3. These obtained values were averaged over the two planes containing the thickness direction, which was the chosen vertical axis.

4.1.2 Uniaxial Tensile Test Results

Figure 4.2 shows the obtained engineering stress-strain curves for HSLA 590. UTS was calculated using the peak load. In Hopkinson bar tests and servo-hydraulic test at 80/sec, the peak on the engineering stress versus engineering strain curves may not correspond to

the UTS. This ambiguity can be resolved by taking timed images of the Hopkinson bar tests, which is being carried out currently. In case the peak does not correspond to the uniform strain (when necking begins), UTS can be calculated using the load when the necking begins. Ductility was measured by joining the fractured samples and measuring the elongation in the gage length. Figure 4.3 shows the UTS, 0.2% offset YS and ductility as a function of strain rate for HSLA 590. Each data point on figure 4.3 represents one tensile test result.

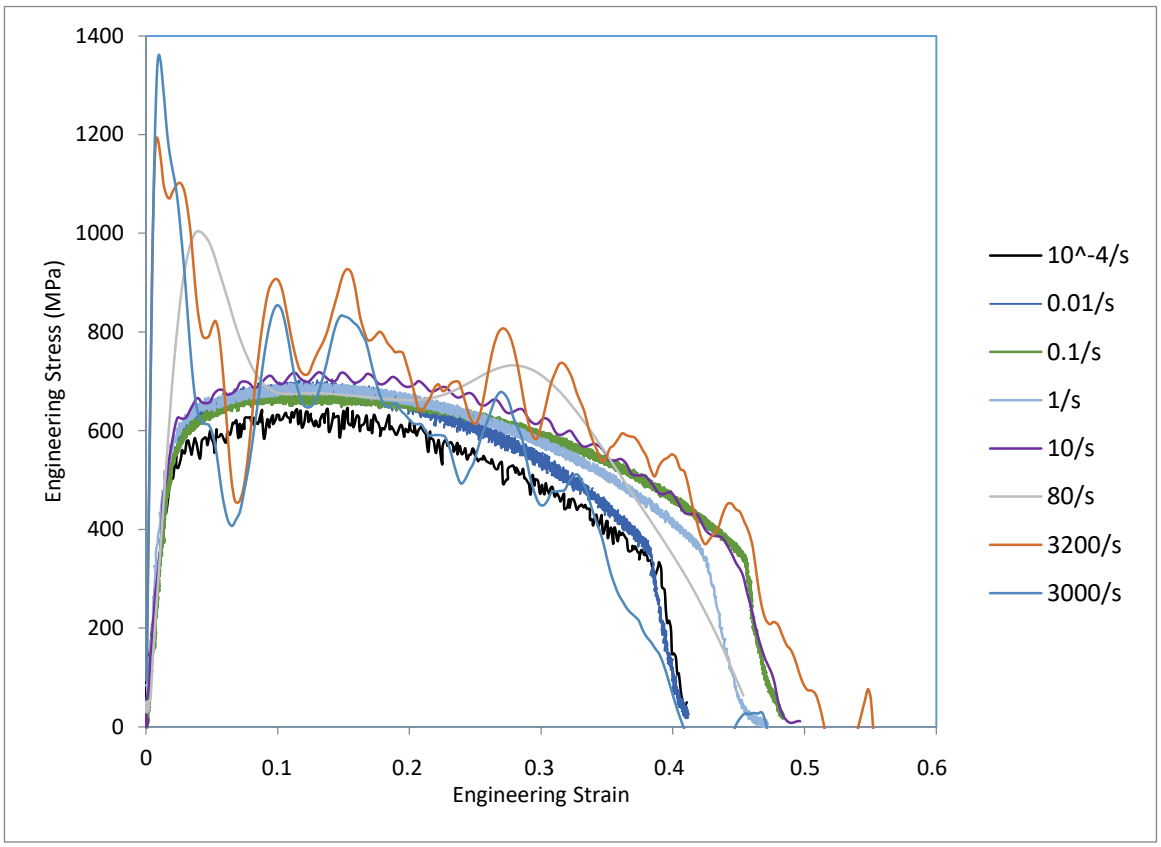

Figure 4.2: Engineering stress versus engineering strain plots for HSLA 590

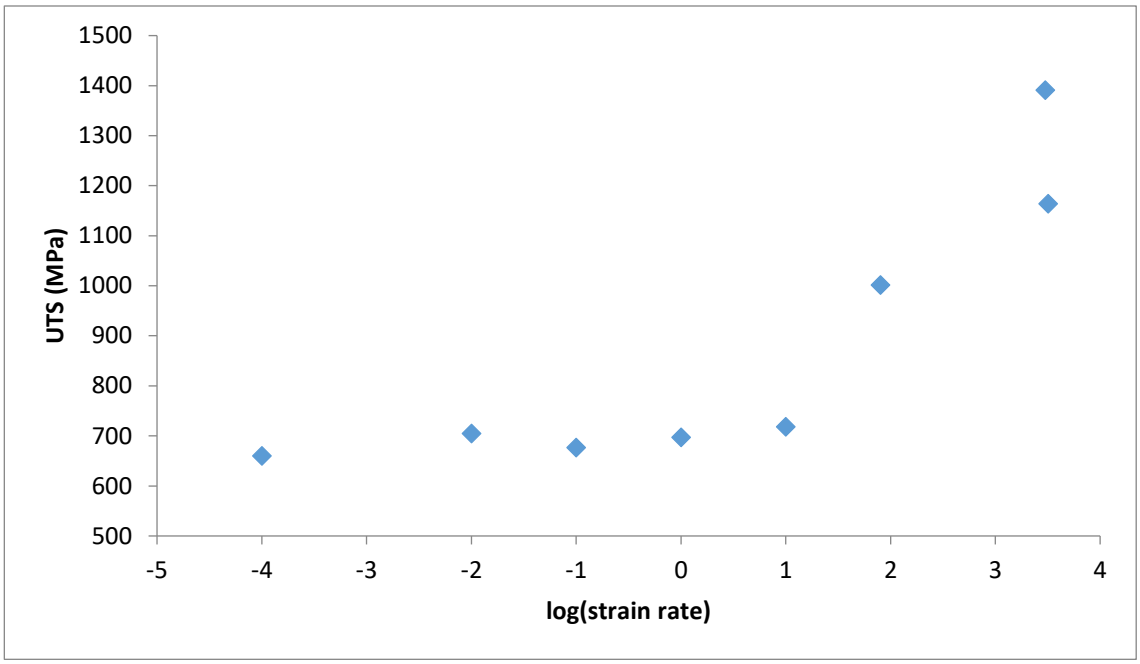

(a)

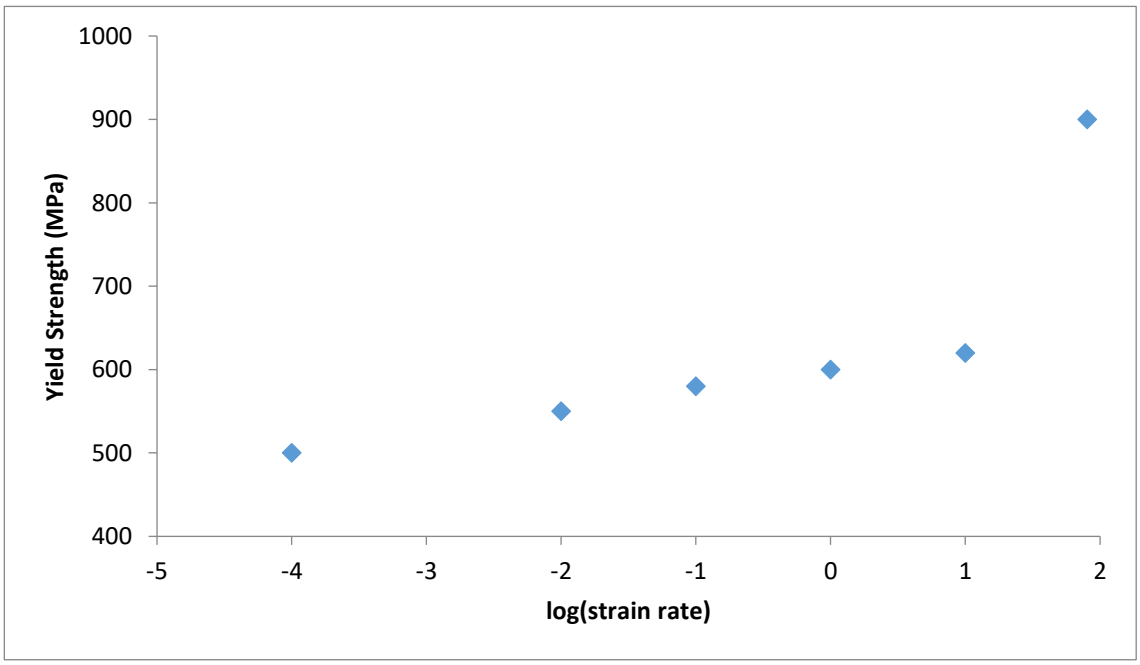

(b)

Figure 4.3: HSLA mechanical data vs log(strain rate) for (a) UTS (b) YS and (c) Ductility

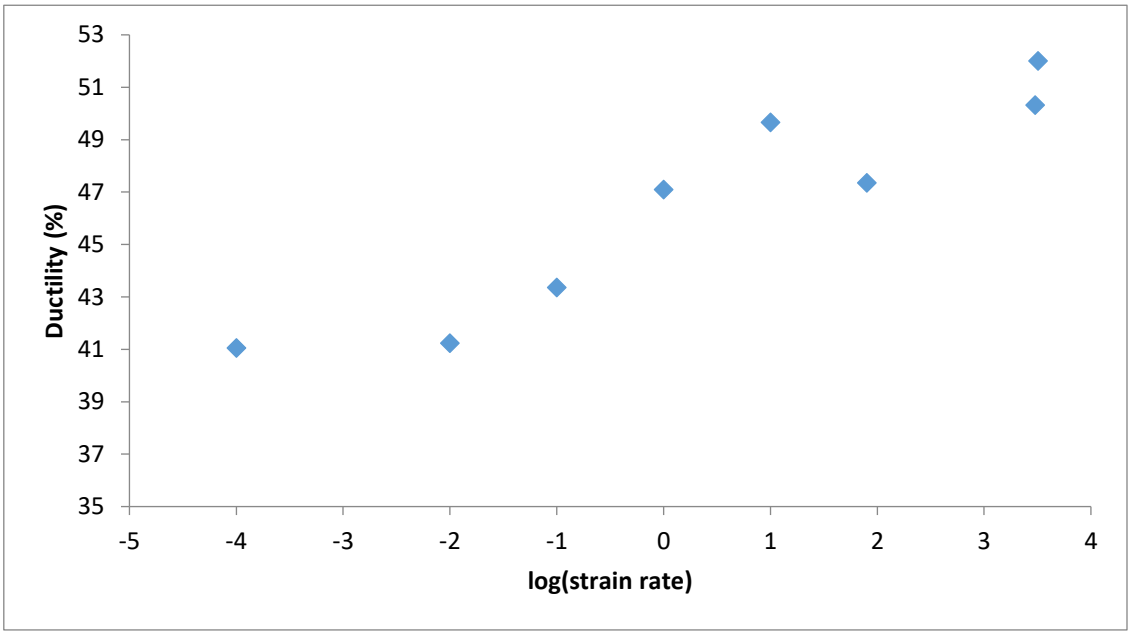

Figure 4.3: (c) continued

For HSLA 590, the ultimate tensile strength remained invariant until a strain rate of 50/sec at around 700 MPa. It increased significantly to 1400MPa, at a strain rate of 3200/sec. Hopkinson bar tensile plots have artificial peaks, leading to the UTS. These peaks have been noticed in some of the previous studies, but no explanations are provided for their occurrence. It may be a characteristic of the Hopkinson bar setup, and specimen gripping mechanism. In order to avoid incorrect yield strength values for Hopkinson bar tests, yield strengths were only calculated for servo-hydraulic tests (up to 80/sec). Yield strength showed a gradual increase when the strain rate increased from 10^{-3}/sec to 50/sec, with a significant increase to about 900 MPa at 80/sec. Ductility too, showed a 10% increase when the strain rate was increased from 10^{-3}/sec to 3200/sec. Interestingly, both ductility and strength increased with the increase in strain rate.

4.1.3 Fracture Profilometry

Figure 4.4 shows the optical images of fracture profile for HSLA 590 at 10^{-4}/sec and 3200/sec. Linear profile roughness parameter (R_L) was measured for both the cases.

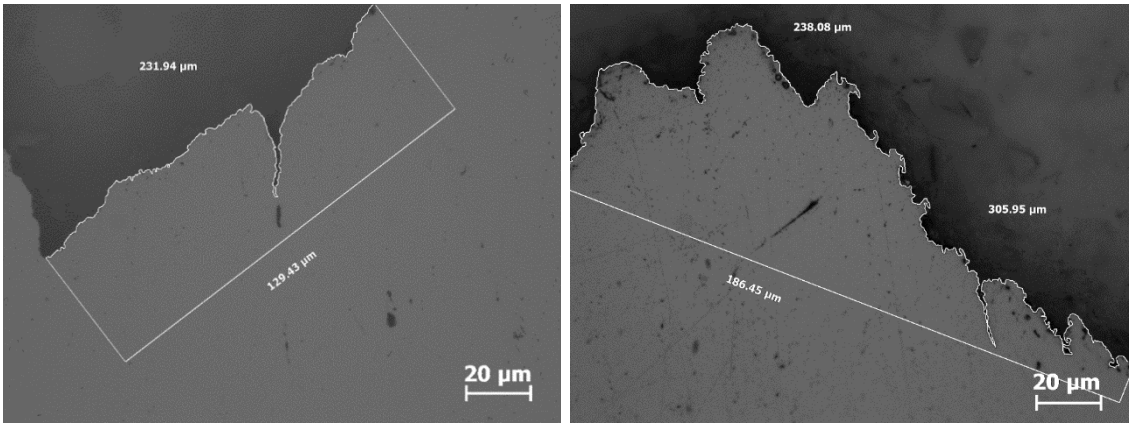

Figure 4.4: Shows the fracture profile with measurements on specimens tested at (a) 10^{-3}/sec and (b) 3200/sec

The R_L values for 10^{-4}/sec and 3200/sec were 1.79 and 2.91 respectively. A higher profile roughness value at 3200/sec strain rate, is consistent with the observed high ductility at 3200/sec.

4.1.4 Quantitative Fractography

Qualitative analysis of fractured surfaces for all strain rates showed predominantly ductile failure, with a high number density of voids. A quantitative study shows invariant values of area fraction, number per unit area of dimpled region, and dimple size. These values are shown in Table 4.1. As expected, ductile failure was observed in the HSLA 590 for all strain rates. Number density of dimples did not vary significantly with strain rate.

Table 4.1: Quantitative fractography data for HSLA 590

Strain rate (/sec)	$<A_A>$ dimpled region	$<N_A>$ dimpled (/mm^2) x 10^3	Average dimple size (μm)
10^{-4}	0.69 ± 0.01	174 ± 55	2.70 ± 0.42
50	0.76 ± 0.02	200 ± 46	2.52 ± 0.29
3200	0.61 ± 0.01	246 ± 68	2.28 ± 0.31

4.2 DUCTIBOR 500

4.2.1 Bulk Microstructure of Ductibor 500

"As received" microstructure of Ductibor 500 consists of ferrite and pearlite. Figure 4.5 shows the "as received" microstructure of Ductibor 500 prior to the hot-forming. The darker constituent in optical image corresponds to pearlite, whereas the brighter phase corresponds to the ferrite phase. In SEM micrographs, the brighter constituent is pearlite, whereas the darker phase is ferrite.

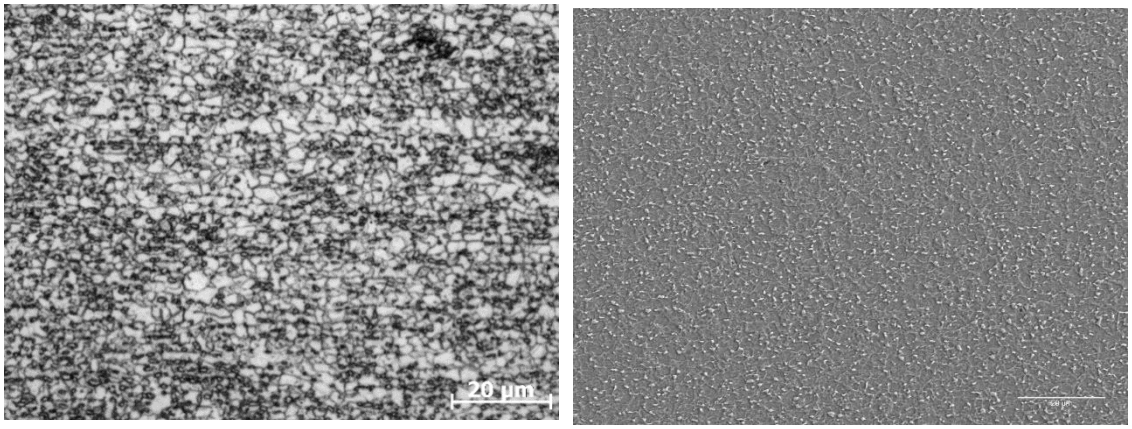

(a) (b)

Figure 4.5: As received (a) Optical (b) SEM micrographs of Ductibor 500

Figure 4.6 depicts the microstructures obtained after hot-stamping, under optical microscope and SEM.

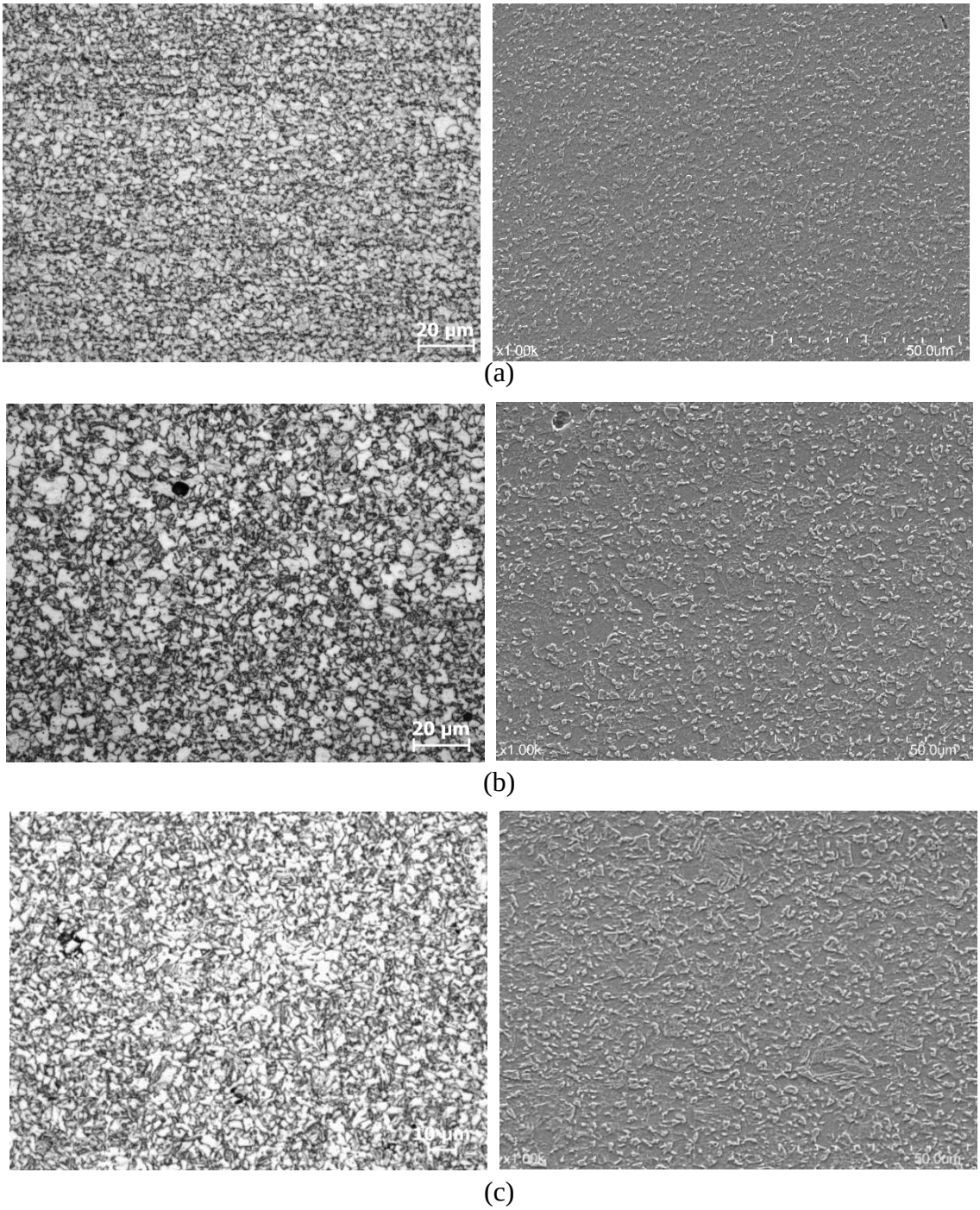

Figure 4.6: Shows the micrographs of DUCTIBOR 500 specimens austenitized at (a) 920°C for 7 minutes (b) 950°C for 15 minutes and (c) 980°C for 30 minutes. Micrographs on the left are optical micrographs, and that on the right are SEM micrographs.

Complex microstructures were observed after hot-stamping in Ductibor 500 with a mixture of various constituents, including ferrite (primary phase), pearlite and hard-constituents such as bainite and/or martensite (secondary constituents). Complete martensitic transformation could not be achieved after hot-stamping, due to lower hardenability of Ductibor 500 (requires much higher cooling rates for complete martensitic transformation). As seen in the above micrographs, secondary constituents (constituents with a relief in the SEM micrographs), appear to grow in size with increasing time and temperature of austenitization. Table 4.2 shows the volume fraction of the secondary constituents, and total surface area per unit volume of ferrite-secondary constituents interface.

Table 4.2: Volume fraction of secondary constituents and total surface area per unit volume of ferrite-secondary constituents interface for DUCTIBOR 500.

Hot-stamping parameters	$<V_V>$	$<S_V>$ (mm^2/mm^3)
920°C for 7 minutes	0.30 ± 0.05	752 ± 98
950°C for 15 minutes	0.28 ± 0.06	588 ± 83
980°C for 30 minutes	0.38 ± 0.05	870 ± 88

4.2.2 Uniaxial Tensile Test Results

Engineering stress vs engineering strain curves for quasi static strain rate tests are shown in figure 4.7 to figure 4.10. As received specimens and hot-forming process condition of 920°C for 7 minutes, shows yield point elongation, which disappears for the other process conditions of 950°C for 15 minutes and 980°C for 30 minutes.

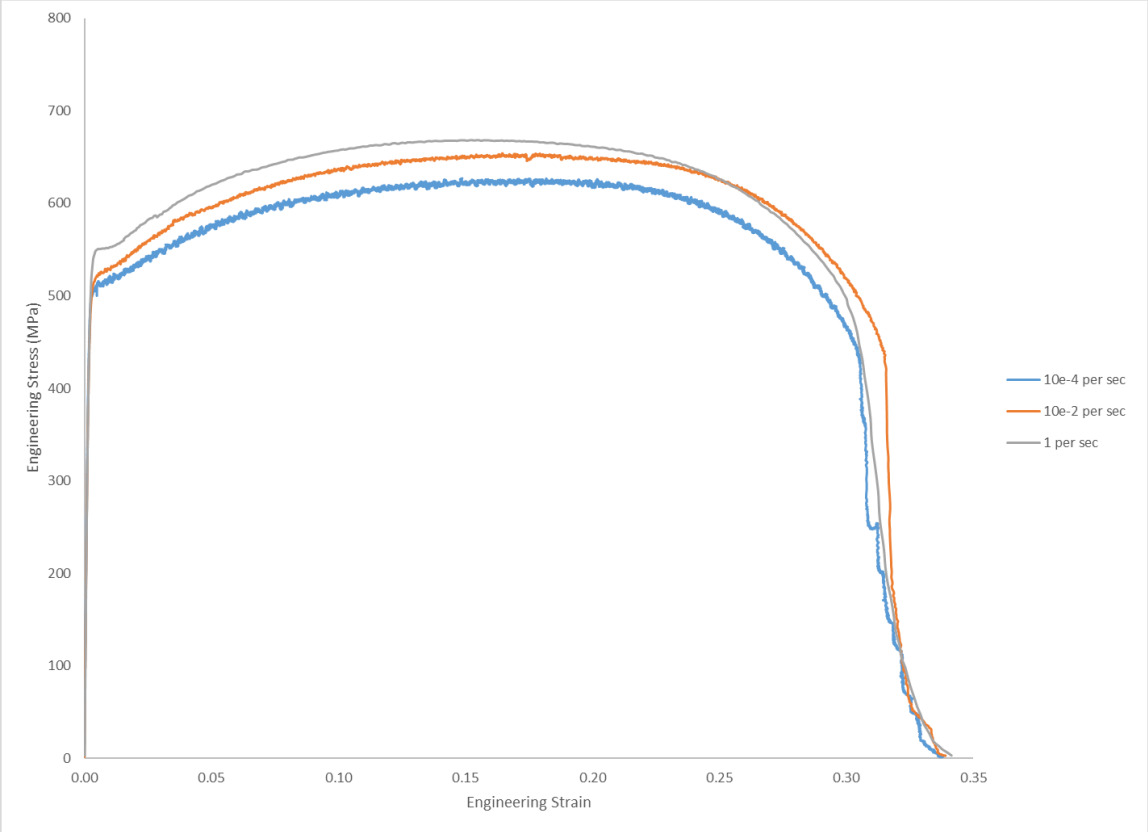

Figure 4.7: Engineering stress versus engineering strain curves for "as received" DUCTIBOR 500 at quasi-static strain rates.

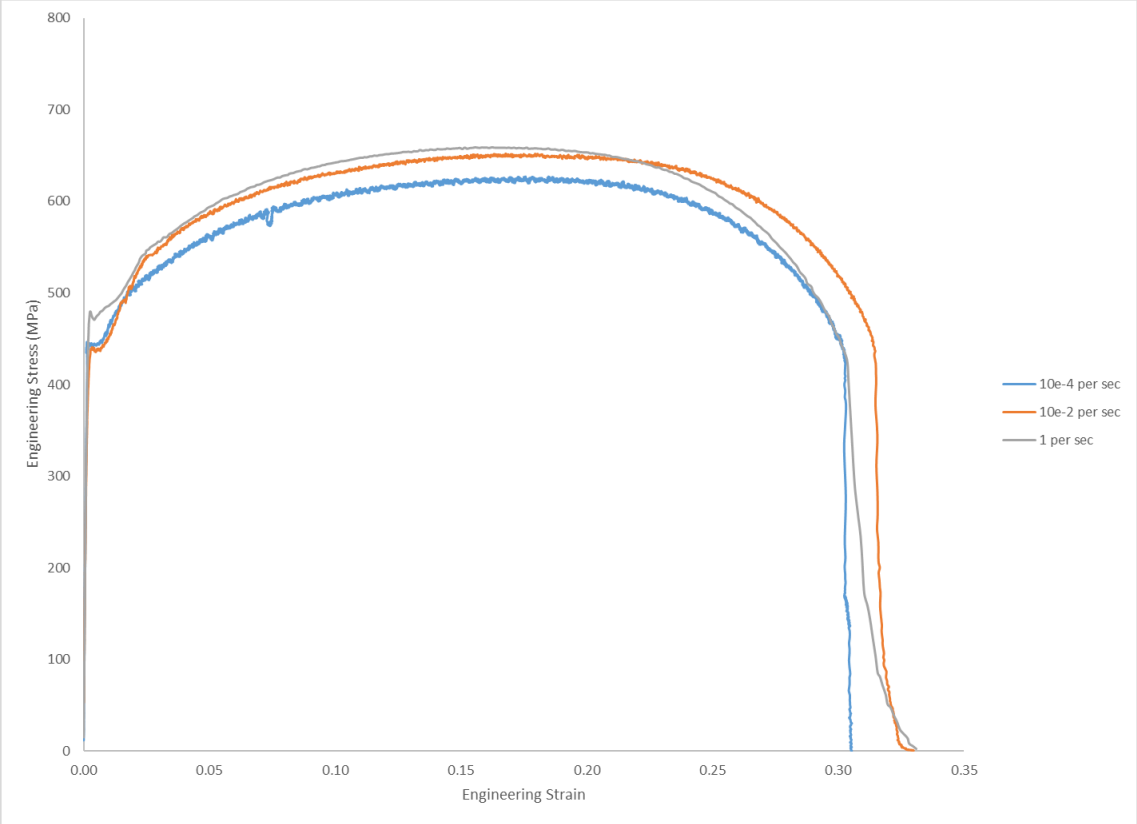

Figure 4.8: Engineering stress versus engineering strain curves for DUCTIBOR 500 hot-formed at 920°C for 7 minutes at quasi-static strain rates.

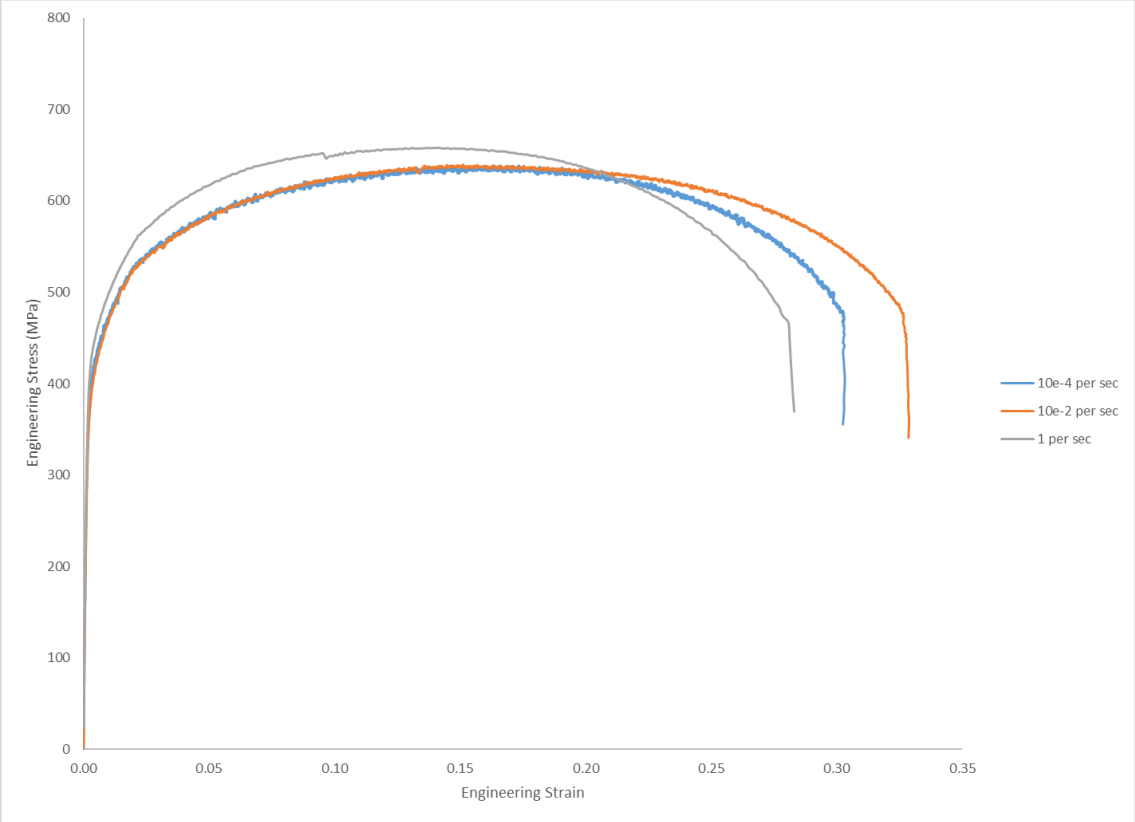

Figure 4.9: Engineering stress versus engineering strain curves for DUCTIBOR 500 hot-formed at 950°C for 15 minutes at quasi-static strain rates.

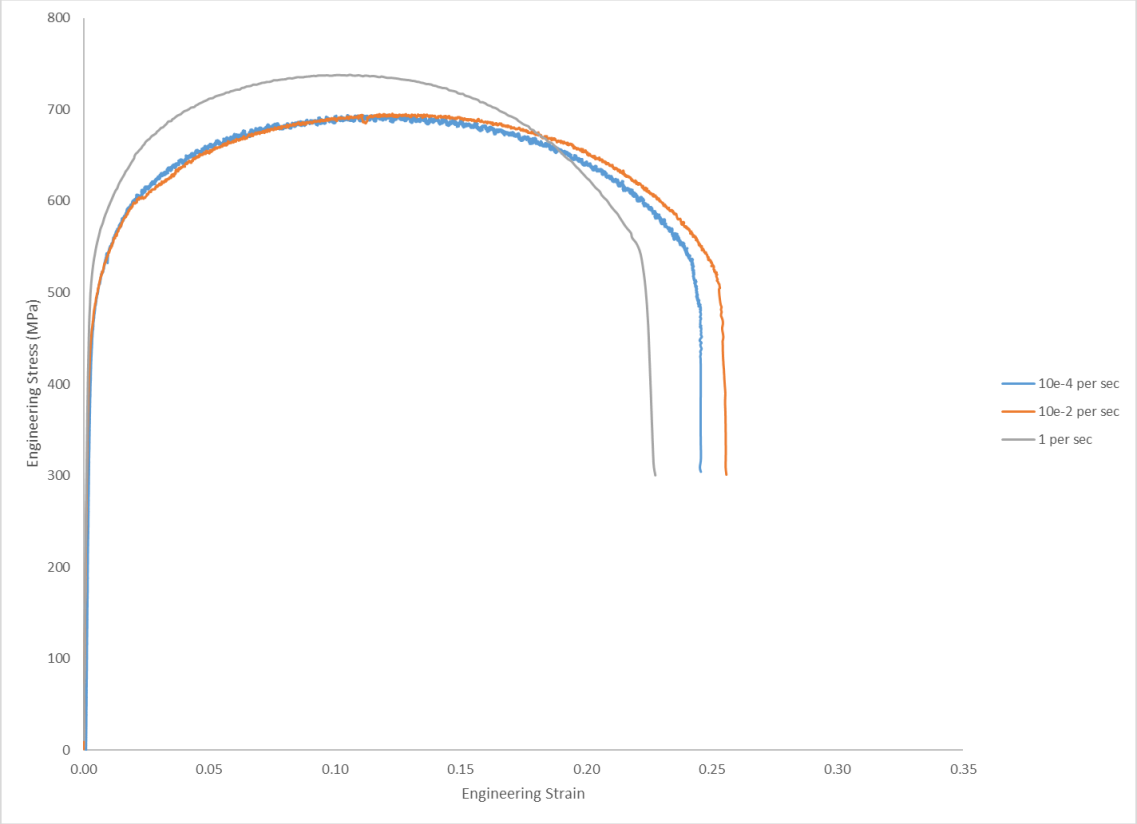

Figure 4.10: Engineering stress versus engineering strain curves for DUCTIBOR 500 hot-formed at 980°C for 30 minutes at quasi-static strain rates.

Yield point elongation observed for 920°C for 7 minutes is because of the incomplete austenitization of Ductibor 500 at 920°C for 7 minutes. Pearlite remains in the microstructure at 920°C for 7 minutes, thereby resulting in yield point elongation phenomena. An increase in ultimate tensile strength with increasing temperature and time of austenitization is observed. Figure 4.11 shows the plots for 10^{-4}/sec and 1000/sec. Plots shown for 1000/sec are from the raw data, without any averaging. Hence, these plots are not smooth. Strength values at 1000/sec are significantly higher compared to the quasi-static strain rates.

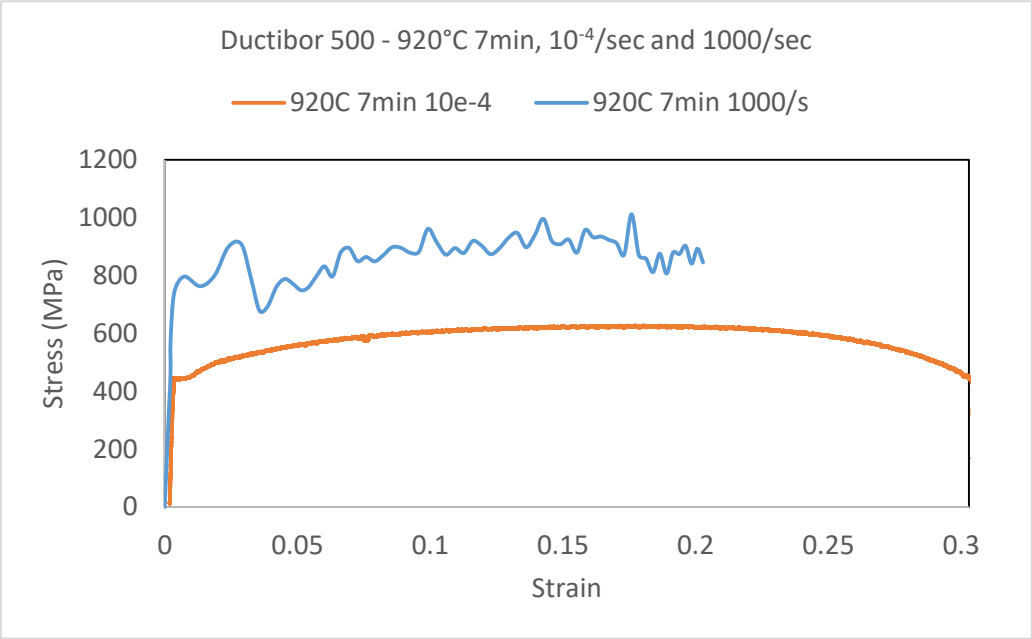

(a)

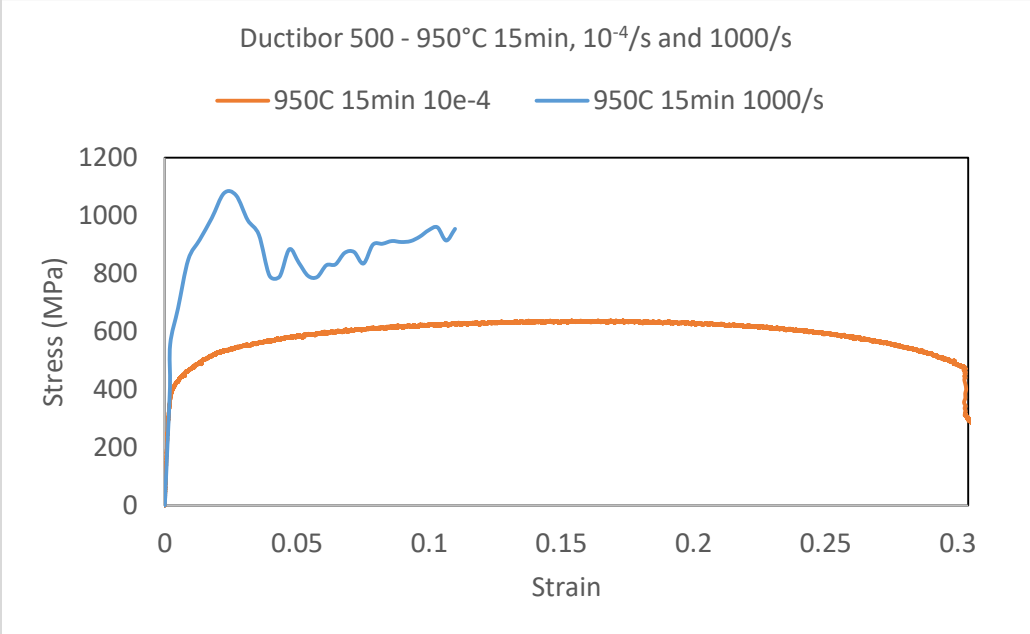

(b)

Figure 4.11: Engineering stress vs engineering strain at 10^{-4}/sec and 1000/sec for DUCTIBOR 500 hot-formed at (a) 920°C for 7 minutes (b) 950°C for 15 minutes and (c) 980°C for 30 minutes

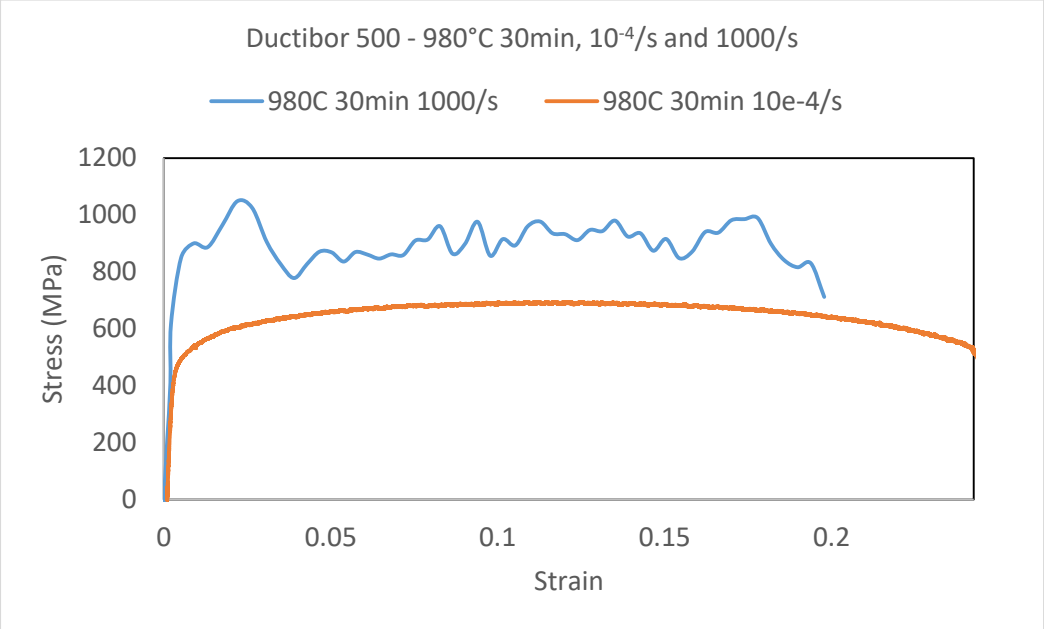

Figure 4.11: (c) continued

Variations in 0.2% offset yield strength, ultimate tensile strength and ductility are plotted against the logarithmic values of strain rate in Figure 4.12. Each data point corresponds to a single tensile test. It is clear that, the yield strength, ultimate tensile strength and ductility, are strain rate sensitive. For all time-temperature combinations of hot-forming, these values seldom changed until a strain rate of 1/sec. At 1000/sec strain rate, yield strength and ultimate tensile strength increased, almost by a factor of 1.5. An increase in ductility was also observed. Also, strength values for the different hot-forming processing conditions are almost similar at quasi-static strain rates. This further suggests the robustness of hot-stamping process, for the processing conditions used in this research.

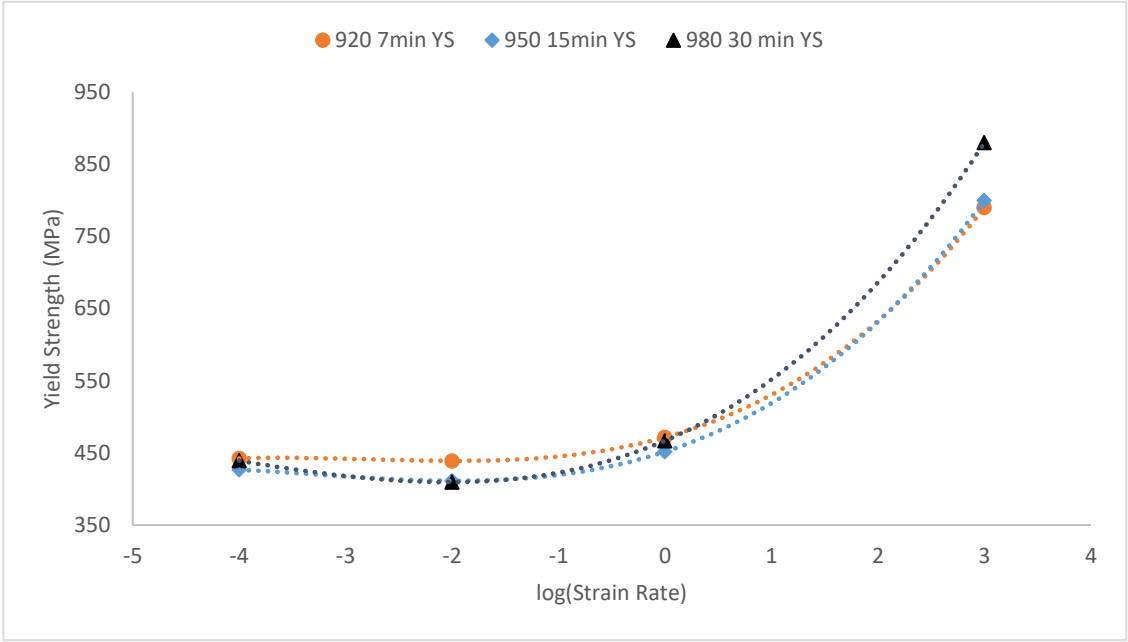

(a)

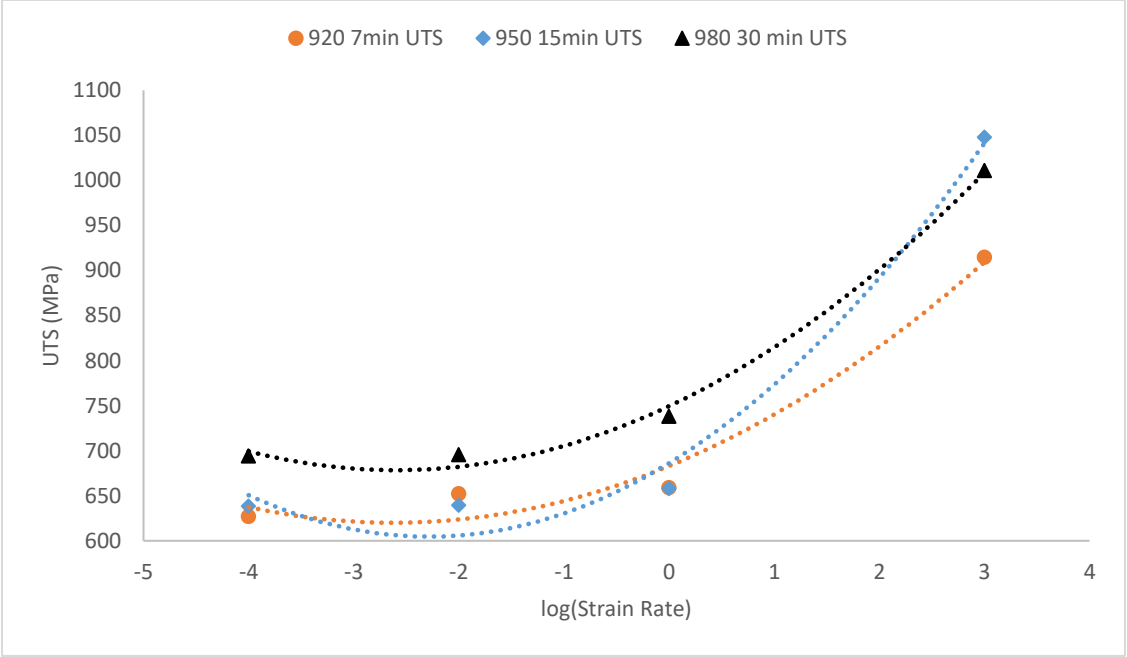

(b)

Figure 4.12: Shows (a) Yield Strength vs log(strain rate) (b) UTS vs log(strain rate) and (c) Ductility vs log(strain rate) for DUCTIBOR 500.

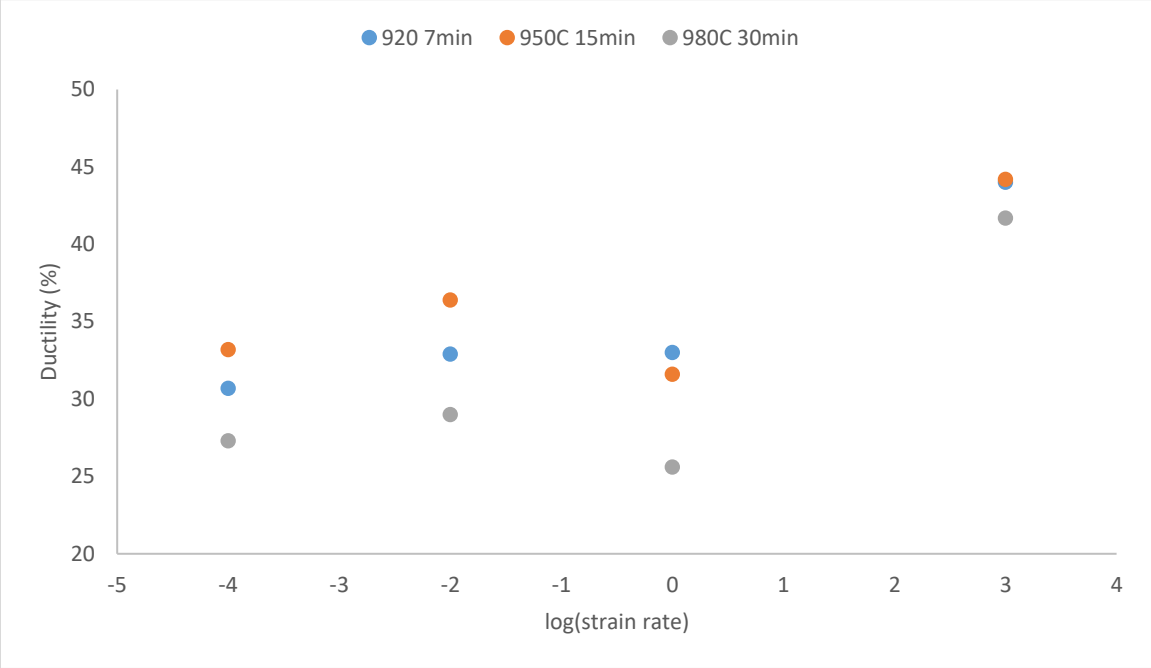

Figure 4.12: (c) continued

4.2.3 Quantitative Fractography

Figure 4.13 shows representative fractured surfaces of Ductibor 500. Regions of ductile failure, brittle failure and pullouts were identified in the fractured surfaces. These morphologies correspond to the different failure mechanisms. They were quantitatively studied using fractography. For all strain rates and hot-forming parameters, ductile failure remained the dominant mode of failure. Table 4.3 shows the variation in area fraction of different fracture morphologies. Table 4.4 shows the number fractions of dimples and pullouts for specimens treated at 920°C for 7min and 980°C for 30min respectively. All the errors reported, correspond to a 95% confidence interval.

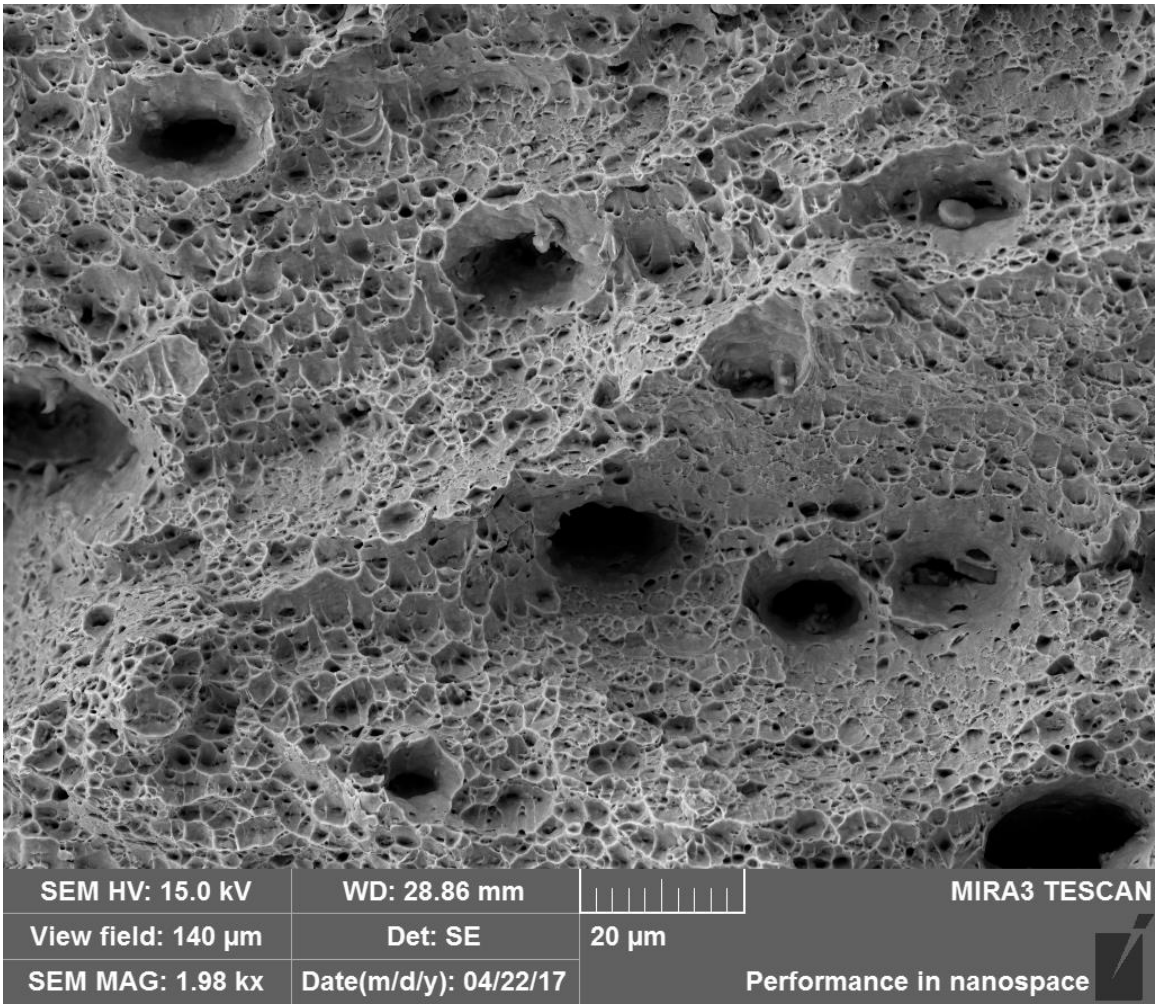

(a)

Figure 4.13: Fracture surfaces of DUCTIBOR 500 hot-formed at 920°C for 7 minutes, pulled at (a) 10^{-4}/sec, (b) 1000/sec, and hot-formed at 980°C for 30 minutes, pulled at (c) 10^{-4}/sec and (d) 1000/sec.

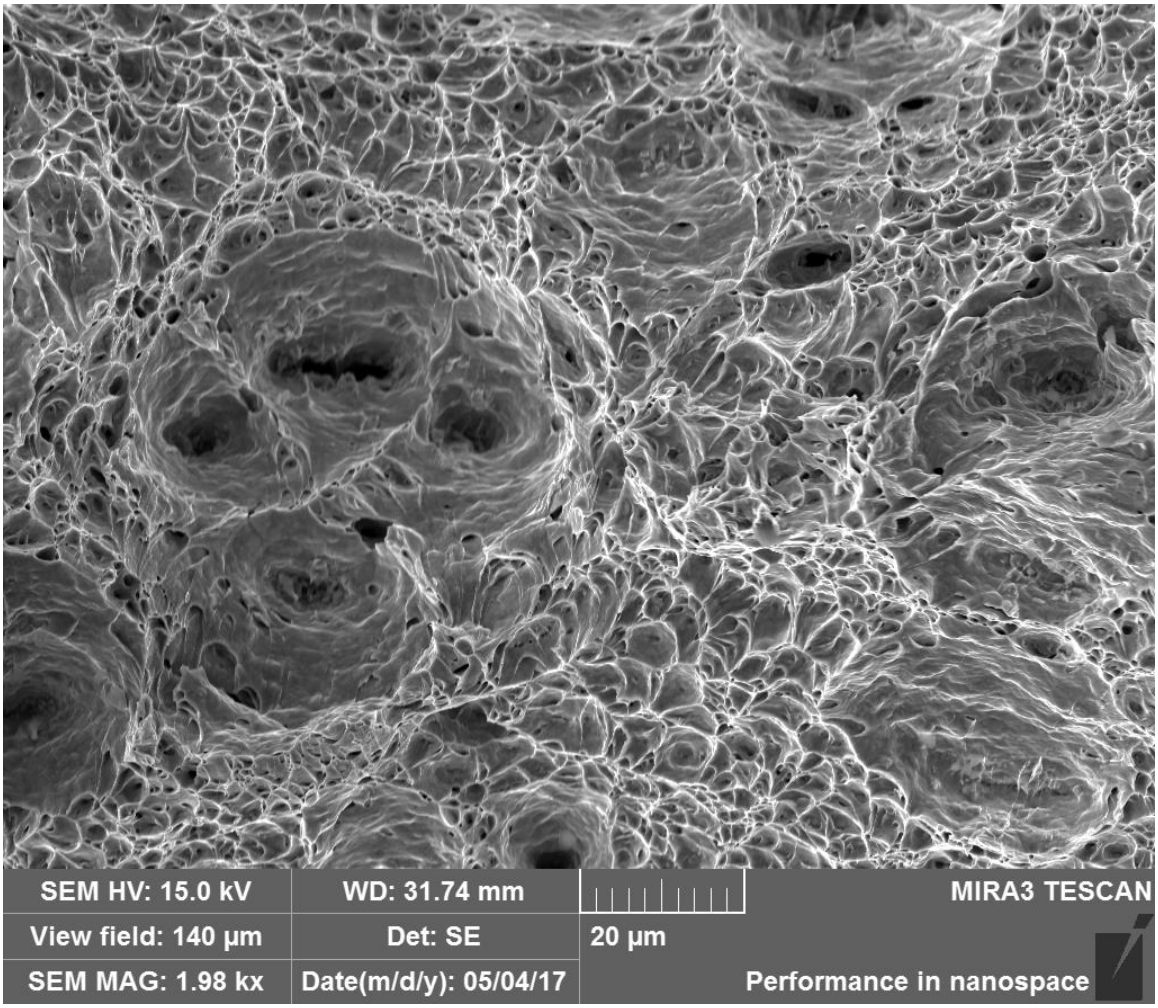

Figure 4.13: (b) continued

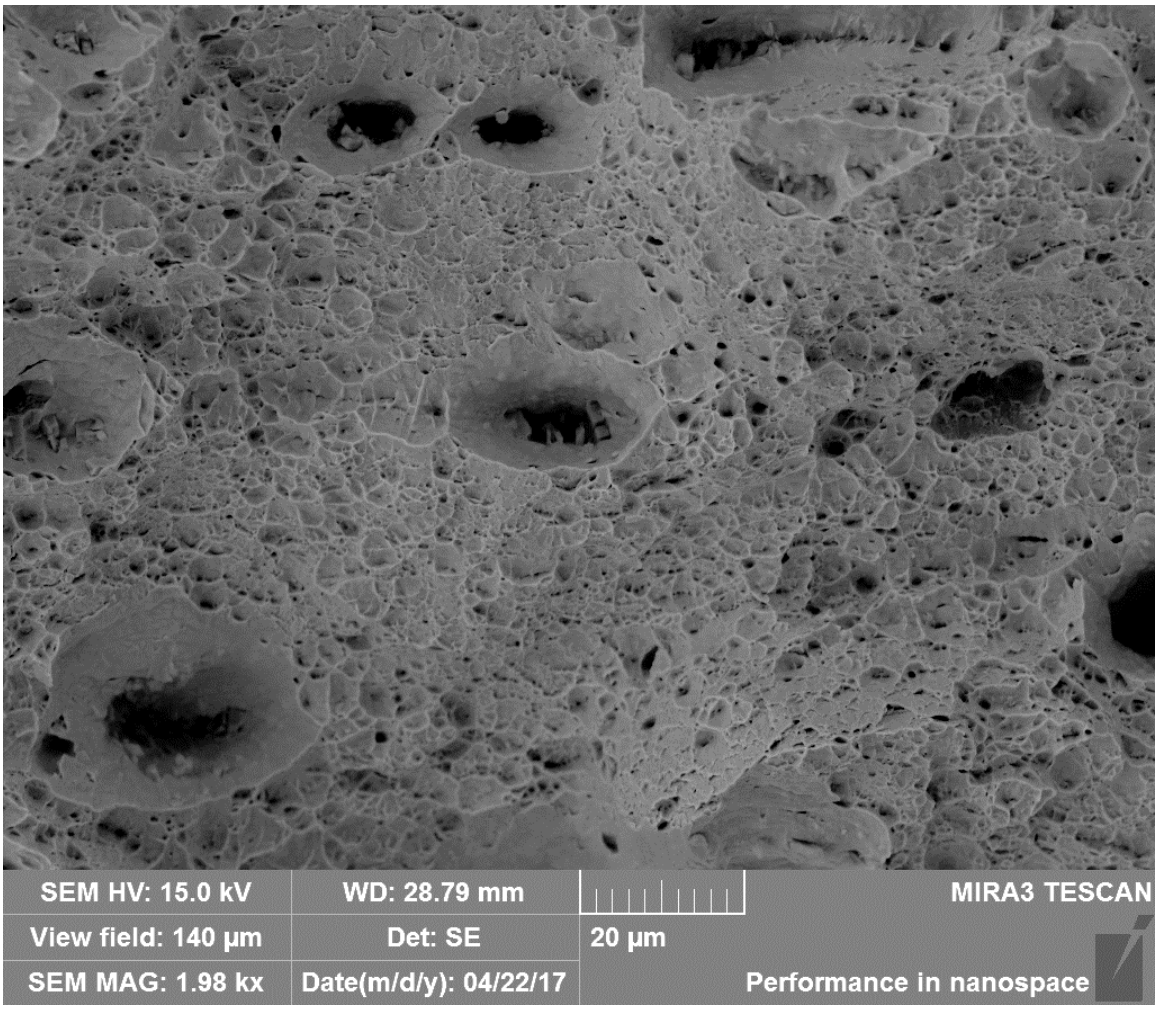

Figure 4.13: (c) continued

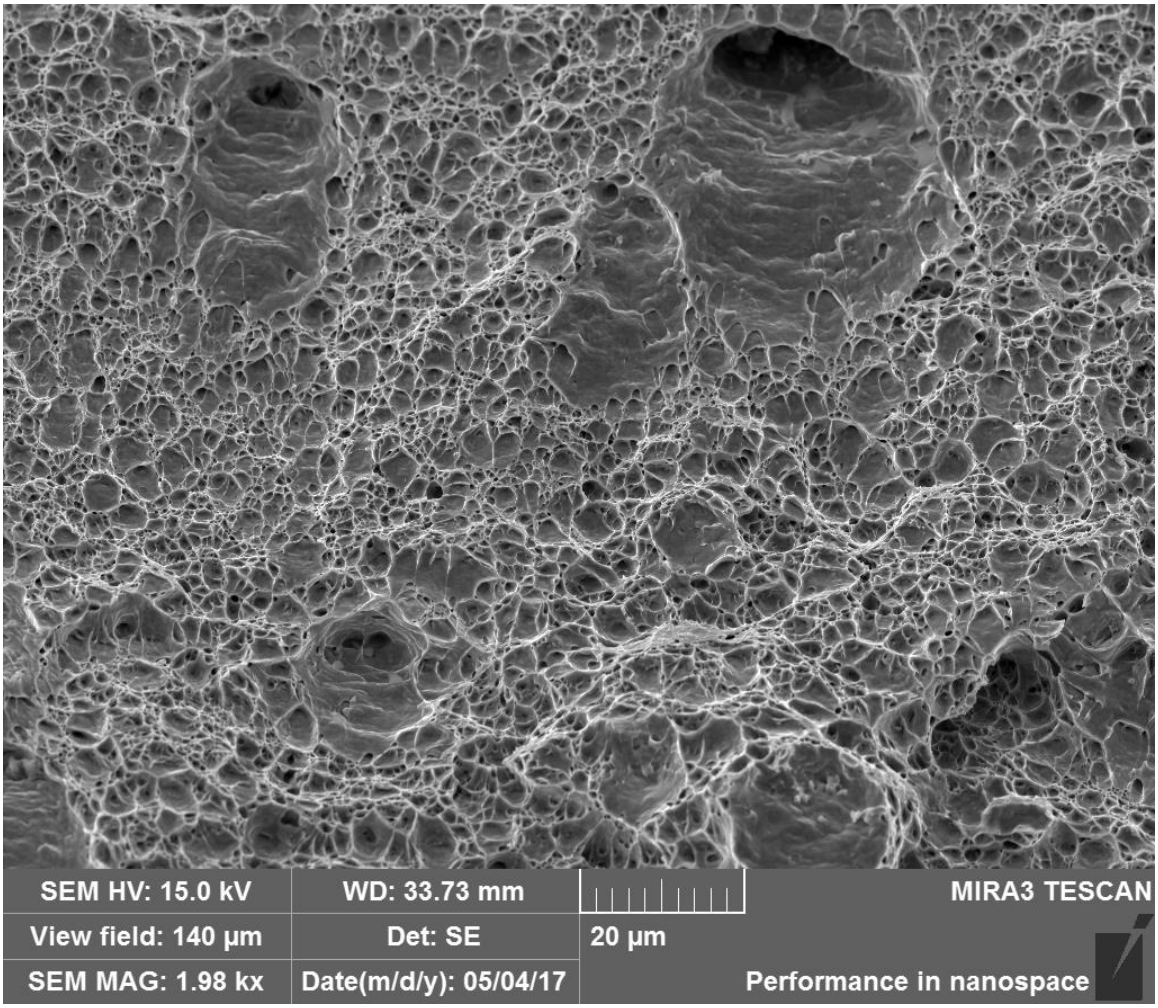

Figure 4.13: (d) continued

Table 4.3: Shows the Area fraction of dimpled and brittle regions for specimens hot-formed at (a) 920°C for 7 minutes and (b) 980°C for 30 minutes for DUCTIBOR 500.

(a)

Temp - Time	Strain rate(/sec)	$<A_A>$ dimple	Error	$<A_A>$ brittle	Error	$<A_A>$ pullout	error
920°C, 7min	10-4	0.66	0.09	0.34	0.09	0.21	0.08
	1000	0.56	0.08	0.43	0.09	0.12	0.06

(b)

Temp - Time	Strain rate	$<A_A>$ dimple	Error	$<A_A>$ brittle	Error	$<A_A>$ pullout	error
980°C, 30min	10-4	0.79	0.01	0.21	0.09	0.12	0.05
	1000	0.83	0.06	0.17	0.06	0.02	0.002

Table 4.4: Table shows the number density of dimples and pullouts in specimens hot-formed at (a) 920°C for 7 minutes and (b) 980°C for 30 minutes for DUCTIBOR 500.

(a)

Time – Temp combination	Strain Rate(/sec)	$<N_A>$ dimples X 10^3 (/mm^3)	error	$<N_A>$ pullout x 10^3 (/mm^3)	error
920°C, 7min	10^{-4}	81	15	0.35	0.15
	1000	40	11	0.59	0.23

(b)

Time-Temp combination	Strain Rate(/sec)	$<N_A>$ dimples X 10^3 (/mm^3)	error	$<N_A>$ pullout x 10^3 (/mm^3)	error
980°C, 30min	10^{-4}	71	16	0.27	0.17
	1000	153	27	0.20	0.02

For both the hot-forming parameters, area fractions of dimpled and flat regions, remained invariant with the strain rates. Area fraction of pullouts decreased with increasing strain rate. At a strain rate of 1000/sec, area fraction and number density of dimpled region significantly increased with an increase in temperature and time of austenitization. The

failure was more ductile at a higher time and temperature of austenitization. Number densities of pullouts remained invariant over all the strain rates, as well as time-temperature combinations of austenitization. At a nominal condition of 920°C for 7min, number density of dimples reduced by half with an increase in strain rate. However, at 980°C for 30min, number density of dimples almost doubled, with an increase in strain rate.

Average dimple sizes were also estimated for each case. Table 4.5 shows the average dimple size estimates for Ductibor 500.

Table 4.5: Shows the estimates for average dimple size (in μm) on the fracture surfaces for DUCTIBOR 500.

Processing Condition	Strain Rate (/sec)	Average Dimple Size (μm)
920°C for 7 minutes	10^{-4}	3.9 ± 0.4
	10^{3}	5.6 ± 0.7
980°C for 30 minutes	10^{-4}	4.2 ± 0.5
	10^{3}	2.9 ± 0.3

4.3 USIBOR 1500

4.3.1 Bulk Microstructure of Usibor 1500

Figure 4.14 shows the SEM micrograph of "as received" steel sheet. "As received" sheet of Usibor 1500 (prior to the hot-forming process) had a ferrite-pearlite microstructure. Pearlite islands, appearing bright, were randomly distributed in the

microstructure. All the micrographs show the cross-section containing transverse – thickness directions, thickness direction being vertical axis.

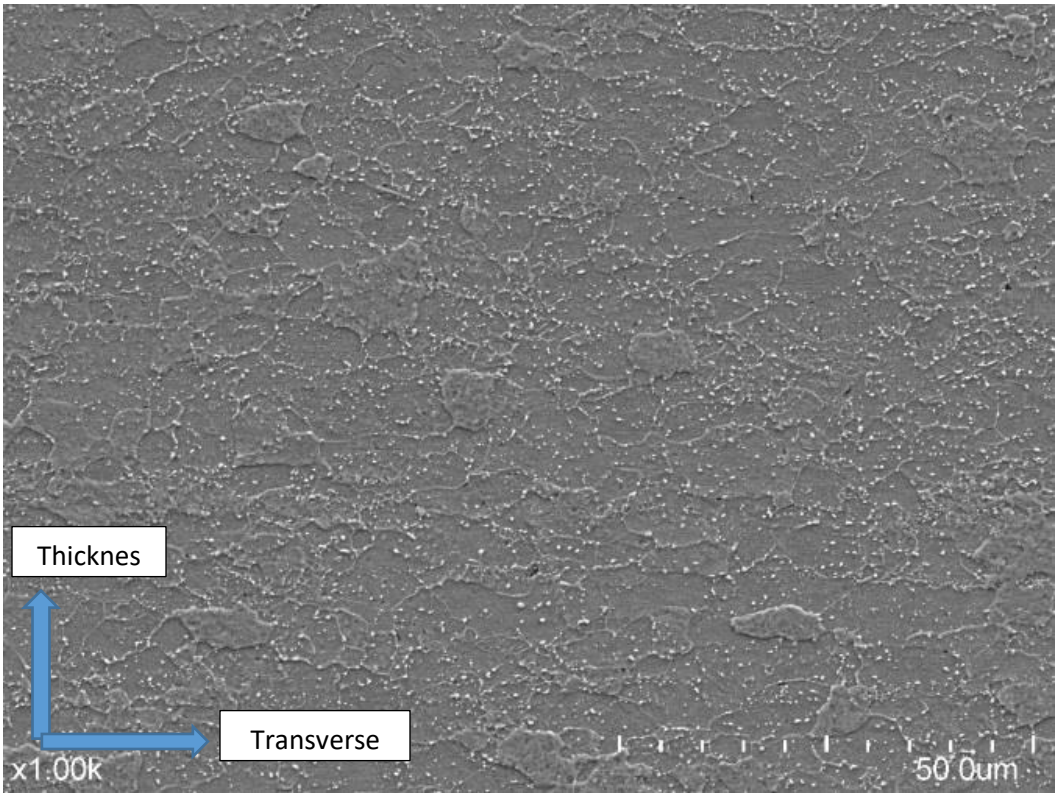

Figure 4.14: Shows a representative SEM micrograph for USIBOR 1500 in “as received” condition.

Blanks of Usibor 1500 were hot-stamped as discussed in section 3.2.2. Completely martensitic microstructures were observed for all the hot-forming parameters. Complete austenitization was achieved, as the temperatures were well above the Ac_3 temperature, and the blanks were held at those temperatures for long enough time. High quenching rate (~ 40°C/s), resulted in fully martensitic microstructures. Figure 4.15 shows the SEM microstructures of hot-stamped Usibor 1500.

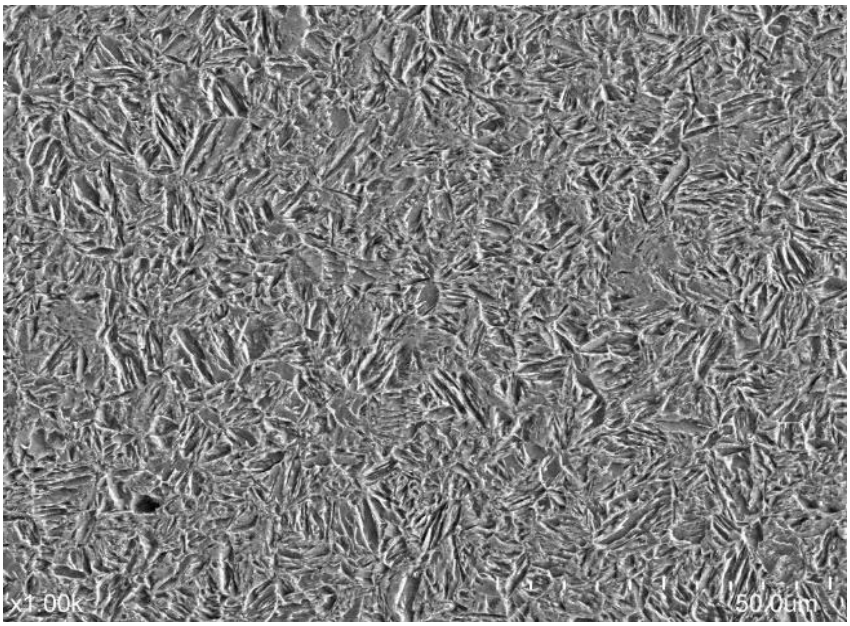

(a)

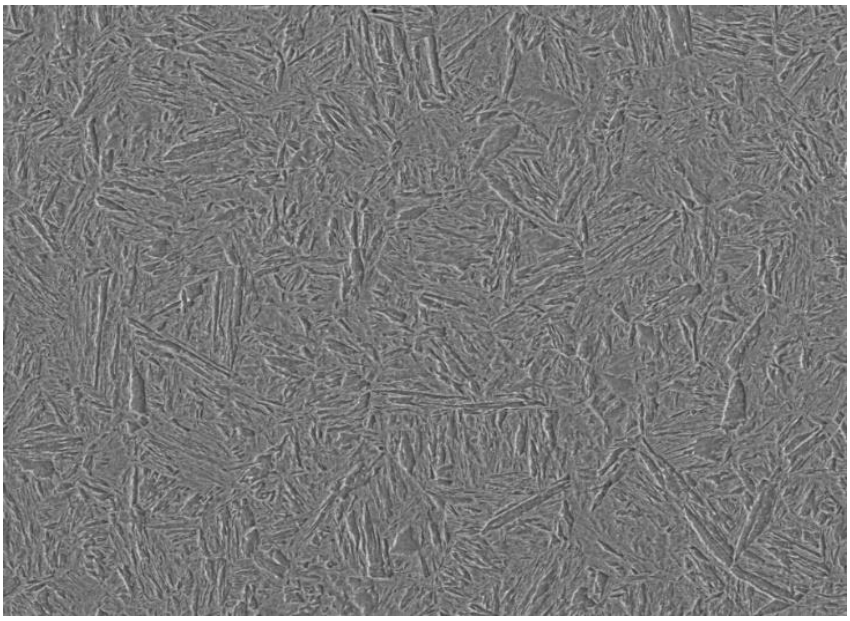

(b)

Figure 4.15: Shows the SEM micrographs of USIBOR 1500 hot-formed at (a) 920°C for 7 minutes (b) 950°C for 15 minutes and (c) 980°C for 30 minutes

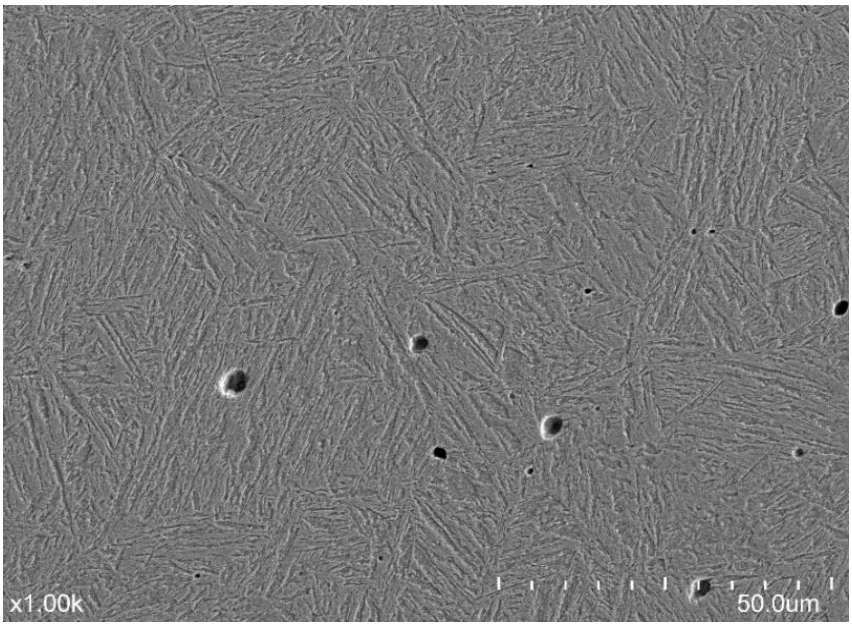

Figure 4.15: (c) continued

Martensite laths appear to grow finer with increasing temperature and time of austenitization. Total surface area per unit volume (S_V) of martensite – martensite (α' – α') interface are shown in Table 4.6.

Table 4.6: Shows the values of $<S_V>$ of martensite-martensite interface for USIBOR 1500.

Hot-stamping parameters	$<S_V>$ (mm^2/mm^3)
920°C for 7 minutes	132 ± 14
950°C for 15 minutes	197 ± 19
980°C for 30 minutes	215 ± 15

4.3.2 Uniaxial Tensile Test Results

Combined engineering stress vs strain curves at quasi-static strain rates for Usibor 1500 are shown in figure 4.16 to figure 4.19. Yield strength values in figure 4.20 are obtained after modulus correction.

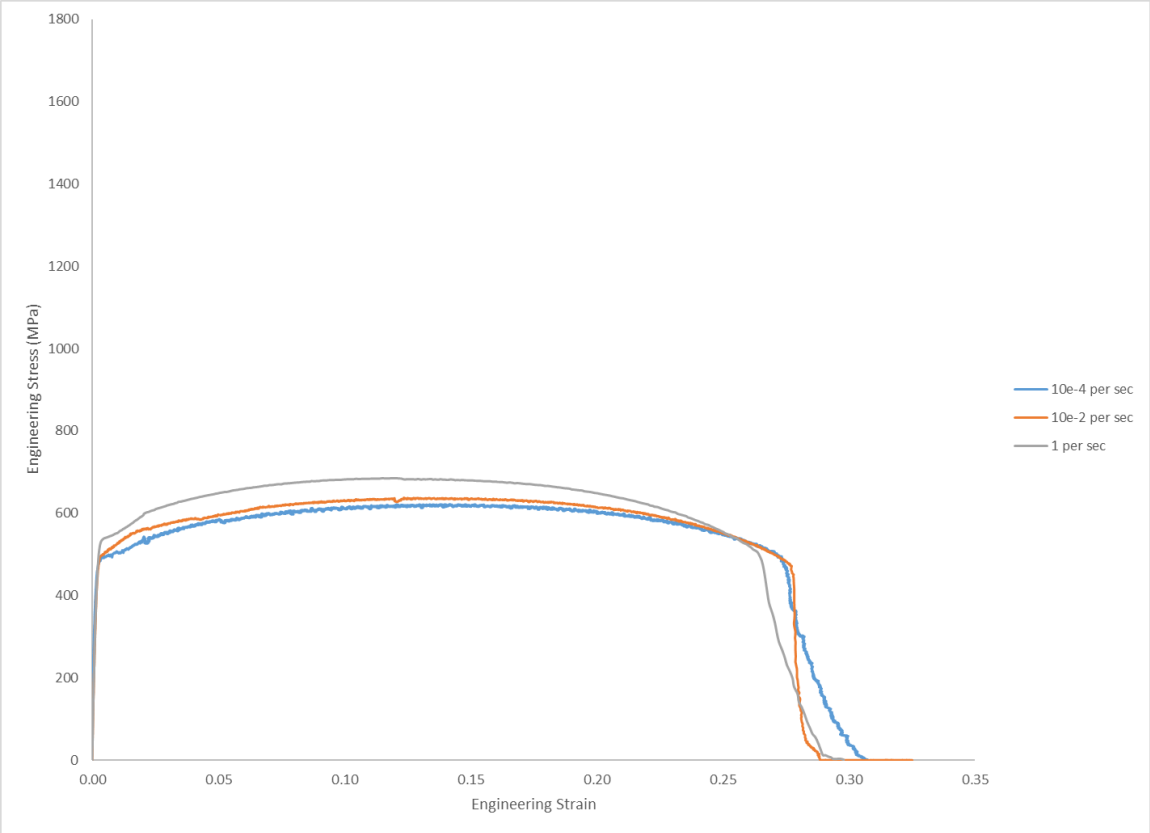

Figure 4.16: Engineering stress versus engineering strain curves for “as received” USIBOR 1500.

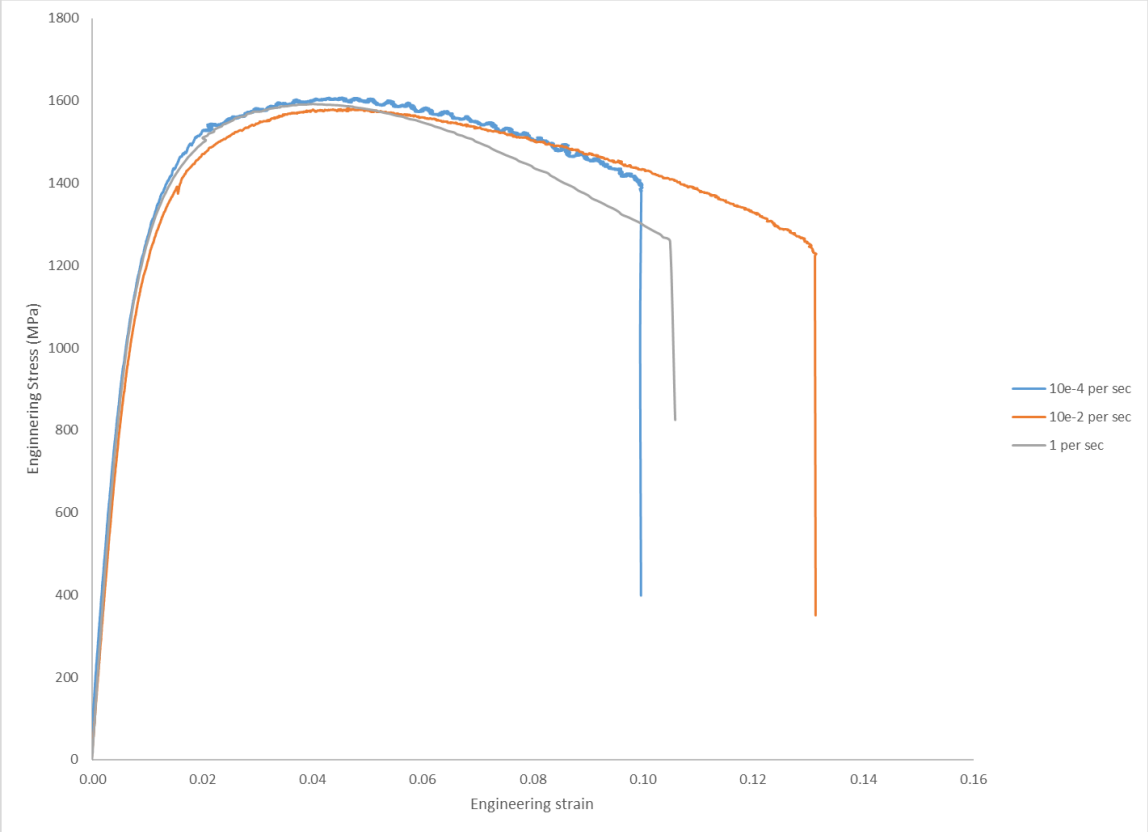

Figure 4.17: Engineering stress versus engineering strain curves for USIBOR 1500 hot-formed at 920°C for 7 minutes at quasi-static strain rates.

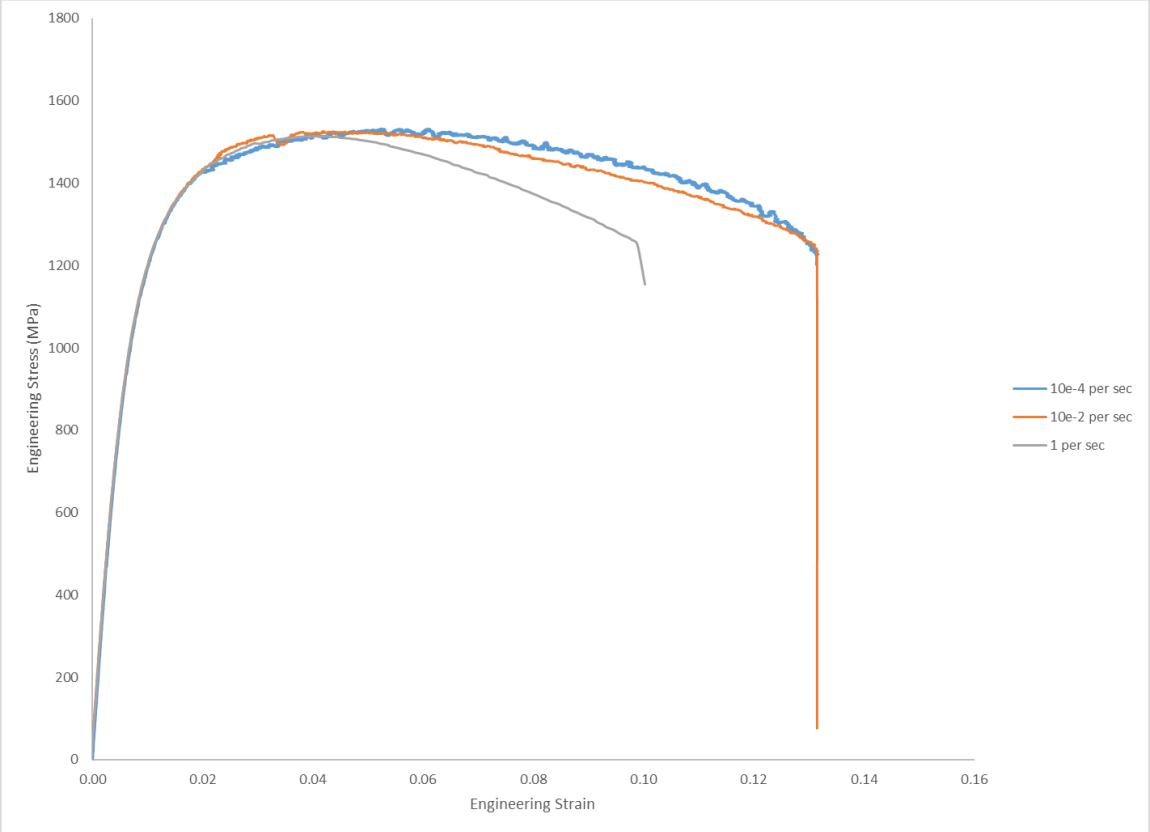

Figure 4.18: Engineering stress versus engineering strain curves for USIBOR 1500 hot-formed at 950°C for 15 minutes at quasi-static strain rates.

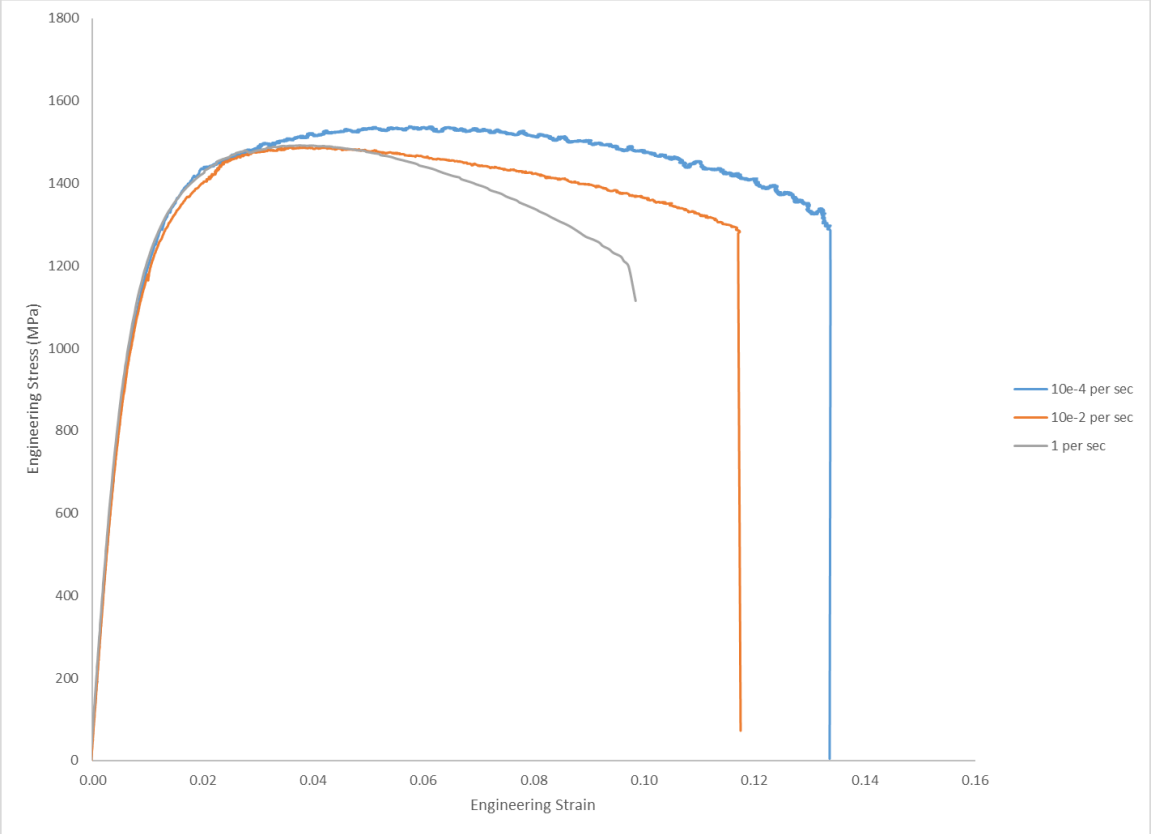

Figure 4.19: Engineering stress versus engineering strain curves for USIBOR 1500 hot-formed at 980°C for 30 minutes at quasi-static strain rates.

0.2% offset Yield strengths (YS), ultimate tensile strengths (UTS) and ductilities are plotted against the logarithmic values of strain rate in figure 4.20. Yield Strength and UTS are significantly higher than Ductibor 500, due to completely martensitic microstructures in the case of Usibor 1500. However, ductility when compared to Ductibor 500, as expected, was less. The strength values varied insignificantly until a strain rate of 1/sec (values were within 5% range). A significant increase in strength levels were seen at 1000/sec strain rate. The nominal condition of 920°C for 7 minutes showed the highest strength values across all the strain rates. Ductility increased slightly at 1000/sec.

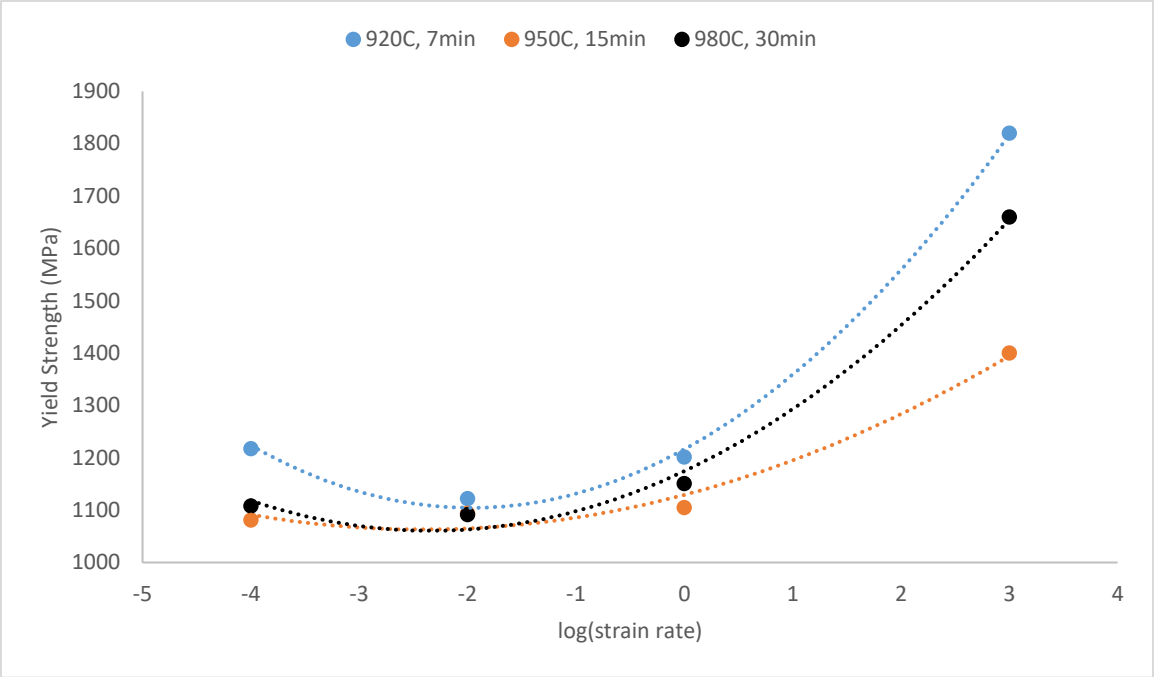

(a)

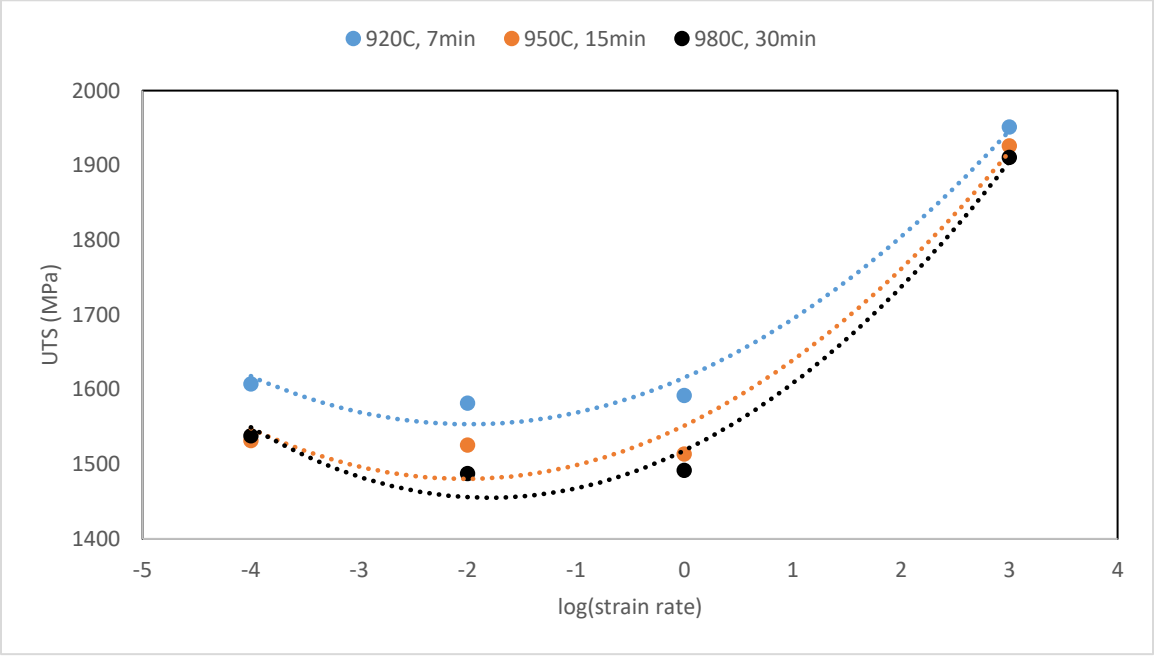

(b)

Figure 4.20: Plots for (a) YS vs log(strain rate), (b) UTS vs log(strain rate) and (c) Ductility vs log(strain rate) for USIBOR 1500.

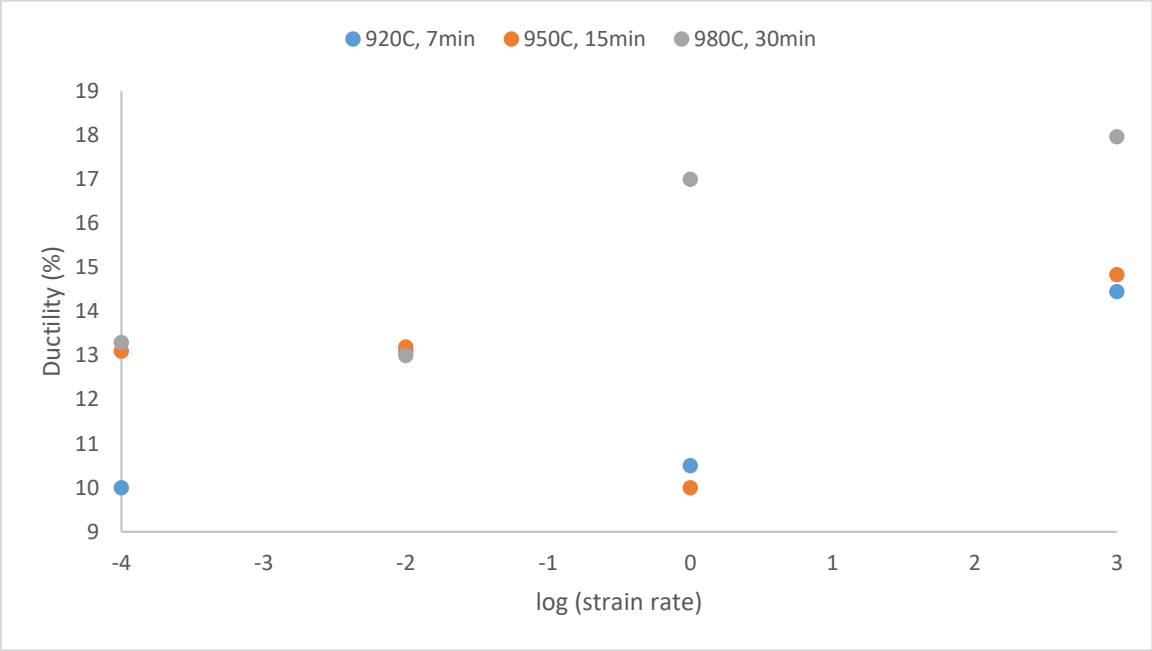

Figure 4.20: (c) continued

4.3.3 Quantitative Fractography

Representative fractured surfaces for Usibor 1500 are shown in figure 4.21. Different morphologies, corresponding to different modes of failure, were quantitatively studied using fractography. For all strain rates and hot-forming parameters, qualitative analysis of the fractured surfaces show ductile failure as the predominant mode of failure. Table 4.7 shows the area fraction of dimpled region, brittle region, and inclusion pullouts for Usibor 1500. Table 4.8 shows the number density of dimples and pullouts. All the errors correspond to a 95% confidence interval. Table 4.9 shows the dimple size estimates for Usibor 1500.

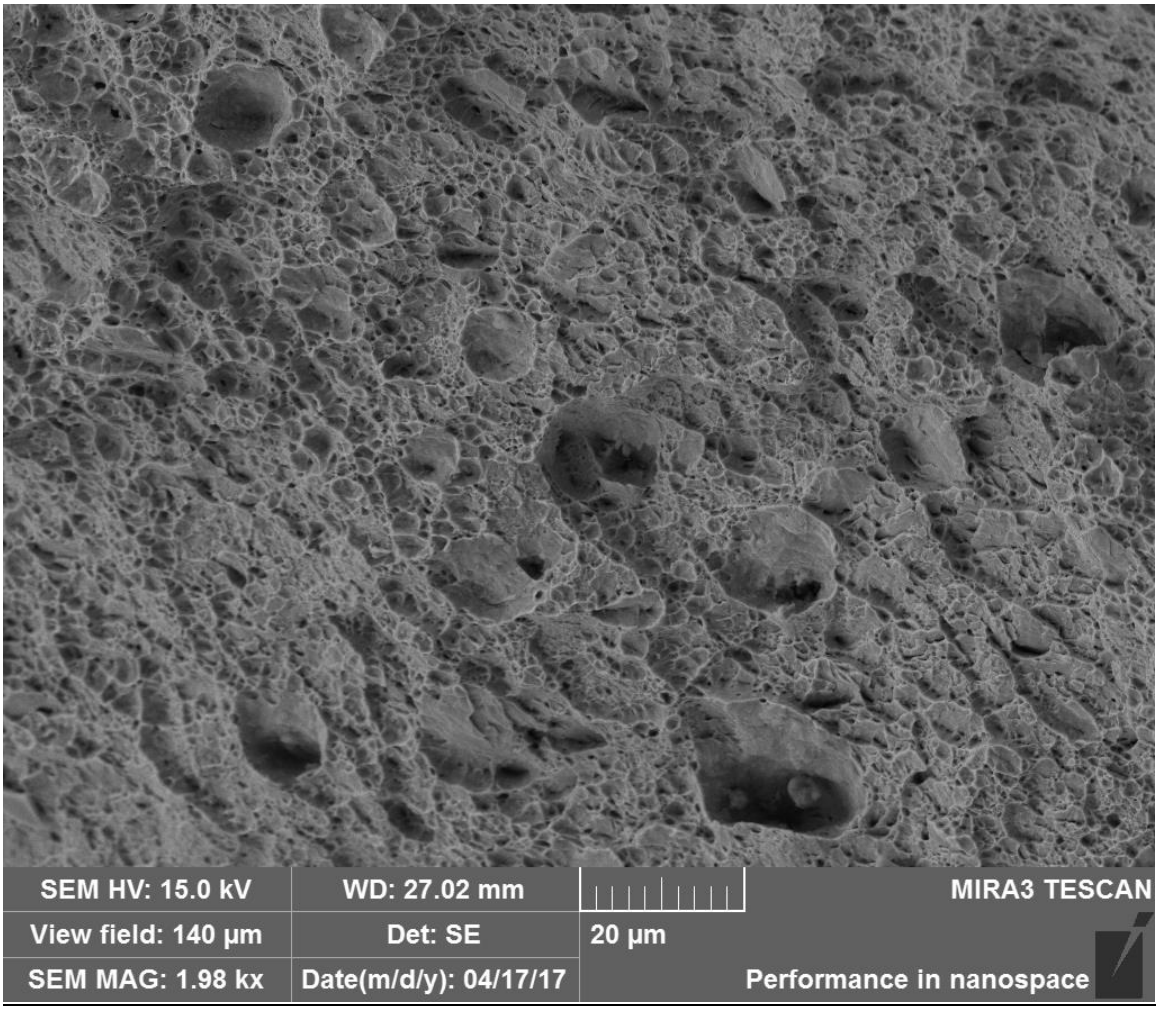

(a)

Figure 4.21: Fracture surfaces of USIBOR 1500 hot-formed at 920°C for 7 minutes, pulled at (a) 10^{-4}/sec, (b) 1000/sec, and hot-formed at 980°C for 30 minutes, pulled at (c)10^{-4}/sec and (d) 1000/sec.

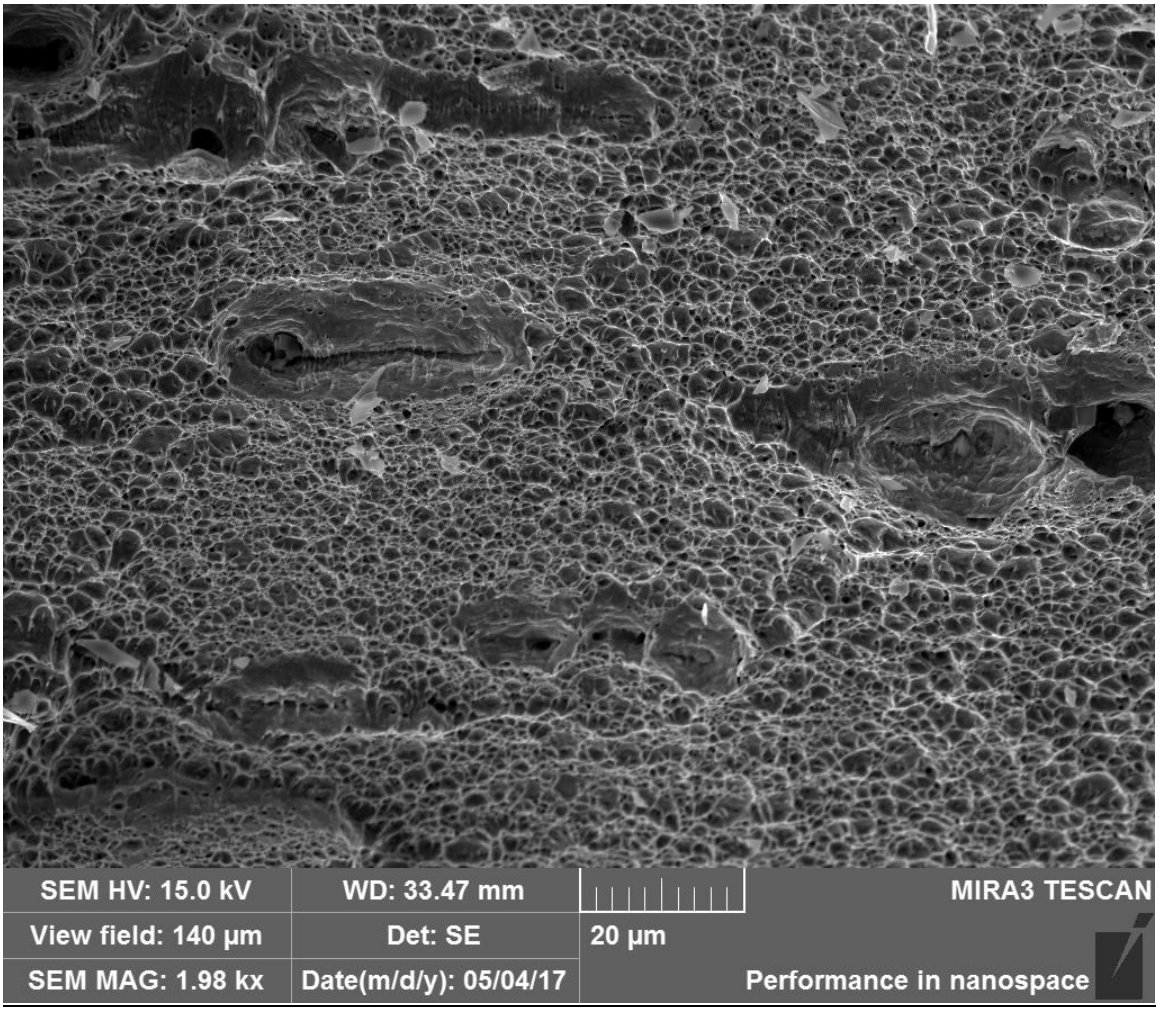

Figure 4.21: (b) continued

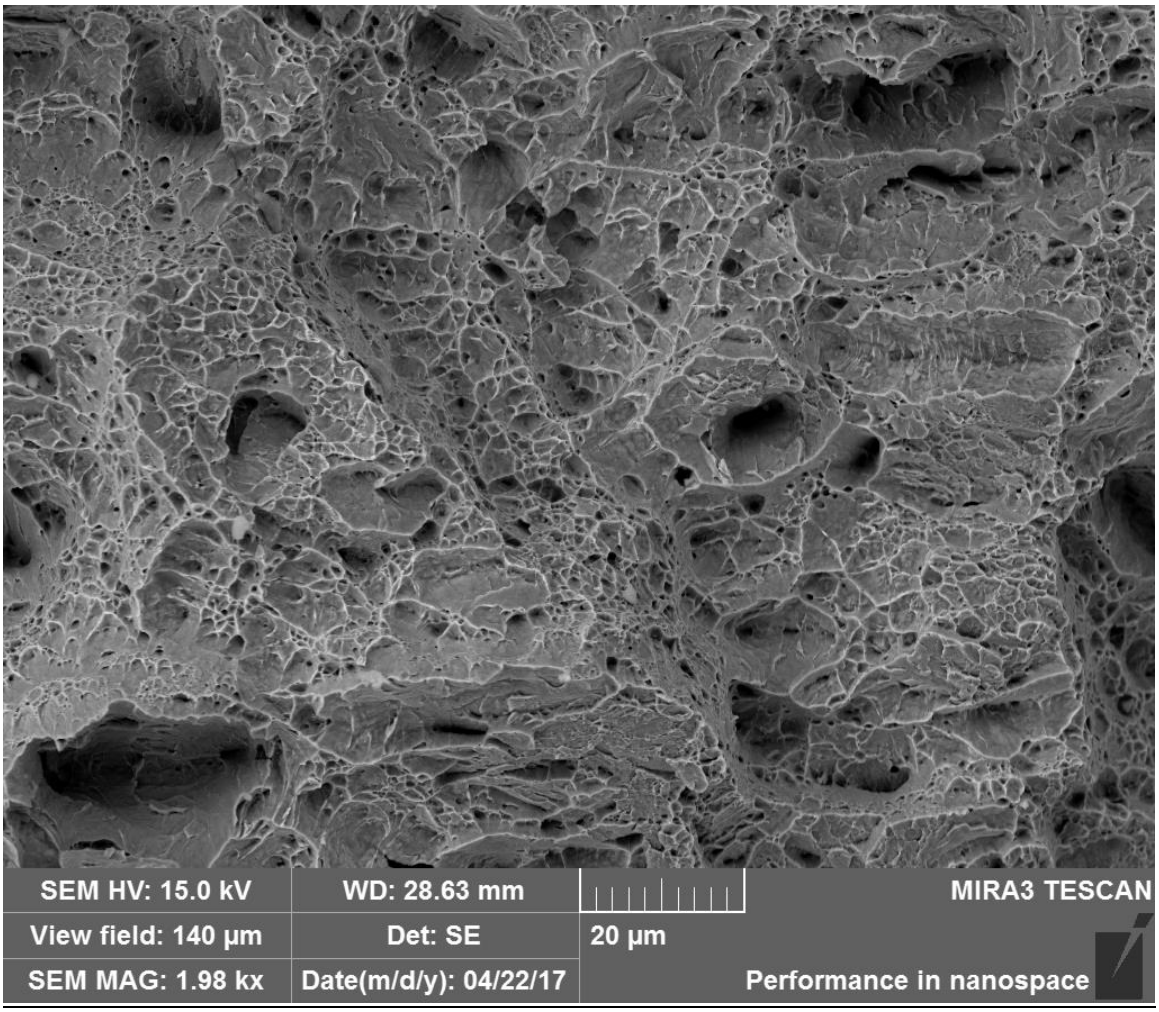

Figure 4.21: (c) continued

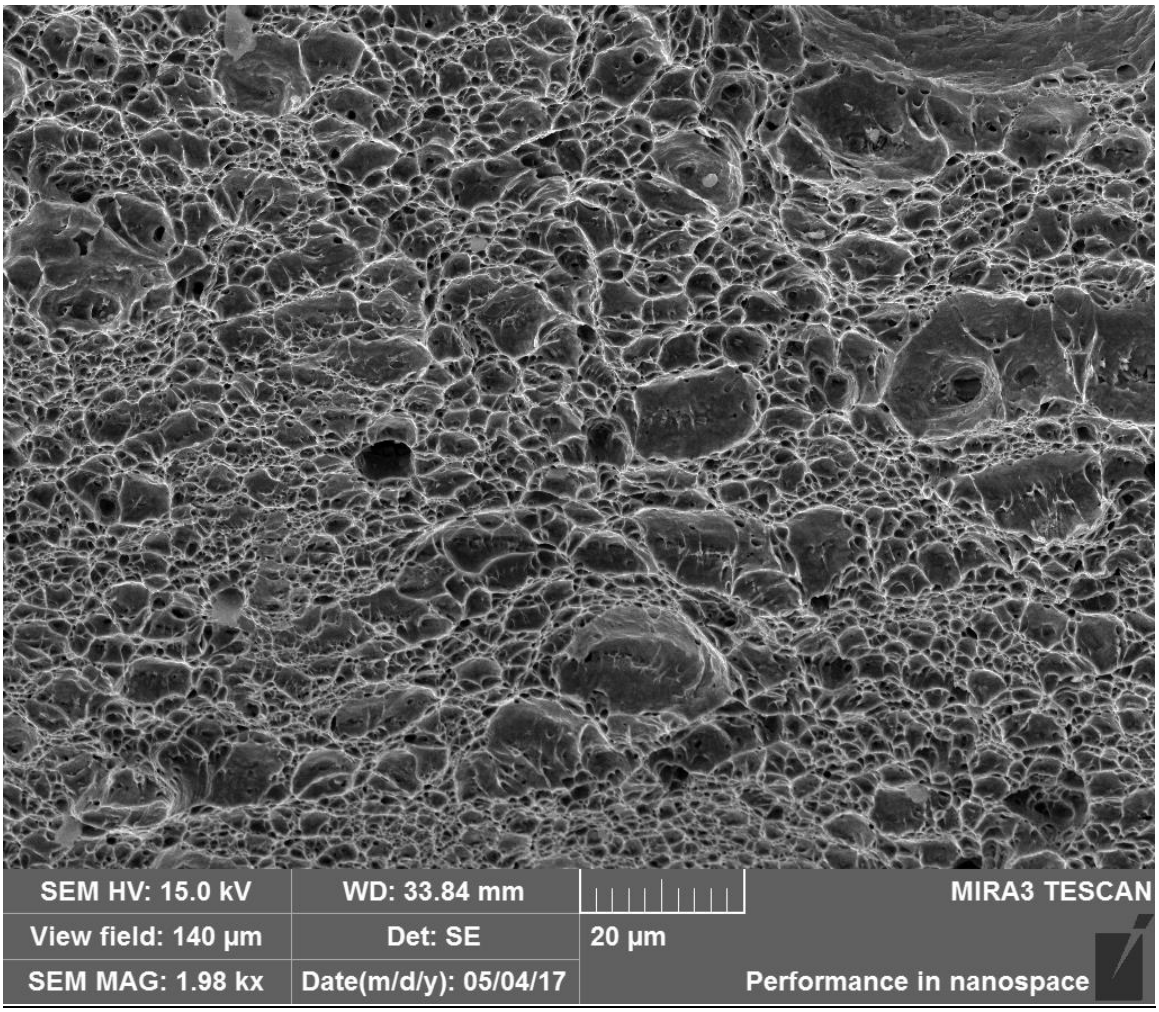

Figure 4.21: (d) continued

Table 4.7: Shows the area fraction of different fracture morphologies for (a) 920°C for 7 minutes and (b) 980°C for 30 minutes for USIBOR 1500.

(a)

Processing parameters	Strain rate (/sec)	$<A_A>$ dimple	error	$<A_A>$ brittle	error	$<A_A>$ Pullout	error
920°C, 7min	10^{-4}	0.74	0.07	0.25	0.07	0.03	0.03
	1000	0.73	0.06	0.26	0.06	0.01	0.01

(b)

Processing parameters	Strain Rate (/sec)	$<A_A>$ dimple	error	$<A_A>$ brittle	error	$<A_A>$ Pullout	error
980°C, 30min	10^{-4}	0.40	0.08	0.60	0.08	0.012	0.002
	1000	0.85	0.07	0.15	0.07	0.007	0.001

Table 4.8: Number densities of dimples and pullouts for (a) 920°C for 7 minutes, and (b) 980°C for 30 minutes for USIBOR 1500.

(a)

Processing parameters	Strain Rate (/sec)	$<N_A>$ dimple (/mm^3) x 10^3	error	$<N_A>$ pullout (/mm^3) x 10^3	error
920°C, 7min	10^{-4}	93	8	0.12	0.01
	1000	119	25	0.08	0.02

(b)

Processing parameters	Strain Rate (/sec)	$<N_A>$ dimple (/mm^3) x 10^3	error	$<N_A>$ pullout (/mm^3) x 10^3	error
980°C, 30min	10^{-4}	112	33	0.034	0.006
	1000	147	36	0.029	0.005

Table 4.9: Average dimple size estimates for USIBOR 1500

Processing parameters	Strain rate (/sec)	Average Dimple Size (μm)
920°C, 7 minutes	10^{-4}	3.4 ± 0.2
	10^3	2.9 ± 0.3
980°C, 30 minutes	10^{-4}	3.7 ± 0.2
	10^3	3.3 ± 0.2

4.4 Coating Analysis

Figure 4.22 shows the coating on “as received” steels and EDS analysis on different layers.

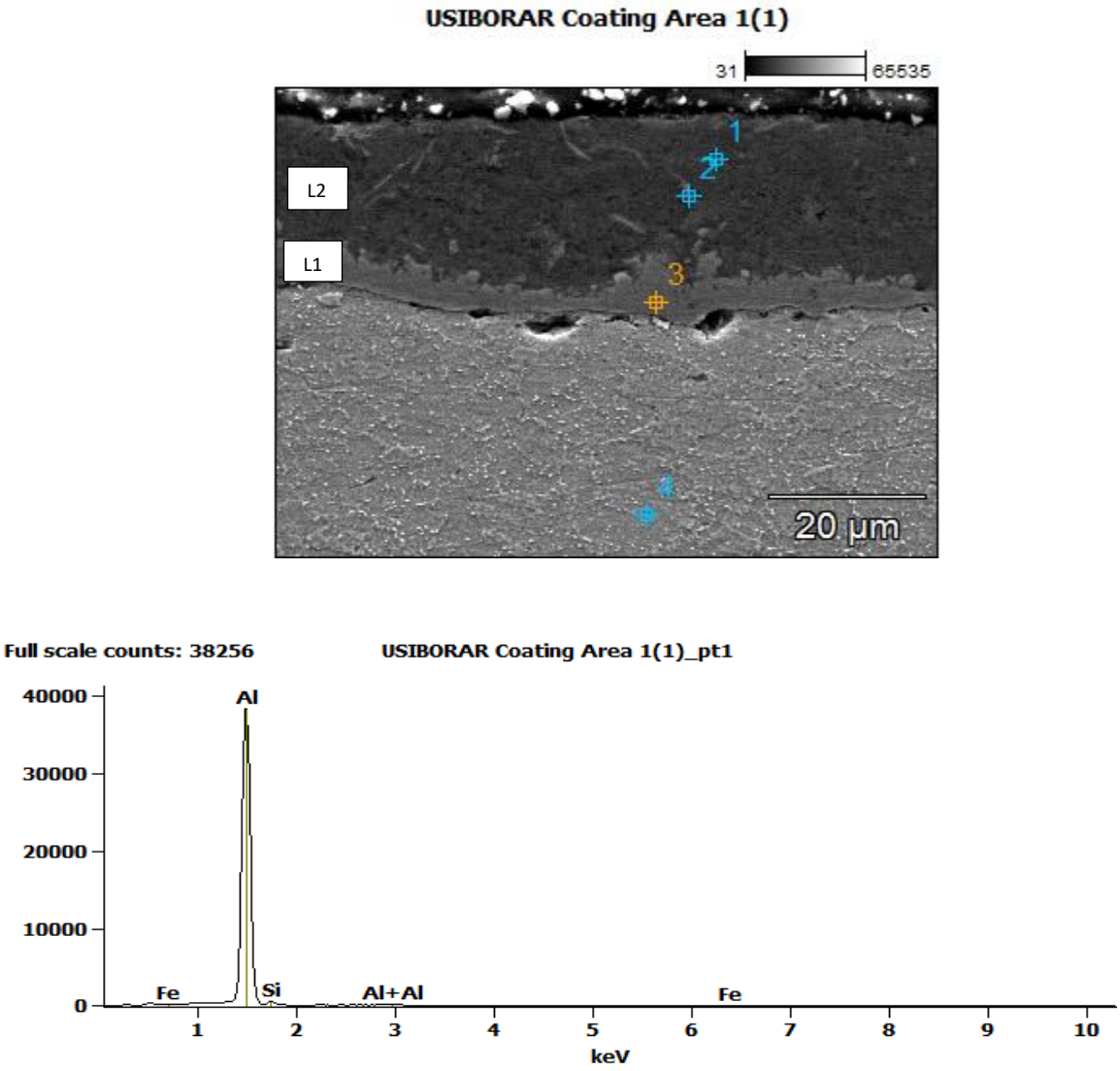

Figure 4.22: Shows the coating on as received steel grades and their EDS plots.

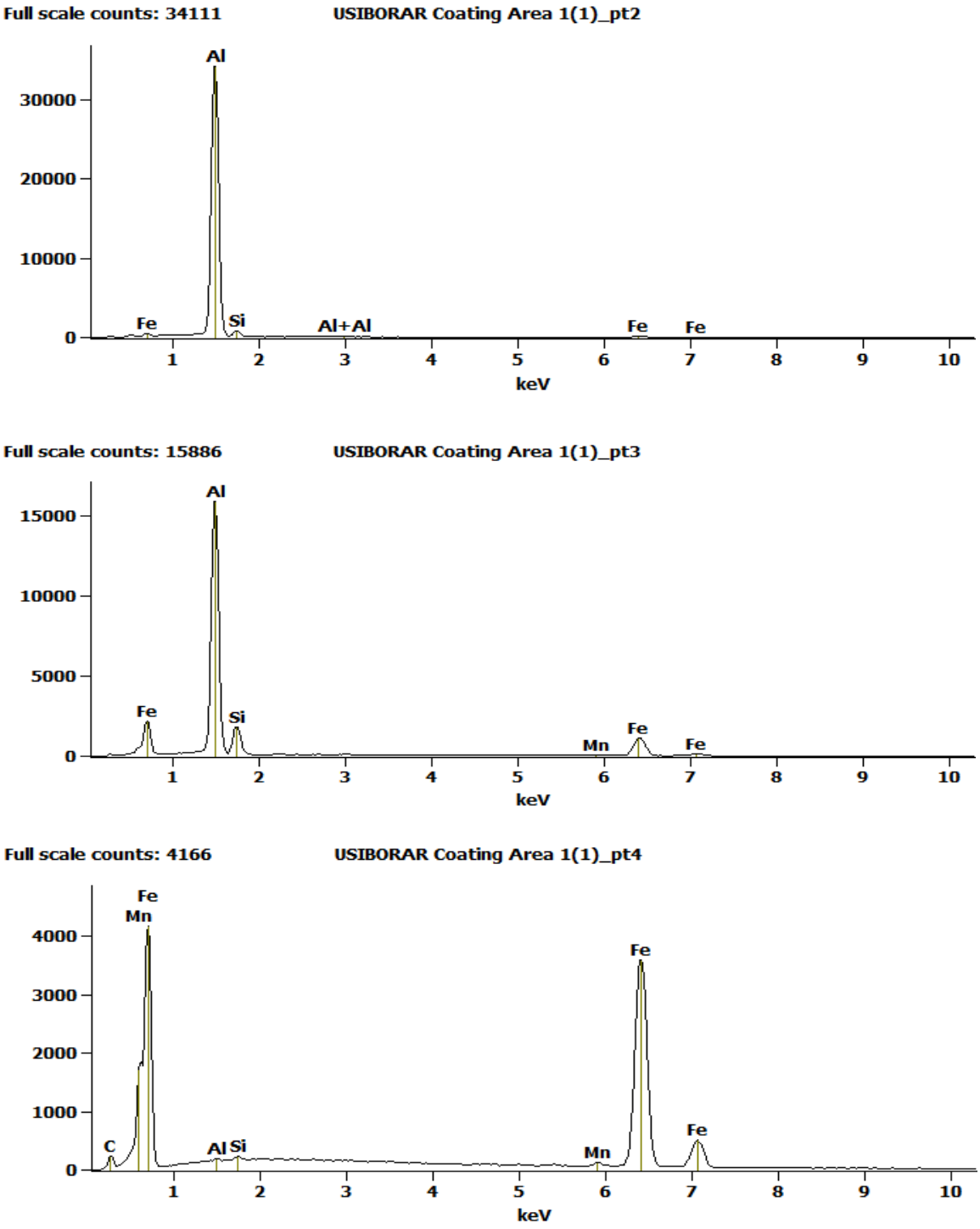

Figure 4.22: continued

As received coating consists of two different layers. The layer adjacent to the substrate (denoted by L1) is an intermetallic layer of Fe-Al-Si, which helps in stopping vertical cracks from reaching the substrate. Layer L2 is rich in Aluminum and contains about 10 weight percent Silicon. The average thickness of intermetallic layer was measured to be 4.33µm. Average thick of Layer L2 was measured to be 14.74µm. Figure 4.23 shows the coating layer after hot-forming at 920°C for 7 minutes, along with its EDS analysis. Total thickness of the coating was 19.3µm.

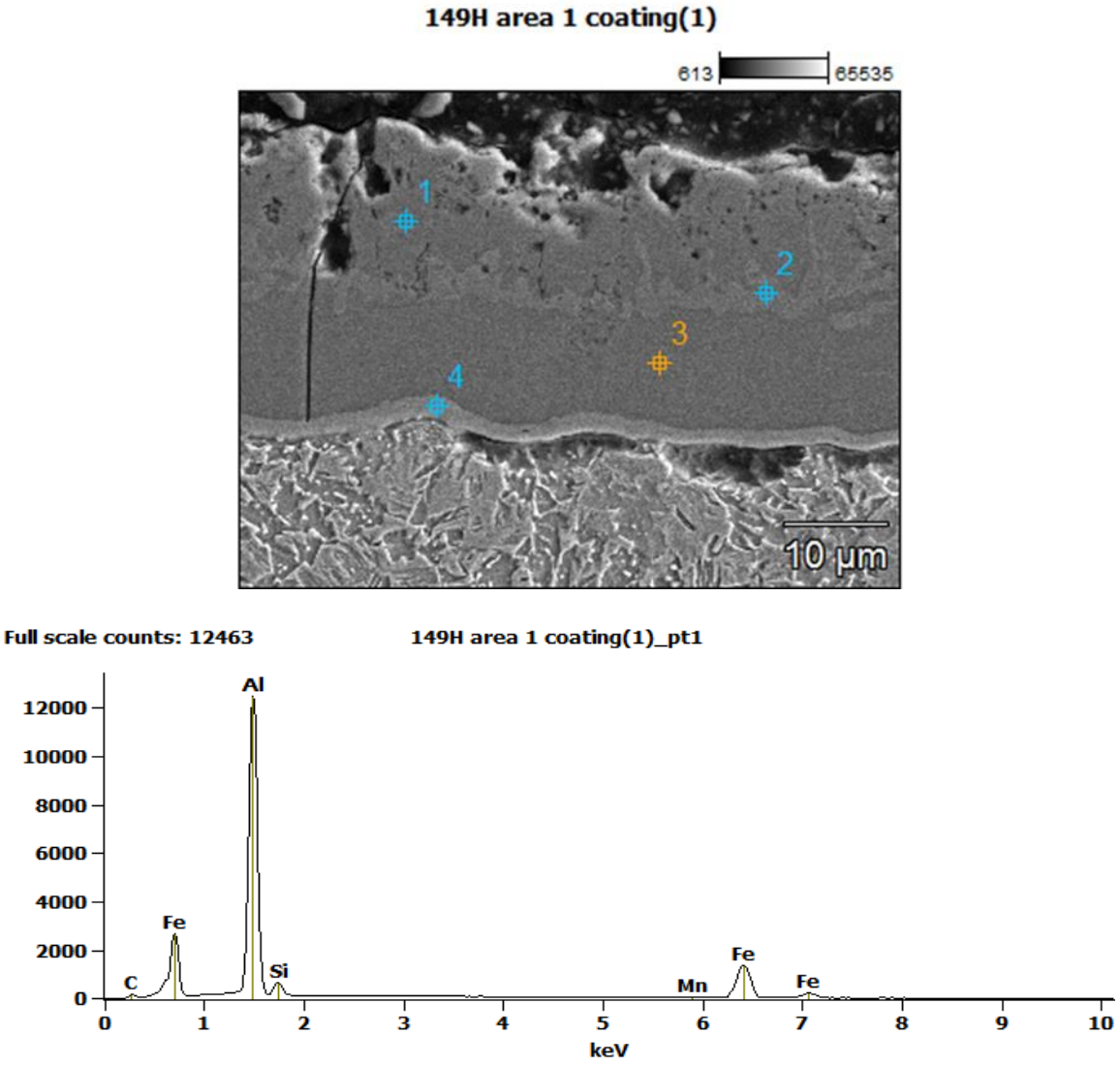

Figure 4.23: Shows the coating with EDS analysis at 920°C for 7 minutes.

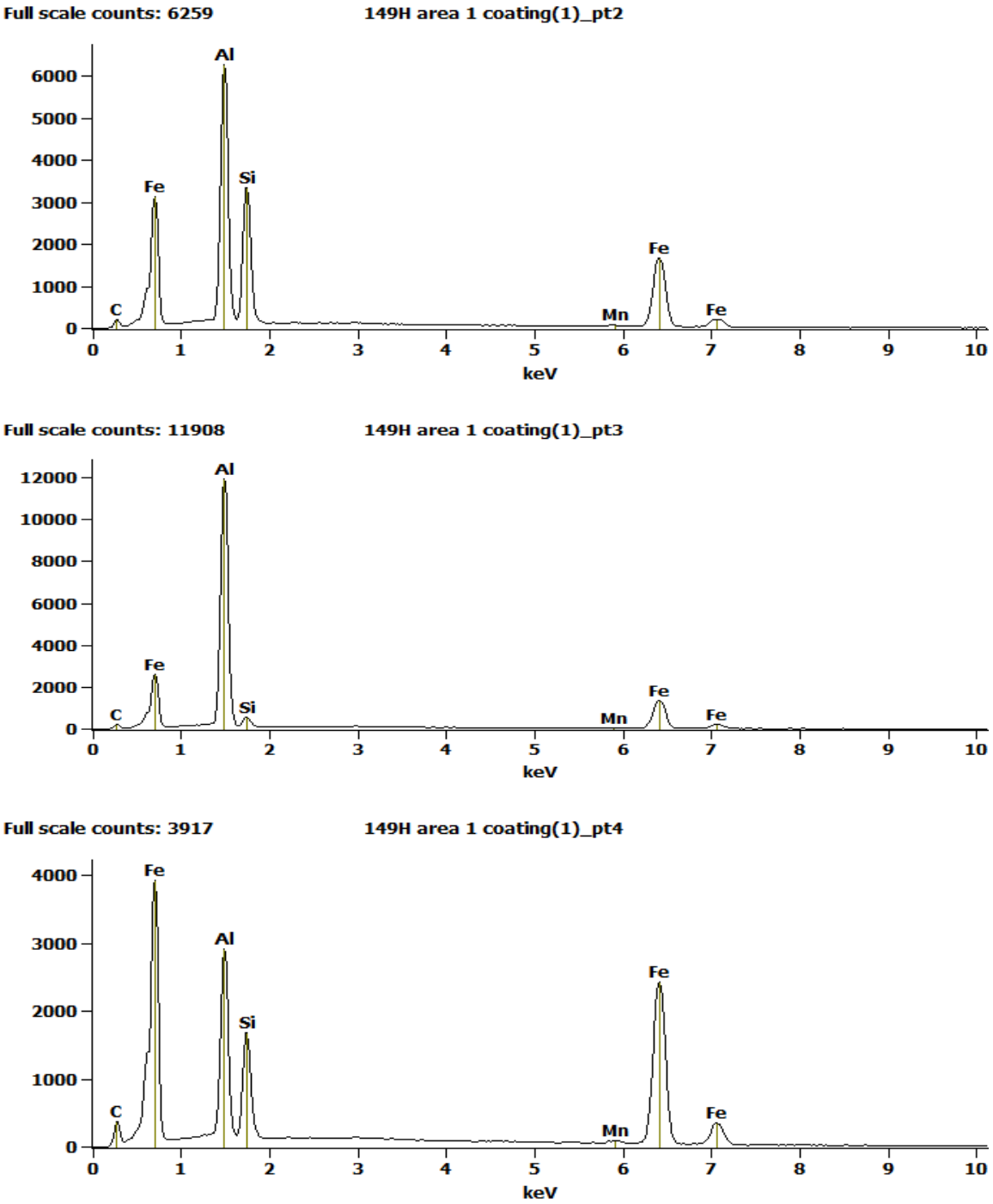

Figure 4.23: continued

Iron diffuses from the substrate during the hot-forming process. The average thickness of coating increased to 24µm. EDS analysis showed three different layers formed (point 1 and point 3 being the same). A layer rich in silicon was present in the coating. This layer, called the inter-diffusion layer was observed to be highly uneven. As seen in the micrograph, Fe-Al-Si inter-diffusion layer arrested the crack from propagating to the substrate. Figure 4.24 shows the coating after the blank was hot-formed at 950°C for 15 minutes.

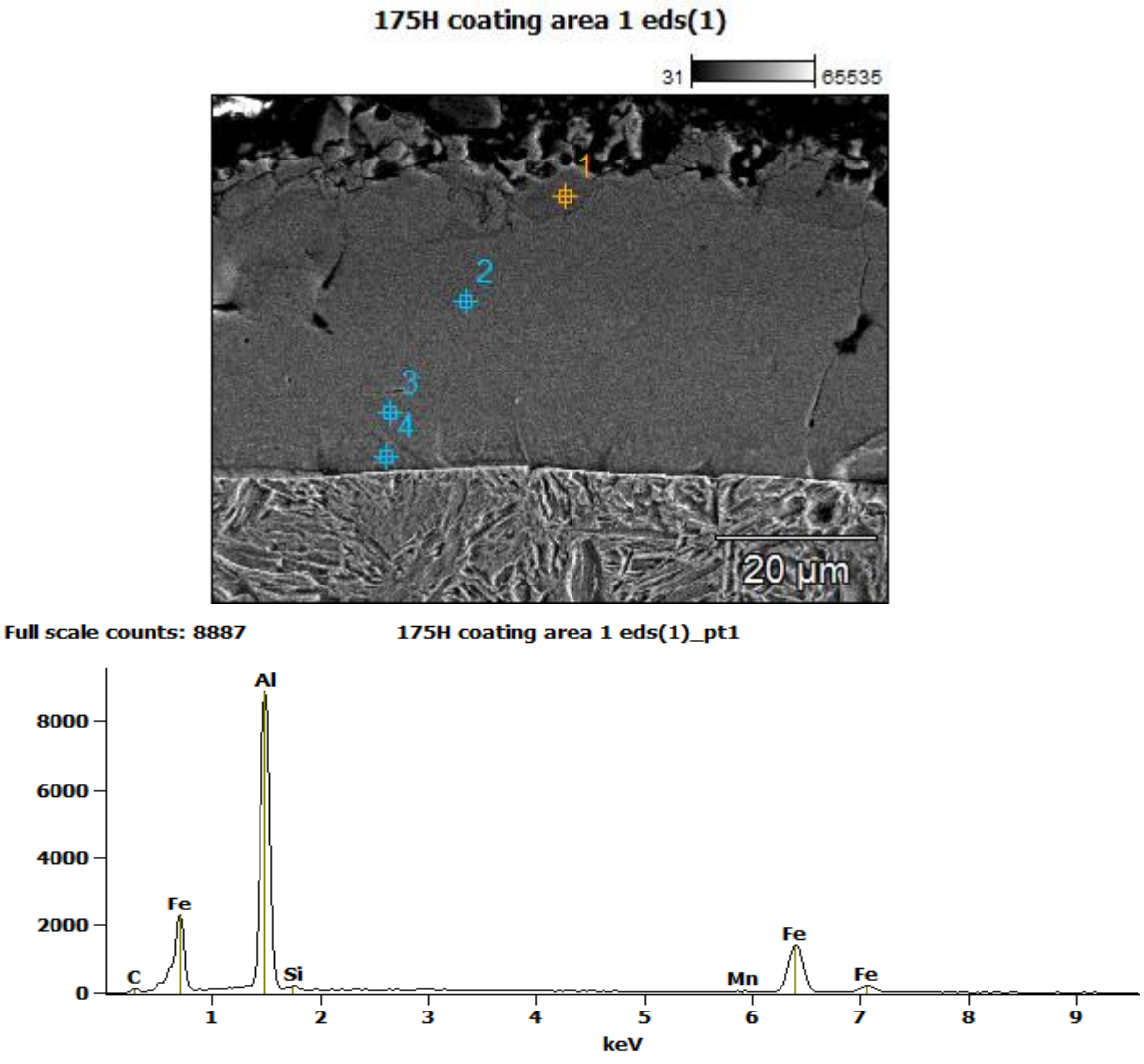

Figure 4.24: Shows the coating with EDS analysis for 950°C for 15 minutes.

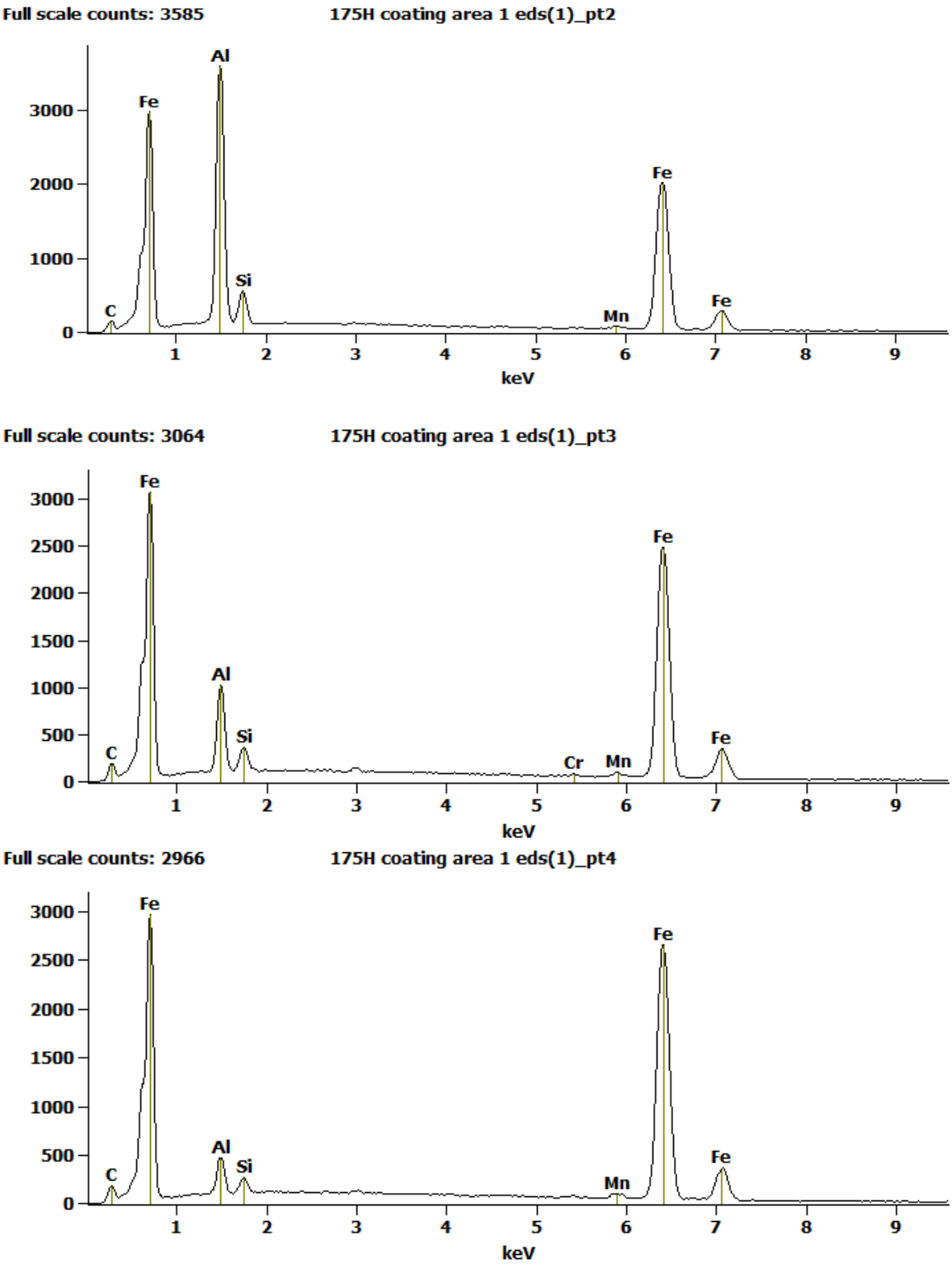

Figure 4.24: continued

At 950°C for 15 minutes, coating was observed to have 3 distinct layers. With more time for iron to diffuse in to the coating, the layer rich in Aluminum was seen to diminish with increasing temperature and time of austenitization. Average coating thickness at 950°C for 15 minutes was 39.6µm. Figure 4.25 shows the coating at 980°C for 30 minutes with EDS line scan.

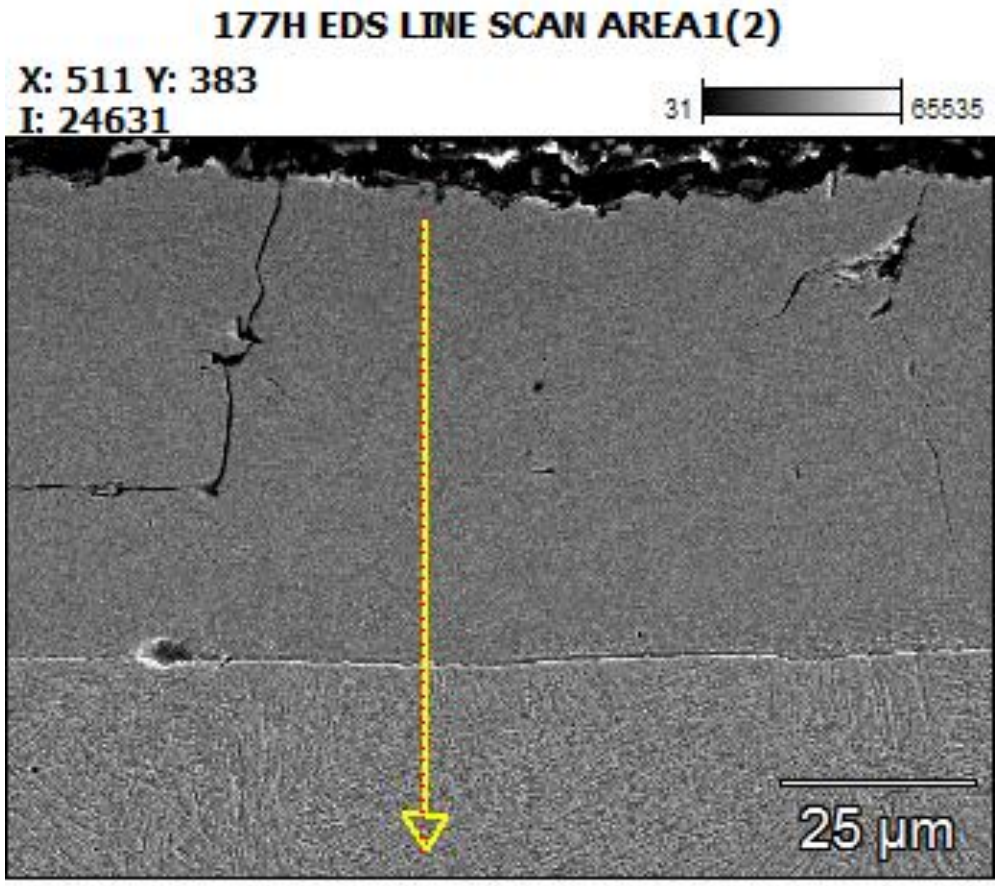

(a)

Figure 4.25: Shows the (a) coating with (b) EDS line scan at 980°C for 30 minutes.

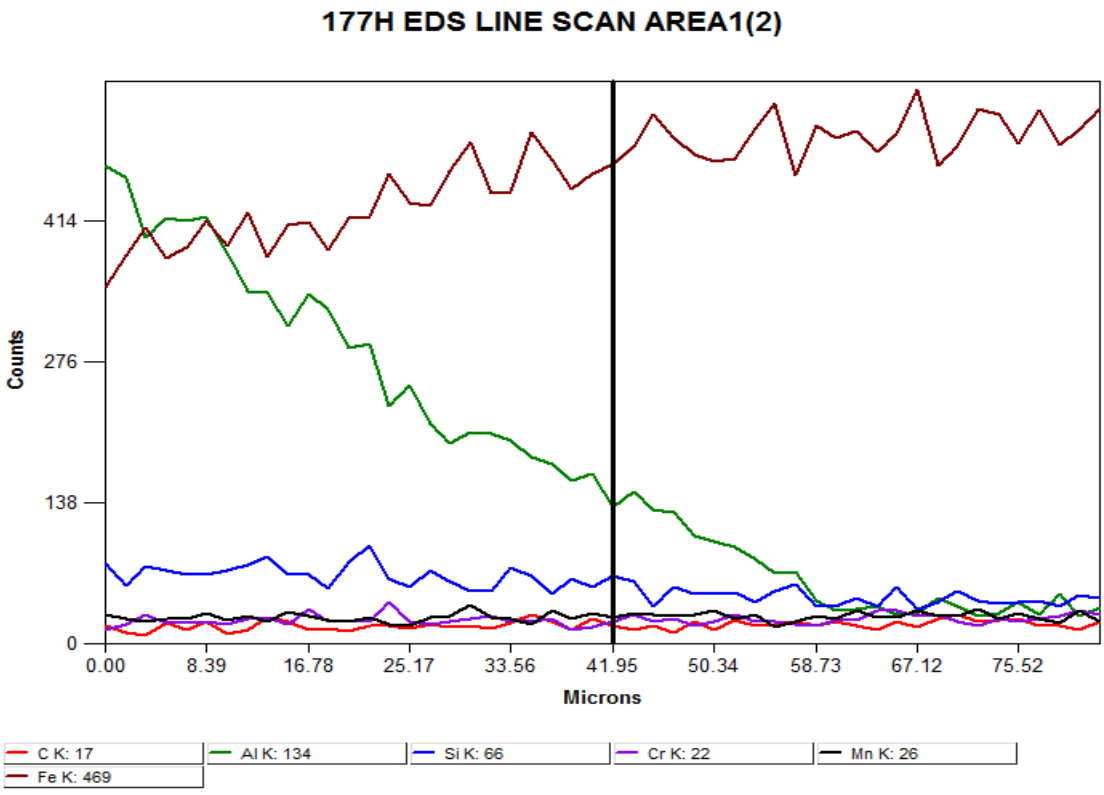

Figure 4.25: (b) continued

A single layer was observed at 980°C for 30 minutes. A line scan revealed gradual change in the concentrations of aluminum and iron. The average thickness of coating was observed to be 61.72µm.

Coating cross-section was also observed in failed specimens. Figure 4.26 shows the coating cross-section in failed specimens for the abuse condition, pulled at 1000/sec.

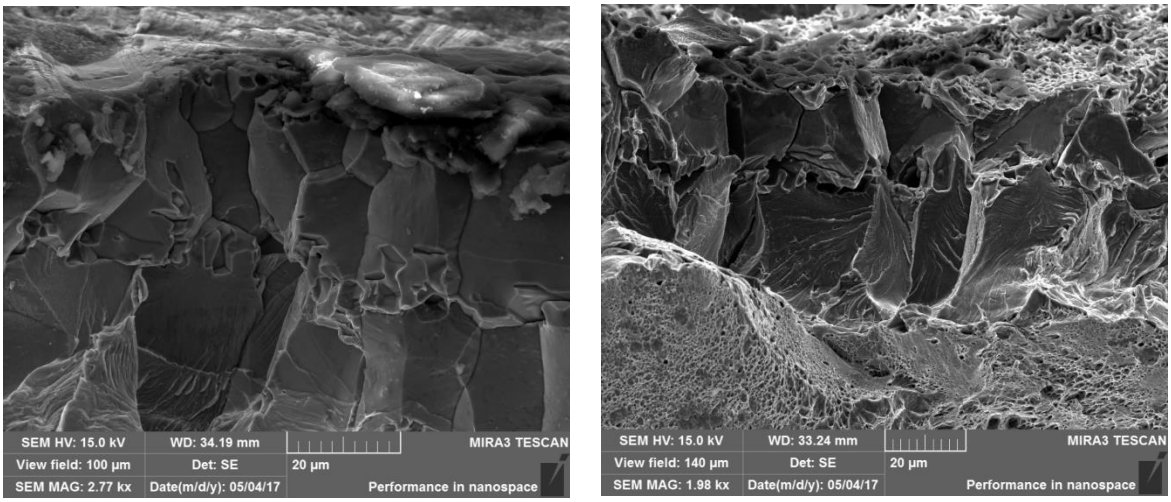

(a) (b)

Figure 4.26: Shows the coating cross-section in failed samples of (a) DUCTIBOR 500 and (b) USIBOR 1500 hot-formed at 980°C for 30 minutes and pulled at 1000/sec

Cross –section of both Ductibor 500 and Usibor 1500 hot-formed at 980°C for 30 minutes and deformed at 1000/sec, shows intergranular failure in the coating. Failure appears to be brittle in the coating, marked by the river pattern. Intergranular failure in coating was also observed for specimens pulled at slower strain rates and other heat-forming parameters. Coating adhered well near the fracture surface for process condition of 950°C for 15 minutes and 980°C for 30 minutes, even for specimens tested at 1000/sec. It did not adhere well to the substrate near the fracture surface for hot-forming process condition of 920°C for 7 minutes, as shown in figure 4.27.

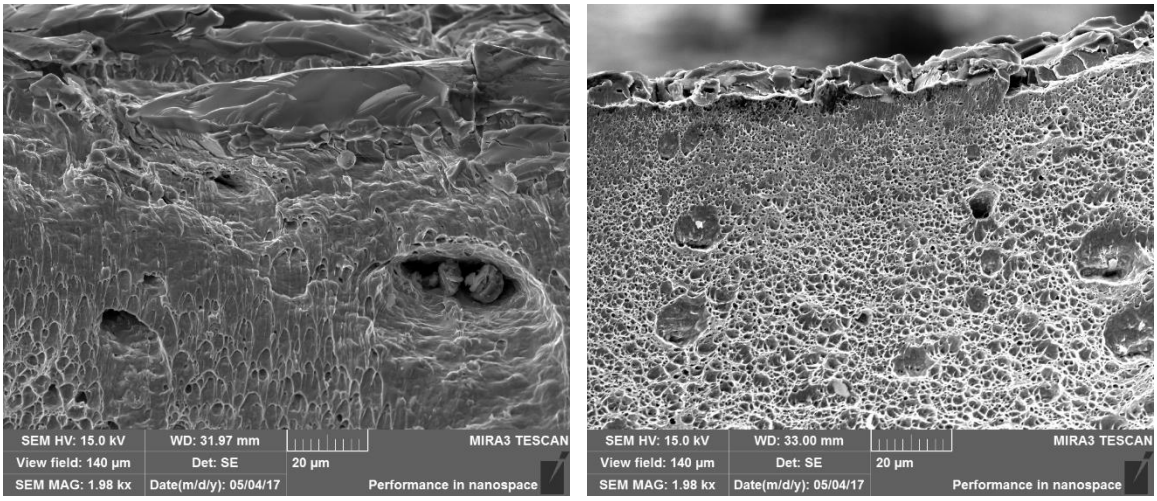

(a) (b)

Figure 4.27: Shows the coating for (a) DUCTIBOR 500, and (b) USIBOR 1500 hot-formed at 920°C for 7 minutes and pulled at 1000/sec.

4.4 DISCUSSION

Effects of strain rate and microstructure (with varying steel grades, and parameters of hot-forming), on the observed mechanical behavior and fracture micro-mechanisms have been discussed in this section. For simplicity, hot-forming process parameters have been referred as P1 for 920°C for 7 minutes, P2 for 950°C for 15 minutes, and P3 for 980°C for 30 minutes.

4.4.1 Effects of Geometry

Table 4.10 shows the "as received" tensile values for Ductibor 500 and Usibor 1500 for the miniature geometry used in this research, pulled at 10^{-4}/sec.

Table 4.10: Uni-axial tensile properties for "as received" DUCTIBOR 500 and USIBOR 1500 for the miniature geometry

Grade	UTS (MPa)	0.2% offset Yield Strength (MPa)	Uniform Elongation (%)	Total Elongation (%)
Ductibor 500	627	504.5	17.9	34
Usibor 1500	622	493	14.2	31

Values for ASTM E8 geometry for both Ductibor 500 and Usibor 1500 are listed in table 3.2. Measured ultimate tensile strengths, for both Ductibor 500 and Usibor 1500, were observed to be higher compared to the ASTM E8 geometry by approximately 50 MPa. Ductibor 500 had comparable yield strength values, whereas, Usibor 1500 showed an increase in yield strength value by 40 MPa in the miniature geometry. These variations could have arisen due to the variation in data acquisition and testing machine itself. From applications perspective, the differences in these values were well within the tolerance range. Ductility (or Total Elongation) is known to be dependent on the specimen geometry. Even though the uniform elongation values were comparable for both the geometries, miniature geometry showed considerably higher ductility for both Ductibor 500 and Usibor 1500. Therefore, deformation post uniform strain was much higher in miniature specimens.

4.4.2 Effects of Strain rate

1) HSLA 590

HSLA 590 has a completely ferritic microstructure. When the strain rate was increased from 10^{-4}/sec to 3200/sec, the ultimate tensile strength increased from 660 MPa to 1390 MPa (~110% increase), while the ductility increased by 10%. Yield strength increased changes from 500 MPa to 900 MPa (~80% increase) when the strain rate was increased from 10^{-4}/sec to 50/sec. Bilinear relationship was observed in the plots of UTS and YS versus logarithmic values of strain rate. The change in slope was observed at 1/sec. Bilinear relationship between flow stress at 0.1 plastic strain and logarithmic values of strain rate was observed by Alkhader et. al [45]. In this study, change in slope was observed at 1000/sec strain rate. Strain hardening coefficient (n) was calculated from the true stress – true strain plots. Strain hardening coefficient remained invariable at 0.08 for strain rates up to 10/sec. It increased to 0.57 for 80/sec.

Fracture profilometry revealed an increase in the profile roughness parameter (R_L) values from 1.79 to 2.91, an increase of about 62%, when the strain rates were changed from 10^{-4}/sec to 3200/sec. Therefore, fracture preferred a more tortuous path at a higher strain rate. Quantitative fractography showed that the failure at all strain rates was predominantly ductile, with little variations in area fractions of ductile and brittle regions with the strain rates. Moreover, number density of dimples remained invariant for all strain rates. Dimples are formed due to void formation, void coalescence and growth. These voids are formed at ferrite-ferrite grain boundaries, ferrite-ferrite-ferrite triple points or at the interface of ferrite and carbides, due to stress concentration [46]. Therefore, mechanisms

of void formation in HSLA 590 are independent of strain rate, as suggested by the nominal change in the number density and dimples size estimates. A higher ductility at 3200/sec, therefore, may only be dependent on the path of the fracture, as revealed by differences in profilometry.

2) Ductibor 500

For all hot-forming process parameters, when the strain rate was increased from 10^{-4} /sec to 1000/sec, the ultimate tensile strength increased by 50%. Yield strength showed an increase by almost 80%, whereas the ductility increased by 10%. As in the case of HSLA 590, ambiguity exists in the calculation of UTS and yield strength at 1000/sec. This is a characteristic of Hopkinson bar experiment. Peak observed in the engineering stress versus engineering strain curves may not correspond to the uniform strain. This ambiguity may be resolved by taking a series of timed images of the Hopkinson bar experiment, and correlating of these images to the obtained load. In case the specimen does not start to neck at the peak load, load corresponding to necking should be used to calculate the UTS. For hot-forming process parameters P2 and P3, microstructures obtained for Ductibor 500 after hot-stamping was very similar to that of dual phase steels. Figure 4.28 shows the variation in strain hardening coefficient (n) for Ductibor 500, with strain rate and hot-forming process conditions. Strain hardening coefficient for hot-forming process condition of P3 was slightly lower than conditions P1 and P2. The difference increased at 1000/sec. A lower value of strain hardening coefficient for hot-forming process condition P3 can be attributed to a comparatively large volume fraction of secondary hard constituents.

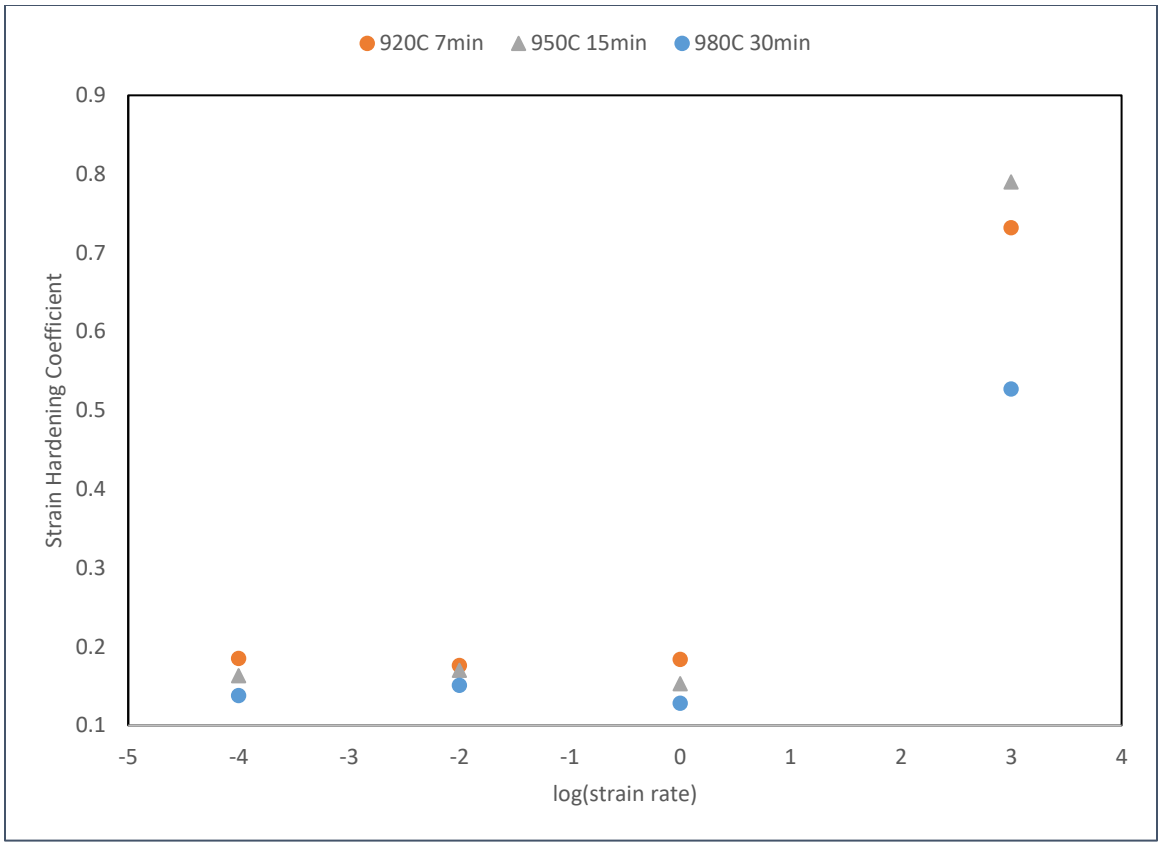

Figure 4.28: Strain hardening coefficient for DUCTIBOR 500.

Failure for all hot-forming process parameters were pre-dominantly ductile, at quasi-static as well as high strain rates. Area fractions of dimpled and brittle region remained invariant with the strain rate. Therefore, fraction of fracture surface undergoing ductile failure did not change with the strain rate. However, for hot-forming process parameter P1, number density of dimples decreased by half, whereas for P3, number density of dimples almost doubled for an increase in strain rate from 10^{-4}/sec to 1000/sec. Several previous studies have shown that in Dual Phase steels, ferrite – martensite debonding, fracture of martensite and localized deformation in martensite [47, 48] results in void formation. These voids grow and coalesce, ultimately forming dimples on the fracture surfaces. Variation in the number density of dimples could be because of the changes in void formation

mechanism with the volume fraction and morphology of hard-constituents in the microstructure, as well as the strain rate. Changes in area fraction and number density of dimples highlights the effect of microstructure and strain rate on micro-mechanisms of failure in Ductibor 500.

3) Usibor 1500

Usibor 1500 showed tensile strengths in excess of 1500 MPa. Ductility was observed to be in excess of 10%. For all process parameters, with an increase in the strain rate from 10^{-4}/sec to 1000/sec, the ultimate tensile strength increased by 20%, yield strength increased by about 50%, and ductility increased by approximately 4%. An increase in ductility was as a result of higher localized deformation in martensite at a higher strain rate. As discussed in the case of Ductibor 500, the ambiguity in calculating the UTS and yield strength at 1000/sec strain rate may be resolved by taking timed images of the Hopkinson bar experiment.

Quantitative fractography revealed a pre-dominantly ductile failure for all hot-forming process conditions. Area fraction of dimpled and brittle region remained invariant for hot-forming process parameter P1. However, for hot-forming process parameter P3, the area fraction of the dimpled region almost doubled at 1000/sec. Therefore, even at an abuse hot-forming condition, hot-stamped martensitic steel undergoes ductile failure at high strain rates, ductility being almost 18%. This can be of importance while designing automotive body parts that require high strength and high ductility. For hot-forming process parameter P1 and P3, the number density of dimples remained invariant with the change in strain rate.

4.4.3 Effects of microstructure

HSLA 590 has a completely ferritic microstructure. For process parameter P1, the engineering stress versus engineering strain curve shows yield point elongation phenomena, similar to the "as received" specimens. This suggests that complete austenitization could not be achieved for Ductibor 500 for hot-forming process parameter P1, and some pearlite still remained in the microstructure. Therefore, hot-forming process parameter P1 is insufficient to obtain dual phase type microstructure. For process parameters P2 and P3, the yield point elongation phenomena disappears, suggesting that these combinations of temperature and time are enough for complete austenitization. For process parameters P2 and P3, Ductibor 500 has a dual-phase type of microstructure with hard constituents like bainite and/or martensite in the ferrite matrix. The amount and morphology of bainite and/or martensite changes with the hot-forming process conditions. HSLA 590 and Ductibor 500 showed comparable strength values. These steel grades have comparable chemistries, therefore HSLA 590 can also be used for hot-stamping. However, even due to the differences in microstructure of HSLA 590 and hot-stamped Ductibor 500, they have similar strength values due to two competing factors; finer ferrite grains in HSLA 590, and larger ferrite grains with bainite and/or martensite. Usibor 1500 has a completely martensitic microstructure. Martensite laths growth thinner with increasing time and temperature of austenitization. This is as a result of larger austenite grain size, with increasing temperature and time of austenitization. Usibor 1500 being completely martensitic, showed much higher values of ultimate tensile strength and yield strengths. While comparing the different grades of steel, strength values and ductility for HSLA 590 showed the highest sensitivity to strain rate, while Usibor 1500 showed the least. It has

been well established that ferrite being the softer phase, deforms more than harder constituents like bainte and/or martensite. Fourlaris et.al [49] studied the strain rate behavior of three different grades of steels with varying martensitic content from 0% to 100%. It was observed that the tensile properties of the steel grade with highest martensitic content showed the least sensitivity to strain rate. For the same strain rate, relatively higher number of dislocations are produced in completely martensitic microstructure, which results in significantly higher initial strain hardening, compared to microstructures containing ferrite (softer phase), where movement of dislocations is much more easier. Dislocation intertwine, generating areas of high stress concentration, ultimately resulting in failure with lower ductility and much higher strength values in fully martensitic steels.

For hot-stamped steels, change in microstructures were observed with changing hot-forming process parameter. For a change in hot-forming process parameter from P1 to P3, for both quasi-static and high strain rates, Ductibor 500 showed a 10% increase in strength values. Ductility was observed to decrease by approximately 3%. This increase in strength values, and decrease in ductility, may be as a result of increase in the volume fraction and change in morphology of bainite and/or martensite (hard constituents) in the microstructure. For practical applications, the change in strength values is minimal, highlighting the robustness of hot-stamping process. Change in area fractions of dimpled region and number density of dimples were more prominent at 1000/sec, thereby suggesting that the fracture micro-mechanisms are more sensitive at high strain rates. As discussed earlier, ferrite – hard constituent interface de-cohesion is one of the mechanisms of void formation. Differences in strain partitioning between ferrite (softer phase) and martensite leads to the accumulation of dislocations at their interface. Ferrite being the

softer phase, it is more susceptible to deformation at high strain rates. A larger variation in fracture micro-mechanisms at high strain rates, may be as a result of higher strain partitioning between ferrite and hard constituents at high strain rates.

For both quasi-static and high strain rates, Usibor 1500 showed a 4% decrease in the strength values and 3% increase in ductility when the process conditions were changed from P1 to P3. Usibor 1500 being completely martensitic, the variations in tensile properties were minimal for these processing conditions. These minimal variation in tensile properties of Usibor 1500, reaffirms the robustness of hot-stamping process over the range of hot-forming process conditions used in this research. Contrary to Ductibor 500, for a change in hot-forming process condition, it was observed that the area fraction of dimpled failure was more sensitive at 10^{-4}/sec compared to 1000/sec. This further highlights the effect microstructure and strain rate on failure micro-mechanisms.

4.4.3 Coating analysis

From the cross-sectional SEM analysis, coating showed different layers with varying concentrations of Al, Si and Fe. During the austenitization process, Fe from the substrate steel diffuses into the coating, thereby forming intermetallic coating layers. Majority of cracks were observed to be vertical, originating at the coating surface. These cracks got arrested at the Al-Fe-Si intermetallic layer, preventing the crack from reaching the substrate, and in turn inhibiting material failure. The thickness of the coating increased from about 24μm for hot- forming process condition P1 to about 64μm for condition P3 due to an increase in diffusion of Fe into the coating as revealed by the EDS analysis. Coating adhered well to the substrate near the fracture surface for hot-forming process

conditions P2 and P3. Absence of inter-diffusion layer rich in Si, may have resulted in better coating adherence for these hot-forming process parameters. Failure in the coating occurred through intergranular crack propagation.

CHAPTER 5

SUMMARY AND CONCLUSIONS

The main focus of this research is on understanding the effects of microstructure and strain rate on fracture micro-mechanisms in Advanced High Strength Sheet (AHSS) steels. To achieve this, three different commercially available grades of steel; HSLA 590, Ducitbor 500 and Usibor 1500 have been studied. Global microstructures of these steel grades have been quantified using stereological techniques. Tensile tests were conducted at different strain rates ranging from 10^{-4}/sec to 3200/sec. Additionally, differences in fracture surfaces have been studied using quantitative fractography and fracture profilometry. Following important observations and conclusions were made from the obtained data.

- Tensile properties of all three grades of steel are strain rate sensitive. HSLA 590 has the largest change in strength values and ductility, primarily due to the presence of softer ferrite phase.
- Hot-forming conditions used in this research are robust for both Ductibor 500 and Usibor 1500, as the variation in tensile properties is minimal for these conditions.
- Failure in both Ductibor 500 and Usibor 1500 is pre-dominantly ductile, even at an abuse hot-forming condition of 980°C for 30 minutes. Variation in number density of dimples, shows that the void nucleation density is a function of both strain rate and microstructure.
- Thickness of coating increases by almost 3 times when the processing condition is changed from nominal to abuse. Intergranular failure is observed in the coating.

Future Recommendations

Obtained data and their analyses from this research shows the strain rate dependency of tensile properties in ferritic HSLA 590, and hot-stamped Ductibor 500 and Usibor 1500. It would be interesting to quantitatively study the fracture profiles of these steel grades for void formation and extent of deformation in different phases as a function of distance from the fracture edge. This will provide additional insights in to the deformation behavior in these steel grades. Another important aspect would be to understand the better adherence of coating layer near the fracture edge, when the intermetallic layer is absent.

APPENDIX

1) STEREOLOGICAL MEASUREMENTS - MICROSTRUCTURES

a) Ductibor 500

920°C, 7min		950°C, 15min		980°C, 30 min	
Points on secondary phases	No. of intersections with the Cycloid	Points on secondary phases	No. of intersections with the Cycloid	Points on secondary phases	No. of intersections with the Cycloid
4	16	3	5	4	7
2	13	3	8	4	9
2	7	1	6	4	7
3	13	2	6	4	12
4	4	0	2	3	14
3	8	2	4	2	6
3	7	2	5	3	7
2	16	4	6	4	7
4	9	0	10	5	13
5	6	4	11	3	10
2	8	3	4	0	9
1	8	3	10	4	9
2	10	3	6	3	11
2	9	5	9	4	16
4	7	1	2	4	6
2	10	3	8	4	14
2	6	2	10	5	12
3	4	3	6	3	12
2	10	1	7	2	8
3	11	6	11	4	12
4	5	4	10	3	8

Points on secondary phases correspond to the number of points lying on the secondary phases on a 3x3 point grid in point counting method.

Raw data for total surface per unit volume with the number of intersections of cycloids with the ferrite – secondary phase interface, length of the minor axis of cycloid being equal to 23.35μm.

b) Usibor 1500

920°C, 7min	950°C 15min	980°C, 30 min
No. of Intersections with the Cycloid	No. of Intersections with the Cycloid	No. of Intersections with the Cycloid
13	15	20
8	16	13
14	18	31
19	18	26
14	21	19
17	25	28
16	24	18
17	16	26
23	32	26
8	22	35
15	24	12
13	28	15
18	34	26
17	28	32
14	33	33
18	29	37
8	21	32
18	25	25
14	20	27

Raw data for total surface area per unit volume with the number of intersection of cycloid with the martensite – martensite inteface with the length of the cycloid being equal to 23.35μm.

2) TENSILE DATA TABLE FOR HSLA 590

Strain Rate	log strain rate	UTS (MPa)	Ductility (%)	0.2% offset YS (MPa)	Uniform Strain (%)
1.00E-04	-4	659.62	41.05	500	8.97
0.01	-2	704.47	41.23	550	12.04
0.1	-1	676.56	43.35	580	8.06
1	0	697.04	47.09	600	10.07
10	1	718.25	49.66	620	9.36
80	1.90309	1001.47	47.35	900	2.13
3000	3.477121	1391	50.32	-	1.07
3200	3.50515	1164	52	-	0.8

3) TENSILE DATA FOR DUCTIBOR 500

a) "As received" DUCTIBOR 500

Strain rate (/sec)	0.2% offset YS (MPa)	UTS (MPa)	Ductility (%)	Strain Hardening Coefficient (n)
0.0001	504	627	34	0.15
0.01	518	654	34	0.16
1	549	668	34	0.15
1000	-	-	-	-

* 1000/sec tests were not conducted

b) HOT – FORMING CONDITION : 920°C, 7 MINUTES, DUCTIBOR 500

Strain rate (/sec)	0.2% offset YS (MPa)	UTS (MPa)	Ductility (%)	Strain Hardening Coefficient (n)
0.0001	442	627	31	0.18
0.01	439	652	33	0.18
1	472	659	33	0.18
1000	790	915	44	0.73

c) HOT – FORMING CONDITION: 950°C, 15 MINUTES, DUCTIBOR 500

Strain rate (/sec)	0.2% offset YS (MPa)	UTS (MPa)	Ductility (%)	Strain Hardening Coefficient (n)
0.0001	427	638	33.2	0.16
0.01	411	640	36.4	0.17
1	452	658	31.6	0.15
1000	800	1048	44.2	0.79

d) HOT – FORMING CONDITION: 980°C, 30 MINUTES, DUCTIBOR 500

Strain rate (/sec)	0.2% offset YS (MPa)	UTS (MPa)	Ductility (%)	Strain Hardening Coefficient (n)
0.0001	439	694	27.3	0.14
0.01	409	695	29	0.15
1	466	738	25.6	0.13
1000	880	1010	41.7	0.53

4) TENSILE DATA FOR USIBOR 1500

a) "AS RECEIVED" USIBOR 1500

Strain rate (/sec)	0.2% offset YS (MPa)	UTS (MPa)	Ductility (%)
0.0001	493	622	31
0.01	497	637	32.4
1	537	685	30
1000	-	-	-

* 1000/sec tests were not conducted

b) HOT – FORMING CONDITION: 920°C, 7 MINUTES, USIBOR 1500

Strain rate (/sec)	0.2% offset YS (MPa)	UTS (MPa)	Ductility (%)
0.0001	1218	1607	10
0.01	1122	1582	13
1	1202	1592	10.5
1000	1820	1951	14.5

c) HOT –FORMING CONDITION: 950°C, 15 MINUTES, USIBOR 1500

Strain rate (/sec)	0.2% offset YS (MPa)	UTS (MPa)	Ductility (%)
0.0001	1081	1532	13.1
0.01	1094	1526	13.2
1	1105	1514	10
1000	1400	1926	15

d) HOT – FORMING CONDITION: 980°C, 30 MINUTES, USIBOR 1500

Strain rate (/sec)	0.2% offset YS (MPa)	UTS (MPa)	Ductility (%)
0.0001	1108	1538	13.3
0.01	1091	1488	13
1	1150	1492	17
1000	1911	1660	18

5) FRACTOGRAPHY DATA DUCTIBOR 500 (9X9 point frame for point counting, area of unbiased frame = 4234.24 μm^2 for number density counts)

a) 920°C, 7 minutes - 10^{-2}/sec

# of test points on dimpled region	# of dimples in the unbiased frame	# of test points on pullout region	# of pullouts in the unbiased frame	# of test points on faceted region
8	848	0	1	1
9	712	0	1	0
9	337	0	3	0
7	599	0	0	2
9	576	0	1	0
7	777	2	1	0
6	313	0	1	3
6	447	2	0	1
7	561	0	3	2
2	457	2	5	5
3	389	3	3	3
4	597	0	1	5
9	275	0	3	0
9	537	0	2	0
7		0		2
7		0		2
7		1		1
7		1		1
3		0		6
6		2		1
8		0		1
4		0		4
3		0		6
9		0		0

b) 920°C, 7 minutes - 1/sec

# of test points on dimpled region	# of dimples in the unbiased frame	# of test points on pullout region	# of pullouts in the unbiased frame	# of test points on faceted region
5	214	1	1	3
4	182	0	2	5
2	436	2	0	5
5	266	0	2	4
0	201	0	2	9
2	253	2	1	5
7	277	0	2	2
6	290	0	5	3
5	502	2	1	2
7	492	1	1	1
7	288	0	3	2
5	387	0	2	4
6	508	1	2	3
2	507	3	2	4
4		2		3
6		1		2
4		3		2
7		0		2
7		0		2
9		0		0
4		0		5
6		1		2
5		1		3
6		2		2
7		0		2
8		0		1

c) 980°C, 30 minutes – 10^{-4}/sec

# of test points on dimpled region	# of dimples in the unbiased frame	# of test points on pullout region	# of pullouts in the unbiased frame	# of test points on faceted region
6	148	3	2	3
6	395	2	0	3
9	316	0	1	0
7	229	1	2	2
5	335	4	2	4
7	362	0	0	2
9	303	0	2	0
8	355	1	0	1
6	286	3	0	3
8	302	1	1	1
9		0		0
7		2		2
9		0		0
0		2		9
4		2		5
9		0		0
7		0		2
9		0		0
9		0		0
9		0		0
6		1		3
7		2		2

d) 980°C, 30 minutes – 10^{-2}/sec

# of test points on dimpled region	# of dimples in the unbiased frame	# of test points on pullout region	# of pullouts in the unbiased frame	# of test points on faceted region
5	391	0	1	2
8	388	0	2	1
7	246	1	2	1
5	110	1	1	3
3	301	1	2	5
7	410	1	0	1
4	596	1	1	4
2	524	3	1	4
3	511	1	1	5
5	498	0	0	4
6		1		2
1		1		7
4		0		5
4		0		5
2		0		7
3		0		6
6		0		3
9		0		0
2		0		7
3		0		6
6		1		2
9		0		0
8		0		1
9		0		0
5		0		4
8		0		1

e) 980°C, 30 minutes – 1/sec

# of test points on dimpled region	# of dimples in the unbiased frame	# of test points on pullout region	# of pullouts in the unbiased frame	# of test points on faceted region
5	398	0	2	4
8	424	0	1	1
4	483	0	2	5
6	527	0	0	3
5	334	0	1	4
9	248	0	1	0
9	308	0	1	0
9	404	0	0	0
8	456	0	0	1
8	509	0	1	1
6		0		3
7		0		2
8		0		1
4		0		5
3		0		6
7		0		2
6		0		3
4		0		5
4		0		5
6		0		3
5		0		4
8		0		1
5		1		3
8		0		1
2		0		7
7		0		2

f) 980°C, 30 minutes – 1000/sec

# of test points on dimpled region	# of dimples in the unbiased frame	# of test points on pullout region	# of pullouts in the unbiased frame	# of test points on faceted region
9	864	0	0	0
8	633	0	0	1
5	579	0	2	4
9	863	0	0	0
8	827	0	1	1
9	479	0	1	0
9	412	0	3	0
9	670	0	1	0
9	834	0	0	0
9	562	0	2	0
6		1		3
8		0		1
8		0		1
5		2		4
8		0		1
8		0		1
7		0		2
5		1		4
9		0		0
9		0		0
9		0		0
5		0		4
4		1		5
6		0		3
4		2		5
8		0		1
8		0		1
9		0		0
9		0		0
9		0		0
6		0		3
7		0		2
6		0		3

6) FRACTOGRAPHY DATA USIBOR 1500 (9X9 point frame for point counting, area of unbiased frame = 4234.24 μm^2 for number density counts)

a) 920°C, 7 minutes - 10^{-2}/sec

# of test points on dimpled region	# of dimples in the unbiased frame	# of test points on pullout region	# of pullouts in the unbiased frame	# of test points on faceted region
8	631	0	1	1
4	883	4	1	1
9	913	0	1	0
6	1112	0	0	4
9	903	0	1	0
8	649	1	1	0
8	870	0	1	1
8	536	0	1	1
9	995	0	1	0
8	682	0	1	1
9		0		0
8		0		1
9		0		0
9		0		0
9		0		0
8		0		1
7		0		2
4		1		4
6		0		3
9		0		0
7		0		2
7		0		2
8		0		1
8		0		1

b) 920°C, 7 minutes – 1/sec

# of test points on dimpled region	# of dimples in the unbiased frame	# of test points on pullout region	# of pullouts in the unbiased frame	# of test points on faceted region
9	795	0	1	0
9	507	0	2	0
9	714	0	1	0
9	835	0	1	0
7	832	2	1	0
5	819	1	1	3
7	688	2	0	0
9	640	0	3	0
8	826	1	0	0
7	801	0	1	2
9		0		0
8		0		1
8		0		1
9		0		0
9		0		0
9		0		0
8		0		1
9		0		0
8		1		0
6		0		3
9		0		0
7		1		1
9		0		0
9		0		0
8		0		1
7		0		2

c) 980°C, 30 minutes – 10^{-4}/sec

# of test points on dimpled region	# of dimples in the unbiased frame	# of test points on pullout region	# of pullouts in the unbiased frame	# of test points on faceted region
1	114	0	1	8
2	133	0	0	7
2	173	0	0	7
1	264	0	0	8
2	183	1	0	7
2	114	0	0	7
3	321	0	0	6
5	243	0	1	4
7	175	0	2	2
6	208	0	0	3
7		0		2
3		0		6
1		0		8
1		0		8
6		0		3
3		0		6
5		0		4
3		0		6
2		0		7
4		0		5
4		0		5
6		0		3
3		0		6
8		0		1
5		2		4
3		0		6

d) 980°C, 30 minutes – 10^{-2}/sec

# of test points on dimpled region	# of dimples in the unbiased frame	# of test points on pullout region	# of pullouts in the unbiased frame	# of test points on faceted region
4	194	0	0	5
3	434	0	0	6
1	356	0	0	8
4	272	0	0	5
3	455	0	1	6
2	674	2	0	5
5	315	0	0	4
6	241	0	2	3
7	270	0	0	2
9	264	0	0	0
8		0		1
8		0		1
4		2		3
6		0		3
7		0		2
8		0		1
7		0		2
6		0		3
3		0		6
4		0		5
5		0		4
4		0		5
4		0		5
9		0		0
4		1		4
7		0		2
5		0		4
0		0		9
9		0		0
3		0		6

e) 980°C, 30 minutes – 1/sec

# of test points on dimpled region	# of dimples in the unbiased frame	# of test points on pullout region	# of pullouts in the unbiased frame	# of test points on faceted region
7	273	1	1	1
7	371	0	3	2
2	383	2	1	5
0	556	1	0	8
1	498	0	2	8
5	502	2	1	2
5	863	0	0	4
5	467	0	3	4
2	385	1	3	6
3	620	0	1	6
3		0		6
6		0		3
6		0		3
8		1		0
6		0		3
6		0		3
6		0		3
5		0		4
9		0		0
7		0		2
8		0		1
8		1		0
8		0		1
3		1		5
8		0		1
7		0		2
8		0		1
6		0		3
7		1		1
8		0		1

f) 980°C, 30 minutes – 1000/sec

# of test points on dimpled region	# of dimples in the unbiased frame	# of test points on pullout region	# of pullouts in the unbiased frame	# of test points on faceted region
5	364	0	0	4
4	308	0	0	5
7	863	0	0	2
7	996	1	0	2
9	730	0	1	0
8	502	0	0	1
9	589	0	0	0
8	578	0	0	1
8	511	0	0	1
9	339	0	0	0
8		1		1
9		0		0
9		0		0
9		0		0
6		0		3
9		0		0
8		0		1
9		0		0
9		0		0
9		0		0
8		0		1
9		0		0
9		0		0
9		0		0
7		0		2
8		0		1

7) FRACTOGRAPHY TABLES

a) Ductibor 500

Temp - Time	Strain rate(/sec)	$<A_A>$ dimple	Error	$<A_A>$ brittle	Error	$<A_A>$ pullout	error
920°C, 7min	10^{-4}	0.66	0.09	0.34	0.09	0.21	0.08
	10^{-2}	0.73	0.08	0.27	0.10	0.06	0.03
	1	0.60	0.08	0.40	0.11	0.11	0.04
	1000	0.56	0.08	0.43	0.09	0.12	0.06

Temp -Time	Strain rate(/sec)	$<A_A>$ dimple	Error	$<A_A>$ brittle	Error	$<A_A>$ pullout	error
980°C, 30min	10^{-4}	0.79	0.01	0.21	0.09	0.12	0.05
	10^{-2}	0.59	0.09	0.41	0.11	0.05	0.02
	1	0.70	0.06	0.30	0.07	0.003	0.006
	1000	0.83	0.06	0.17	0.06	0.02	0.002

Time – Temp combination	Strain Rate(/sec)	$<N_A>$ dimples X 10^3 (/mm^3)	error	$<N_A>$ pullout x 10^3 (/mm^3)	error
920°C, 7min	10^{-4}	81	15	0.35	0.15
	10^{-2}	125	20	0.42	0.17
	1	81	14	0.43	0.14
	1000	40	11	0.59	0.23

Time-Temp combination	Strain Rate(/sec)	$<N_A>$ dimples X 10^3 ($/mm^3$)	error	$<N_A>$ pullout x 10^3 ($/mm^3$)	error
980°C, 30min	10^{-4}	71	16	0.27	0.17
	10^{-2}	87	23	0.30	0.11
	1	92	14	0.27	0.10
	1000	153	27	0.20	0.02

b) Usibor 1500

Processing parameters	Strain rate (/sec)	$<A_A>$ dimple	error	$<A_A>$ brittle	error	$<A_A>$ Pullout	error
920°C, 7min	10^{-4}	0.74	0.07	0.25	0.07	0.03	0.03
	10^{-2}	0.81	0.07	0.19	0.09	0.02	0.02
	1	0.89	0.05	0.11	0.06	0.04	0.02
	1000	0.73	0.06	0.26	0.06	0.01	0.01

Processing parameters	Strain Rate (/sec)	$<A_A>$ dimple	error	$<A_A>$ brittle	error	$<A_A>$ Pullout	error
980°C, 30min	10^{-4}	0.40	0.08	0.60	0.08	0.012	0.002
	10^{-2}	0.57	0.09	0.43	0.11	0.02	0.02
	1	0.63	0.09	0.37	0.10	0.04	0.02
	1000	0.85	0.07	0.15	0.07	0.007	0.001

Processing parameters	Strain Rate (/sec)	$<N_A>$ dimple (/mm^3) x 10^3	error	$<N_A>$ pullout (/mm^3) x 10^3	error
920°C, 7min	10^{-4}	93	8	0.12	0.01
	10^{-2}	192	29	0.20	0.05
	1	172	18	0.30	0.13
	1000	119	25	0.08	0.02

Processing parameters	Strain Rate (/sec)	$<N_A>$ dimple (/mm^3) x 10^3	error	$<N_A>$ pullout (/mm^3) x 10^3	error
980°C, 30min	10^{-4}	112	33	0.034	0.006
	10^{-2}	151	40	0.085	0.11
	1	182	43	0.32	0.20
	1000	147	36	0.029	0.005

Note: Data for 10^{-2}/sec and 1/sec for Ductibor 500 and Usibor 1500 were calculated after the thesis defense.

8) USIBOR 1500 - PRIOR AUSTENITE GRAIN SIZES

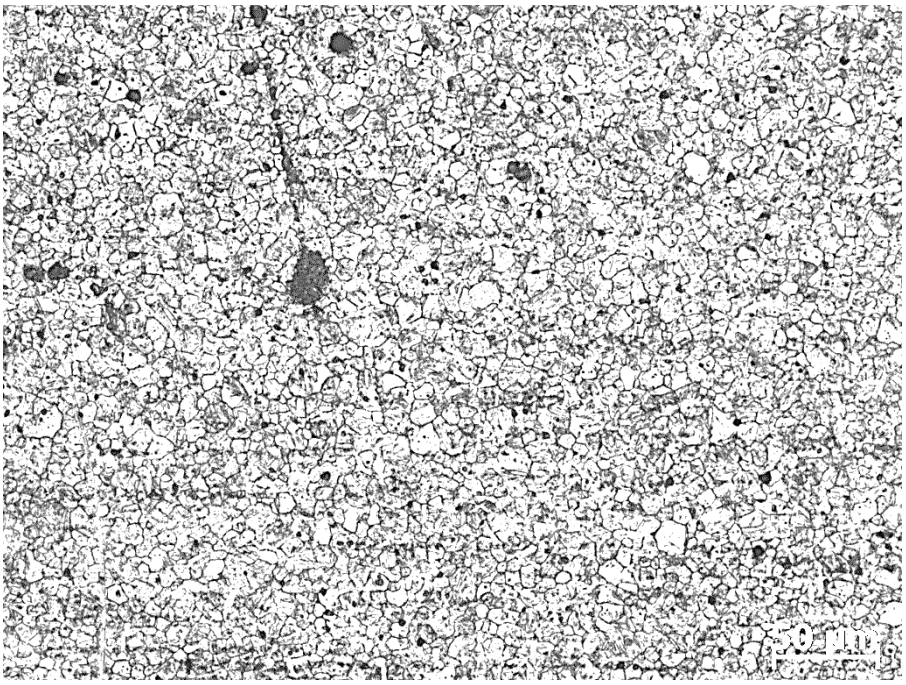

Figure i. Micrograph showing prior austenite grains in USIBOR 1500 hot-formed at 920°C for 7mins

Figure ii. Micrograph showing prior austenite grains in USIBOR 1500 hot-formed at 950°C for 15mins

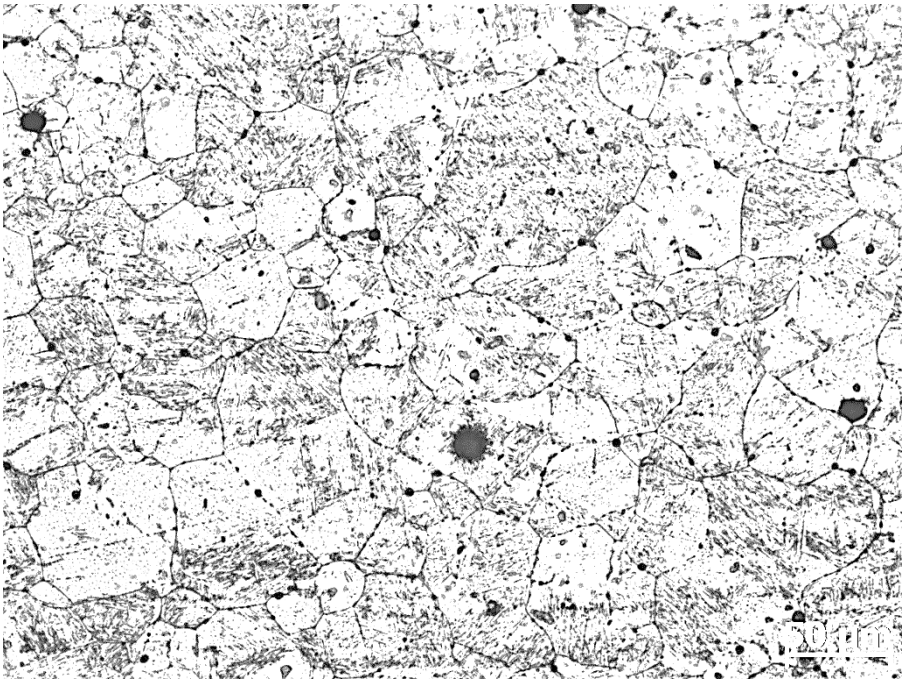

Figure iii. Micrograph showing prior austenite grains in USIBOR 1500 hot-formed at 980°C for 30mins

Hot – forming condition	**$<P_L>$ (/mm)**	**Linear Intercept Grain Size (G) (µm)**
920°C, 7 minutes	144	7.0 $\pm$ 0.3
950°C, 15 minutes	75	13.8 $\pm$ 1.0
980°C, 30 minutes	36	29.1 $\pm$ 2.5

REFERENCES

1. Bhadeshia, H. and R. Honeycombe, *Steels: microstructure and properties*. 2017: Butterworth-Heinemann.
2. Davis, J., *Alloying.* Understanding the Basics, ASM International, Materials Park, OH, 2001. **44073**(0002).
3. Adamczyk, J., *Development of the microalloyed constructional steels.* Journal of Achievements in materials and Manufacturing Engineering, 2006. **14**(1-2): p. 9-20.
4. Jun, H.J., et al., *Effects of deformation and boron on microstructure and continuous cooling transformation in low carbon HSLA steels.* Materials Science and Engineering: A, 2006. **422**(1): p. 157-162.
5. TAMEHIRO, H., et al., *Optimum microalloying of niobium and boron in HSLA steel for thermomechanical processing.* Transactions of the Iron and Steel Institute of Japan, 1987. **27**(2): p. 120-129.
6. KONSTRUKCIJSKA, V.M.H., *High-strength low-alloy (HSLA) steels.* Materiali in tehnologije, 2011. **45**(4): p. 295-301.
7. Militzer, M., E. Hawbolt, and T. Meadowcroft, *Microstructural model for hot strip rolling of high-strength low-alloy steels.* Metallurgical and Materials Transactions A, 2000. **31**(4): p. 1247-1259.
8. Bruce, D.M., et al., *Assessment of the strain-rate dependent tensile properties of automotive sheet steels*. 2004, SAE Technical Paper.

9. Zubko, P., et al. *Changes in Mechanical Properties and Microstructure after Quasi-Static and Dynamic Tensile Loading*. in *Materials Science Forum*. 2014. Trans Tech Publ.

10. Åkerström, P., *Modelling and simulation of hot stamping*. 2006, Luleå tekniska universitet.

11. Liu, H., et al., *Investigation of the hot-stamping process for advanced high-strength steel sheet by numerical simulation.* Journal of Materials Engineering and Performance, 2010. **19**(3): p. 325-334.

12. Naderi, M., et al., *Analysis of microstructure and mechanical properties of different boron and non-boron alloyed steels after being hot stamped.* Procedia Engineering, 2011. **10**: p. 460-465.

13. Merklein, M. and J. Lechler, *Investigation of the thermo-mechanical properties of hot stamping steels.* Journal of Materials Processing Technology, 2006. **177**(1): p. 452-455.

14. Austerhoff, N. and W. Rostek, *Hot Stamping und Wärmebehandlung von höchstfesten Stählen am Beispiel von Karosserie-und Fahrwerksbauteilen.* Tagungsband, 2002. **5**: p. 1-10.

15. Stopp, R., et al. *Warmblechumformung in der Automobil-Serienfertigung—Status, Trends, Potenziale*. in *2nd International Conference on Hot Sheet Metal Forming of High Performance Steels, Luleå, Sweden, June*. 2007.

16. Merklein, M. and J. Lechler, *Determination of material and process characteristics for hot stamping processes of quenchenable ultra high strength*

steels with respect to a FE-based process design. SAE International Journal of Materials and Manufacturing, 2008. **1**(2008-01-0853): p. 411-426.

17. Steinbeiss, H., et al., *Method for optimizing the cooling design of hot stamping tools.* Production Engineering, 2007. **1**(2): p. 149-155.
18. Somani, M.C., et al., *Dimensional changes and microstructural evolution in a B-bearing steel in the simulated forming and quenching process.* ISIJ international, 2001. **41**(4): p. 361-367.
19. Hidaka, K., Y. Takemoto, and T. Senuma, *Microstructural Evolution of Carbon Steels in Hot Stamping Processes.* ISIJ international, 2012. **52**(4): p. 688-696.
20. Karbasian, H. and A.E. Tekkaya, *A review on hot stamping.* Journal of Materials Processing Technology, 2010. **210**(15): p. 2103-2118.
21. Namklang, P. and V. Uthaisangsuk, *Description of microstructures and mechanical properties of boron alloy steel in hot stamping process.* Journal of Manufacturing Processes, 2016. **21**: p. 87-100.
22. Naderi, M., et al., *A numerical and experimental investigation into hot stamping of boron alloyed heat treated steels.* Steel Research International, 2008. **79**(2): p. 77-84.
23. Bahadur, A., *Aluminium diffusion coatings on medium carbon steel.* Materials Transactions, JIM, 1995. **36**(9): p. 1170-1175.
24. Kobayashi, S. and T. Yakou, *Control of intermetallic compound layers at interface between steel and aluminum by diffusion-treatment.* Materials science and engineering: A, 2002. **338**(1): p. 44-53.

25. Bahadur, A., *Structural studies of hot dip aluminized coatings on mild steel.* Materials Transactions, JIM, 1991. **32**(11): p. 1053-1061.

26. Cheng, W.-J. and C.-J. Wang, *Effect of silicon on the formation of intermetallic phases in aluminide coating on mild steel.* Intermetallics, 2011. **19**(10): p. 1455-1460.

27. Gui, Z., W. Liang, and Y. Zhang, *Enhancing ductility of the Al-Si coating on hot stamping steel by controlling the Fe-Al phase transformation during austenitization.* Science China Technological Sciences, 2014. **57**(9): p. 1785-1793.

28. Fan, D.W. and B.C. De Cooman, *Formation of an aluminide coating on hot stamped steel.* ISIJ international, 2010. **50**(11): p. 1713-1718.

29. Wang, K., et al., *Cracking behavior of Al-Si coating on hot stamping boron steel sheet.* Procedia Engineering, 2014. **81**: p. 1713-1718.

30. Wang, K., et al., *Investigation on cracking characteristics of Al–Si coating on hot stamping boron steel parts based on surface strain analysis.* Surface and Coatings Technology, 2017. **309**: p. 282-294.

31. Naderi, M., et al., *Analysis of microstructure and mechanical properties of different high strength carbon steels after hot stamping.* Journal of Materials Processing Technology, 2011. **211**(6): p. 1117-1125.

32. Bardelcik, A., et al., *Effect of cooling rate on the high strain rate properties of boron steel.* International Journal of Impact Engineering, 2010. **37**(6): p. 694-702.

33. Bardelcik, A., et al., *A strain rate sensitive constitutive model for quenched boron steel with tailored properties.* International Journal of Impact Engineering, 2012. **50**: p. 49-62.

34. Underwood, E.E., *Quantitative Stereology*. 1970: Reading, Mass., Addison-Wesley Pub. Co.

35. Microscopy, Q., *RT DeHoff and FN Rhines, eds*. 1968, McGraw-Hill, New York, NY.

36. DeHoff, R.T. and F.N. Rhines, *Quantitative microscopy.* 1968.

37. Baddeley, A., H.-J.G. Gundersen, and L.M. Cruz-Orive, *Estimation of surface area from vertical sections.* Journal of Microscopy, 1986. **142**(3): p. 259-276.

38. Gokhale, A.M. and W.J. Drury, *Efficient measurement of microstructural surface area using trisector.* Metallurgical and Materials Transactions A, 1994. **25**(5): p. 919-928.

39. Gundersen, H.J.G., *Notes on the estimation of the numerical density of arbitrary profiles: the edge effect.* Journal of microscopy, 1977. **111**(2): p. 219-223.

40. Gokhale, A. and E. Underwood, *A general method for estimation of fracture surface roughness: Part I. Theoretical aspects.* Metallurgical and Materials Transactions A, 1990. **21**(5): p. 1193-1199.

41. Gokhale, A. and W. Drury, *A general method for estimation of fracture surface roughness: Part II. Practical Considerations.* Metallurgical and Materials Transactions A, 1990. **21**(4): p. 1201-1207.

42. Gokhale, A.M., *Quantitative fractography*. Materials Park, OH: ASM International, 2002., 2002: p. 538-558.

43. Gokhale, A., W. Drury, and S. Mishra, *Recent developments in quantitative fractography,* in *Fractography of Modern Engineering Materials: Composites and Metals, Second Volume*. 1993, ASTM International.

44. Louis, P. and A.M. Gokhale, *Application of image analysis for characterization of spatial arrangements of features in microstructure.* Metallurgical and Materials Transactions A, 1995. **26**(6): p. 1449-1456.

45. Alkhader, M. and L. Bodelot, *Large strain mechanical behavior of HSLA-100 steel over a wide range of strain rates.* Journal of Engineering Materials and Technology, 2012. **134**(1): p. 011005.

46. Narayanasamy, R., et al., *A study on fracture behaviour of three different high strength low alloy steel sheets during formation with different strain ratios.* Materials & Design, 2008. **29**(9): p. 1868-1885.

47. Steinbrunner, D.L., D. Matlock, and G. Krauss, *Void formation during tensile testing of dual phase steels.* Metallurgical Transactions A, 1988. **19**(3): p. 579-589.

48. Rashid, M., *Formable HSLA and dual-phase steels.* TMS AIME, Warrendale, PA, 1979. **244**: p. 1-24.

49. Oliver, S., T. Jones, and G. Fourlaris, *Microstructure and dynamic material performance of high strength and ultra high strength strip steels.* Materials science and technology, 2007. **23**(1): p. 55-62.